DEVELOPMENT AND APPLICATION OF A PROGNOSTIC CUMULUS PARAMETERIZATION

by Dzong-Ming Pan

David A. Randall, Principal Investigator

Colorado State University

DEPARTMENT OF ATMOSPHERIC SCIENCE

PAPER NO. 580

DEVELOPMENT AND APPLICATION OF A PROGNOSTIC CUMULUS PARAMETERIZATION

by

Dzong-Ming Pan

Research supported by the
National Science Foundation
under grant numbers ATM-9121629 and ATM-9214981
and by the
U.S. Department of Energy
under grant number DE-FG03-94ER91629

Department of Atmospheric Science
Colorado State University
Fort Collins, CO

June 1995

Atmospheric Science Paper No. 580

ABSTRACT

DEVELOPMENT AND APPLICATION OF A PROGNOSTIC CUMULUS PARAMETERIZATION

The Arakawa-Schubert cumulus parameterization assumes a quasi-equilibrium between the cumulus convection and the "large-scale forcing." It is, however, not very clear that it is always possible to distinctly separate the "non-convective processes" from the convective processes. We therefore propose a prognostic approach for implementing the Arakawa-Schubert parameterization. We relax the assumption of cloud work function quasi-equilibrium by explicitly using a cumulus kinetic energy (CKE) equation. This approach bypasses the ambiguity in separating the large-scale forcing from the cumulus convection, and may be the first step toward improving the interactions between parameterized physics in large-scale numerical models. The CKE approach also simplifies the calculation and hence allows more sophisticated physics of convection, such as downdrafts, to be taken into account.

Simple experiments with constant radiative cooling in a one dimensional (1-D) model showed that the steady-state solution depends on the value of α, a parameter that relates CKE to cloud base mass flux. Experiments also showed that LSP (large-scale precipitation) is a part of the "forcing" for the cumulus convection, and that how we parameterize the LSP has direct effects on the results. In the meantime, the LSP is also a response to convective detrainment. Therefore, we cannot really clearly separate forcing and response, as Arakawa and Schubert (1974) did.

The prognostic CKE approach was tested in the 1-D model to simulate observations from the GARP (Global Atmospheric Research Program) Atlantic Tropical Experiment. We can successfully simulate the time evolution of the precipitation rate and the vertical distribution of the apparent heat source and moisture sink. The atmosphere is saturated

too often in the simulation, however. This can be attributed to the over-simplified large-scale saturation parameterization (LSP) which re-evaporates the precipitation falling from upper levels. LSP does not become active until the whole grid box is saturated.

Two different values of α were tested in the GATE simulation. Results indicate that one value of α produces a better time evolution, while the other generates a more realistic vertical structure of the heating rate. This may be due to the fact that we have used only one α for all cloud types. According to the relation derived from the definitions of CKE and cloud-base mass flux, α should be a function of cloud depth.

We tested the prognostic CKE approach against the cloud work function quasi-equilibrium with the Colorado State University general circulation model. It was found that the model produces much higher anvil incidence which dramatically reduces the absorbed solar radiation in the tropics. A "fractional coverage" has been introduced in the simple anvil parameterization. Using the fractional anvils with the CKE approach, we found improvements in the January global precipitation distribution, especially over land. Cumulus convection also occurs much more often.

As a part of the development of the prognostic CKE cumulus parameterization, the fractional entrainment rate, λ, is used as the cloud spectral parameter, replacing the detrainment-level height as chosen by Lord (1978). Lord (1978)'s approach had been questioned by other authors (e.g. Kao and Ogura, 1987) and was proven incompatible with the CKE approach. With this approach, λ is an independent variable and the value of α should depend on $\Delta\lambda$ and the vertical resolution of the model. The independent variable λ appears to be a physically more reasonable identifier for cloud types.

Acknowledgments

I thank my advisor, Professor David A. Randall, for his guidance, patience, and inspiration throughout the course of this dissertation. He is helpful not only in enlightening me in science but also in improving my writing skill. The "300-level" technical writing course that he insisted that I take has proven beneficial for my thesis writing and, I believe, will be useful for my future career.

Thanks also go to my other committee members, Professors Richard H. Johnson, Wayne H. Schubert, and David A. Krueger for their invaluable suggestions for preparing this dissertation.

I would also like to thank Don Dazlich, the GCM guru, for his help on using the CSU GCM. I am grateful to Drs. Kuanman Xu and Scott Denning for suggestions on preparing my defense seminar. Dr. Laura D. Fowler also helped me on using the satellite data. Ms. Cindy Carrick is of great help in the whole process of my defense. Thanks are also due to Kelley Wittmeyer, Ping Ding, and Ross Heikes.

Thanks are due to my parents for their support through the years, both spiritually and economically. Their persistent encouragement and belief are important reasons that I come this far academically.

This work was supported by the National Science Foundation under grants ATM-9121629 and ATM-9214981, and by the U. S. Department of Energy under grant DE-FG03-94ER91629. Part of the work was done using the computing resources in the National Center of Atmospheric Research, Boulder, Colorado.

CHAPTER 1 Introduction

CHAPTER 2 A Prognostic Closure for the Arakawa-Schubert Cumulus Parameterization

CHAPTER 3 Testing the CKE Approach Using a One-Dimensional Model

CHAPTER 5 The Cloud Spectral Parameter

CHAPTER 6 Concluding Discussion

List of Figures

CHAPTER 1

Introduction

1.1 Cumulus Convection and the Atmospheric General Circulation

Cumulus convection plays an important role in the atmospheric general circulation. It vertically transports latent energy and is the main mechanism to balance radiative energy losses in the atmosphere. The atmosphere is basically transparent to solar radiation. Except for the 30% that is reflected back to space by clouds, most of the rest of the energy from the sun can reach directly to the Earth's surface. The long-wave radiation absorbed or emitted by the atmosphere and the Earth's surface results in a net energy flux divergence in the atmosphere. These energy fluxes depend on the composition of the atmosphere. Grossly speaking, with the current composition, each layer of the atmosphere is radiatively cooled at the rate of approximately 2 K day^{-1}. To balance this energy deficit, conduction from the Earth's surface through turbulence transport cannot effectively reach high into the free atmosphere. On the other hand, cumulus convection can carry energy all the way to the tropopause.

In the process of latent energy transport, cumulus convection also vertically redistributes water vapor. The vertical distribution of water vapor in the atmosphere largely accounts for the temperature lapse rate, because water vapor is one of the most important radiatively active gases. Manabe and Strickler (1964) demonstrated that the Earth's climate is close to a radiative-convective equilibrium. They used a realistic vertical distribution of the radiatively active gases, such as H_2O, CO_2, and ozone, to simulate the equilibrium. Their model atmosphere reaches a radiative equilibrium state with a super-adiabatic temperature lapse rate near the surface. This equilibrium state is unstable with respect to free convection, which can also redistribute heat and moisture vertically. A radiative-convective equilibrium state results. Cumulus convection, however, can occur even when the lapse rate is not super-adiabatic, because the release of latent heat can provide extra buoyancy. Furthermore, cumulus convection is closely linked to stratiform clouds which are usually long-lasting and radiatively important.

The latent heat release by cumulus clouds is also an important energy source for the development of tropical cyclones. The interaction between cumulus latent heat release and synoptic scale disturbances, which supply the moisture for convection, is important for tropical cyclones' intensification (Charney and Eliassen 1964).

1.2 Cumulus Parameterization

Since cumulus convection plays an important role in the general circulation, as discussed above, its effects must be taken into account when we simulate the general circulation using large-scale numerical models. These models, such as the general circulation models (GCMs), have grid boxes on the order of 500 km by 500 km horizontally. However, the diameter of a cumulus cloud is on the order of 10 km or less. Obviously, cumulus clouds cannot be resolved in large-scale numerical models. Therefore, an alternative way to express the effects of cumulus convection is needed. Of course, the modelled cumulus effects should be related to the resolvable quantities. Representation of the cumulus effects in terms of grid-scale variables is called cumulus parameterization.

There have been numerous studies about the cumulus effects on the general circulation. One of the simplest approach has been to prescribe a (cumulus) heating profile (usually idealized from observations), and make the general circulation adjust to this fixed heat source/sink (e.g., Hartmann *et al.*, 1984). However, this approach neglects the feedback from the large-scale circulation on the cumulus convection. A cumulus parameterization allows cumulus heating to interact with the large-scale environment. Both the large-scale environment and the cumulus effects vary with time.

To correctly represent cumulus effects in a model, it is important to understand how cumulus convection interacts with the large-scale environment. Cumulus convection occurs only when there is moist convective instability. Given an appropriate trigger, cumulus convection consumes the instability by modifying the environment. Yanai *et al.* (1973) did an analysis of some tropical data and identified the two most important ways by which the cumulus clouds modify the large-scale environment. Basically, the cumuli warm and dry the environment by inducing adiabatic subsidence outside the clouds, through the conservation of mass. Meanwhile the re-evaporation of the detrained condensates moistens and cools the atmosphere. Yanai *et al.* (1973, 1976) also argued that the existence of shallow non-precipitating cumuli helps the growth of deep convection because detrainment from shallow clouds moistens the environment.

Since a single cumulus cloud only occupies a tiny fraction of a grid-box area (horizontally), and often many cumuli co-exist in the same time, it is not practical to treat individual cumulus clouds separately. The cumulus clouds must be treated as an ensemble, and only their collective effects can be considered. The scale separation between cumulus clouds and resolvable large-scale motions allows the effects of cumulus convection to be treated in a statistical way. Assume any variables ψ and χ can be decomposed into two parts: $\psi = \overline{\psi} + \psi'$ and $\chi = \overline{\chi} + \chi'$, where overbars denote an averaging operator such that $\overline{\psi'} = 0$ and $\overline{\chi'} = 0$ are satisfied. We then have $\overline{\psi\chi} = \overline{\psi}\overline{\chi} + \overline{\psi'\chi'}$. Using this averaging procedure, the budget equations for energy and moisture, horizontally averaged over a grid box, can be written as:

$$\rho\frac{\partial\bar{s}}{\partial t} = -\overline{\nabla \bullet (\rho s V)} - \frac{\partial}{\partial z}(\rho\bar{s}\bar{w}) + Q_1, \tag{1.1}$$

$$\rho\frac{\partial\bar{q}}{\partial t} = -\overline{\nabla \bullet (\rho q V)} - \frac{\partial}{\partial z}(\rho\bar{q}\bar{w}) - \frac{Q_2}{L}, \tag{1.2}$$

where the dry static energy is $\bar{s} \equiv c_p\overline{T} + gz$. Overbars represent a horizontal area average; $\overline{T}$ is temperature, and c_p is the specific heat at constant pressure. q is the water vapor mixing ratio, w is the vertical wind, and V is the horizontal velocity. L is the latent heat of evaporation, and Q_R is the radiative heating rate. ρ is the air density. Q_1 and Q_2 are the "apparent heat source" and "apparent moisture sink" defined by Yanai (1973):

$$Q_1 \equiv Q_R + L \bullet C - \frac{\partial}{\partial z}(\rho \overline{w's'}) \,, \qquad (1.3)$$

$$Q_2 \equiv L \bullet C + L\frac{\partial}{\partial z}(\rho \overline{w'q'}) \,. \qquad (1.4)$$

Here primes (') denote deviations from the horizontal average, and C is the net condensation. It is assumed that the vertical eddy transport is mainly due to the effects of cumulus convection. The key problem of cumulus parameterization is to provide closure for Eqs. (1.1) and (1.2), in which there are four variables: $\frac{\partial \bar{s}}{\partial t}$, $\frac{\partial \bar{q}}{\partial t}$, ($Q_1$-$Q_R$), and Q_2 (Arakawa and Chen, 1987).

Many approaches have been invented for cumulus parameterization. A comparison of the most popular cumulus schemes was given by Arakawa and Chen (1987). Among those are the Kuo scheme (Kuo, 1965) and the moist convective adjustment scheme (Manabe *et al*, 1965). These two schemes are relatively simple, and hence have been widely applied in numerical models (e.g. Donner *et al.*, 1982). In addition, there have also been a lot of publications about the Betts-Miller scheme (e.g., Betts and Miller, 1986, and Betts, 1986).

Moist convective adjustment scheme adjusts a saturated super-moist-adiabatic lapse rate back to a saturated moist adiabat. This scheme does not allow precipitation to occur when the large-scale environment is not saturated. However, convective clouds usually only occupy a small fraction of the area of a grid box in a large-scale numerical model. An average over a large area can easily eliminate local saturation.

The original Kuo scheme was used in a hurricane model (Kuo, 1965). Since latent heat is the major energy source for the development of hurricanes, Kuo (1965) paid special attention to the moisture source. He related cumulus heating to the large-scale moisture convergence with a disposable parameter. The potential temperature was adjusted to a moist adiabat in a short relaxation time. Essentially, the disposable parameter determines the percentage of the moist static energy change (increase), due to the large-scale moisture convergence into the column of atmosphere, to heat or to moisten. The vertical distribution of the cumulus heating and moistening is determined by the sounding and the moist adiabat. However, when the moist adiabat is obtained by lifting air parcels from the PBL, the parameterized cumulus can never affect the PBL, as discussed by Raymond and Emanuel (1993). Arakawa and Chen (1987) also showed that the cumulus effects calculated using the Kuo scheme are very sensitive to the disposable parameter. Experience shows that it is inappropriate to use the same constant everywhere on the earth. For this reason, there are modified Kuo schemes. For example, Anthes (1977) related the disposable parameter in the original Kuo scheme to the mean relative humidity of the troposphere.

The Betts-Miller scheme (e.g., Betts and Miller, 1986) uses a so-called "mixing line" method to find some reference profiles, in which the average "saturation point" in a large-scale area is almost constant with time. They assume that the cumulus convection is in a quasi-equilibrium with "large-scale forcing." The cumulus clouds take a relaxation time to adjust the temperature and mixing ratio back to the reference states. The determination of the relaxation time for this scheme is critical but it is still obtained empirically. Meanwhile, two distinct reference states for deep and shallow (non-precipitating) convection, separately, are needed. The distinction between deep and shallow convection is arbitrary.

The Arakawa-Schubert (Arakawa and Schubert, 1974) scheme (A-S scheme, hereafter) is the most physically sophisticated cumulus parameterization. It uses a cloud model and takes into account explicitly the interaction between the cumulus clouds and the environment. The A-S scheme is the starting point of this study. I shall start with a brief review of this scheme in the following section.

1.3 Review of the Arakawa-Schubert Cumulus Parameterization

Consider an ensemble of cumulus clouds in a grid box, in which we are only interested in the statistical properties of the whole ensemble. Let $\tilde{\phi}$ and $\bar{\phi}$ represent values of any quantity ϕ in the environment and its average over the large-scale horizontal area, respectively, and let ϕ_c be the average value of ϕ in the cumulus clouds. We have $\bar{\phi} = \sigma\phi_c + (1-\sigma)\tilde{\phi}$, where σ is the fractional cloud coverage. We assume that $\sigma << 1$. Therefore, we have $\tilde{s} \sim \bar{s}$ and $\tilde{q} \sim \bar{q}$, and $\rho w_c >> \rho|\bar{w}|$. The eddy transport terms in (1.1) and (1.2), using the above approximations, can be written as

$$\begin{aligned} \rho\overline{w's'} &= \rho\sigma(w_c - \bar{w})(s_c - \bar{s}) + \rho(1-\sigma)(\tilde{w} - \bar{w})(s - \bar{s}) \\ &\sim \rho\sigma w_c (s_c - \bar{s}) \\ &\sim M_c (s_c - \bar{s}), \end{aligned} \tag{1.5}$$

where M_c is the total cloud mass flux, as a function of z; and similarly,

$$\rho\overline{w'q'} \sim M_c(q_c - \bar{q}) \,. \tag{1.6}$$

Using the budget equations for the clouds themselves and assuming no storage of mass, water vapor and static energy in the cloud ensemble, (1.1) and (1.2) reduce to:

$$\rho\frac{\partial\bar{s}}{\partial t} = D_s + (M_c - \rho\bar{w})\frac{\partial\bar{s}}{\partial z} - \rho\bar{V} \bullet \nabla\bar{s} + \overline{Q_R}, \tag{1.7}$$

and

$$\rho\frac{\partial\bar{q}}{\partial t} = D_q + (M_c - \rho\bar{w})\frac{\partial\bar{q}}{\partial z} - \rho\bar{V} \bullet \nabla\bar{q}, \tag{1.8}$$

where D_s and D_q denote the effects of detrainment on $\bar{s}$ and $\bar{q}$, respectively. It has also been assumed that the horizontal eddy transport is negligible. Eqs (1.7) and (1.8) explicitly show how the cumulus clouds modify their environment. The cumulus-induced subsidence warms and dries the environment through the second terms on the right-hand sides of these equations. The detrainment cools and moistens the environment through terms D_s and D_q, depending on the amount of mass and condensate detrained. It was assumed by Arakawa and Schubert (1974) that all detrained condensate evaporates *in situ*. To use (1.7) and (1.8) to predict $\bar{s}$ and $\bar{q}$, we have to know the detrainment mass flux, the mixing ratio of liquid water at the detrainment level, and M_c. The problem of cumulus parameterization is thus to relate these properties of the cumulus ensemble to the large-scale variables.

If clouds only detrain in infinitesimally thin layers, the detrainment mass flux is thus the M_c in the layer where the clouds lose buoyancy. The cumulus ensemble can therefore be divided into subensembles according to the detrainment level height. The detrainment mass flux, as a function of height, can be considered as the mass flux distribution over a "spectrum" of cloud types (i.e. clouds that detrain at different heights).

The cumulus parameterization problem is further simplified if we assume that each cloud type can be fully characterized by a fractional entrainment rate. Given the cloud-base conditions and the environment sounding, a fractional entrainment rate determines a vertical distribution of cumulus mass flux and in-cloud moist static energy and mixing ratio. With the in-cloud sounding, we can determine the detrainment level where clouds lose buoyancy. The cumulus parameterization problem then reduces to the determination of the cloud-base mass flux.

Arakawa and Schubert (1974) divided the cumulus ensemble into subensembles. Each subensemble was assumed to be characterized by a constant (with height) fractional entrainment rate, λ. Since buoyancy is the main mechanism for the generation of cumulus convection, it is reasonable to quantify the available potential energy for convection by defining a cloud work function (A) for each cumulus subensemble as a vertical integral of buoyancy:

$$A(\lambda) = \int_{z_B}^{z_D(\lambda)} \frac{g}{c_p \bar{T}(z)} \eta(z, \lambda) \left[s_{vc}(z, \lambda) - \bar{s}_v(z) \right] dz. \tag{1.9}$$

Here z_D is the height of the detrainment level, which is assumed to be where the clouds lose their buoyancy; η is the normalized cloud mass flux, satisfying $M_c = \eta M_B$. M_B is the cloud-base mass flux; $\bar{s}_v = \bar{s} + c_p \bar{T} (0.608\, \bar{q} - \bar{l})$ denotes the virtual static energy; $\bar{l}$ is the mixing ratio of liquid water; subscript c denotes the in-cloud sounding, taking into account dilution by the entrainment of environmental air at each level; z_B is the cloud base, which is assumed to be at the top of the PBL (planetary boundary layer) for all types of clouds. From (1.9), once λ is given, $A(\lambda)$ is a property of the environment only. Basically, $A(\lambda)$ represents the work that is done by buoyancy in lifting an air parcel of unit mass, from cloud base to cloud top. A positive $A(\lambda)$ means the existence of moist convective instability for cloud type λ.

Taking time derivative of (1.9), and using (1.7) and (1.8), we can get

$$\frac{dA}{dt} = J \bullet M_B + F, \tag{1.10}$$

where M_B is the non-negative cloud-base mass flux; F is the "large-scale forcing," which represents the rate of increase of cloud work function due to non-convective processes; and $J \bullet M_B$ includes all the terms involving M_B. The latter processes tend to reduce the cloud work function because cumulus convection stabilizes the environment, so that J is usually negative. Eq. (1.10) is a schematic form of a first degree Fredholm integral equation as derived by Arakawa and Schubert (1974). The kernel is denoted by J. Keep in mind that (1.10) holds for each cumulus subensemble, even though in the equation we have omitted the dependence on λ.

1.3.1 The Quasi- Equilibrium Assumption

As mentioned earlier, the cumulus parameterization problem is to determine the cloud-base mass flux, M_B. There are now two variables in Eq (1.10): A and M_B. To solve for M_B, we need a closure assumption. For that purpose, Arakawa and Schubert (1974) assumed quasi-equilibrium of the cloud work function, i.e.

$$\frac{dA}{dt} \cong 0. \tag{1.11}$$

Physically, cloud work function quasi-equilibrium means that the moist convective instability generated by the large-scale forcing is consumed immediately by cumulus convection. This is a reasonable assumption because the time scale of large-scale processes is much longer than the "adjustment time" in which cumulus clouds consume the convective instability. The adjustment time was estimated to be between 10^3 and 10^4 sec. The consumption of the cloud work function by cumulus convection is so efficient that it occurs instantaneously, compared to the creation of cloud work function by large-scale processes.

This assumption has been verified using observations, by Arakawa and Schubert (1974), Lord and Arakawa (1980), Lord (1982) and Kao and Ogura (1987), etc. Lord and Arakawa (1980) calculated cloud work functions using soundings obtained under a variety of large-scale situations. They found that the cloud work functions depend only on the depth of the clouds. For each cloud type, the cloud work functions fall in a narrow range despite the wide variety of temperature and moisture vertical distributions. This means that the quasi-equilibrium of cloud work function is a good assumption under many different large-scale situations.

Lord (1982) and Kao and Ogura (1987) carried out semi-prognostic tests of the scheme, in which they inputted the observed sounding and large-scale advection every hour. The sounding was used to calculate the kernel (J) in equation (1.10). The large-scale forcing (F) was calculated as the tendency of the cloud work function (A) due to large-scale advection. With (1.11), (1.10) can be solved for M_B at every hour. An advantage of this semi-prognostic test is that the cumulus effects can be isolated from other processes in the model, e.g. radiation or large-scale condensation. Also the computed modification of the environment by cumulus effects is not used on the next time step. As a result, even the errors from the cumulus scheme do not accumulate with time. These semi-prognostic tests demonstrated that the A-S scheme can very well reproduce the GATE (GARP Atlantic Tropical Experiment) observations such as precipitation, Q_1 and Q_2. The quasi-equilibrium assumption was proven successful.

The cumulus parameterization problem deals with the interactions between cumulus convection and the large-scale environment. The semi-prognostic tests, however, only focus on the "response" of cumulus convection to the "large-scale forcing," since the "parameterized" cumulus effects never feedback to the environment. A complete interaction between the cumulus convection and the environment can only be seen in a prognostic model. The error caused by incorrectly-represented interactions among the parameterized physics in the model can become significant especially after long integration with time in climate simulations.

1.3.2 The Large-Scale Forcing

Since cumulus parameterization deals with the interaction between the cumulus convection and the large-scale environment, it is convenient to assume that the atmospheric processes can be divided into two parts that interact with each other (the two terms on the right hand side of eq. (1.10)). One part is the cumulus convection, the other includes all the non-convective processes and is called the "large-scale forcing." One may ask: Is there a clear distinction between the convective and non-convective processes in the real world?

An example to demonstrate the above question is the relation between anvil (stratiform) clouds and cumulus convection. Stratiform clouds often get their water supply through detrainment of cumulus convection. Rutledge and Houze (1987) concluded from a diagnostic modeling study that, in a squall line system, stratiform rain cannot occur without the advection of hydrometeors from the convective region into the stratiform region. Should the stratiform clouds, for that reason, be treated as a convective process even though they may not be sub-grid scale?

Anvil clouds play a more important role in cloud-radiation interactions than cumulus clouds. Not only being optically thick, anvil clouds usually also cover a large horizontal area and last a long time. Since the radiation is a main driving force for the atmosphere, the radiative effects of anvil clouds need to be appropriately represented in the large-scale models. Randall *et al.* (1989) showed the strong interactions among radiation, cumulus convection and anvil clouds. Basically, radiation destabilizes the atmosphere and creates convective instability. Cumulus convection then occurs and redistributes heat and moisture vertically. The formation of anvil clouds through the convective detrainment in turn changes the radiation field. The anvil clouds may have a stabilizing effect on convection by blocking the shortwave radiation to the earth surface, or by warming up the atmosphere through the greenhouse effect. Randall *et al.* concluded that there is a need for a more realistic coupling among the parameterized processes in GCMs. Randall (1989) summarized the status and prospects of the cloud parameterization, emphasizing the importance of the cloud radiative forcing for climate.

The anvil clouds can change the radiation field and, through which, largely determine the convective activities as discussed above. They are, in this sense, a "forcing" for cumulus convection. On the other hand, as we also mentioned, the anvil clouds acquire their water supply from cumulus detrainment, which implies that the anvil clouds are actually a "response" to the cumulus clouds. It seems at least for the interaction between the anvil clouds and the cumulus convection, the definition of large-scale forcing is a little fuzzy.

The problem in distinctly defining the large-scale forcing can also be demonstrated by considering the interaction between the parameterized cumulus convection and the large-scale condensation process in a model. To simplify the cumulus parameterization problem, Arakawa and Schubert (1974) assumed that all detrained liquid water evaporate immediately. The evaporation usually causes supersaturation and triggers the large-scale condensation that re-condenses the water vapor. This may not be realistic especially when considering the low temperatures at high elevations, where the cold atmosphere there is easily saturated and detrained liquid water is not likely to evaporate much in the first place. The coupling between the cumulus convection and the large-scale condensation obviously needs improvement.

A clearer or more correct separation between the large-scale forcing and the cumulus convection in the parameterization can be a first step toward improving the coupling between the parameterized cumulus convection and the other physical processes in the model.

Despite its success in observational and semi-prognostic tests, the A-S scheme has not been as popular as the Kuo scheme and the MSTADJ scheme in numerical weather prediction models. The reason is practical. Solving the Fredholm integral equation, with the constraint that mass flux must be non-negative, is complicated and expensive. For that reason, researchers have been working on simplified versions of the A-S scheme, while keeping its basic idea unchanged (e.g. Moorthi and Suarez, 1992; Randall and Pan, 1993).

If the A-S parameterization can be simplified, more physics then can be included. For example, downdraft has been neglected in Arakawa and Schubert (1974). The effects of vertical wind shear have also been ignored in the A-S parameterization. A simplification of the A-S scheme may make it easier to include the effects of the shear and downdrafts in the parameterized cumulus convection. Also, currently all cumulus clouds are assumed to originate from the top of the PBL. In reality, cumulus clouds can start in the free atmosphere.

1.4 The Cloud Spectral Parameter

Cumulus clouds are often considered as entraining plumes (e.g. Simpson et al., 1965; Sloss, 1967; Johnson, 1980; and Albrecht *et al*, 1986, etc.) which have proven to work reasonably well recently by Lin (1994). Arakawa and Schubert (1974) decomposed the cumulus ensemble into subensembles and assumed that the fractional entrainment rate for each cumulus subensemble is constant with height. Once a number is given for each subensemble as the fractional entrainment rate, the vertical distribution of mass flux and in-cloud properties for each cloud type can be determined. In cumulus clouds, mixing with drier and cooler environmental air diminishes the cloud buoyancy. The stronger the entrainment is, the sooner the clouds lose their buoyancy and the shallower they are. The detrainment level and the fractional entrainment rate thus have a one-to-one correspondence. For that reason, the detrainment-level height seems to be a good "cloud spectral parameter."

Lord (1978) used the detrainment-level height to define cloud types in the model. The fractional entrainment rate thus becomes a dependent variable and has to be calculated at every timestep. This approach seems to be convenient because the resolution for cumulus heating and moistening matches the vertical resolution of the model. However, using the detrainment level to identify a cumulus subensemble is obviously different from using the fractional entrainment rate. As a result, this choice may lead to some numerical problems when applied with our approach of the modified A-S scheme, as will be shown later with the numerical experiments. The iteration for the entrainment rate also takes much computation.

1.5 Summary

In this chapter, we have briefly discussed the important role the cumulus convection plays in the atmospheric general circulation, and the problem of cumulus parameterization in large-scale numerical models. We have also very briefly discussed the methods of cumulus parameterization that have been proposed. Among these methods, the Arakawa-Schubert parameterization is physically most complete.

The basic assumption of the A-S cumulus parameterization is that the cumulus convection is always in a quasi-equilibrium with the "large-scale forcing." It is conceptually convenient to divide all the atmospheric processes into convective processes and non-convective processes — the large-scale forcing. However, practically it is not always easy to do so. An example is the close relation between the stratiform clouds and the cumulus convection. The stratiform clouds usually owe their existence to the cumulus clouds, while they are a part of the large-scale processes.

Our purpose of this study is to explore a different approach for implementing the A-S cumulus parameterization. With this approach, we hope to avoid the ambiguity in the definition of the large-scale forcing as explained above, while still keeping the basic idea of the A-S parameterization. This is also a first step toward improving the coupling among model physics (e.g. between the stratiform clouds and the cumulus convection). On the other hand, the calculation of the kernels is complex and computationally expensive. Our new method can thus simplify the calculation and consequently allow more physics of cumulus convection, such as the effects of the vertical wind shear, to be taken into account.

We summarize the A-S parameterization with a simple flow chart in Fig. 1.1, in which the interactions between cumulus convection and large-scale processes are illustrated. The box in the upper half of the figure includes the processes that contribute to the "large-scale forcing". They are PBL turbulence, radiation, advection, and the effects of stratiform clouds. We put the stratiform clouds in the category of the large-scale forcing, because practically they are a part of the grid-scale processes in the model. The A-S scheme considers all the non-convective processes as a package — the large-scale forcing. With our new approach [the "CKE (cumulus kinetic energy) approach", to be discussed in the next chapter and is indicated by a thick solid-arrow], all the procedures in the shaded area (including the calculation of the large-scale forcing and the kernels) are dropped. Therefore, the "CKE approach" bypasses the explicit calculation/definition of F and J. The relation between the CKE approach and the A-S parameterization shall become more clear in Chapter 2. In Chapters 3 and 4, we shall present some tests of the new approach. We shall use a different cloud spectral parameter in Chapter 5, followed by conclusions in Chapter 6.

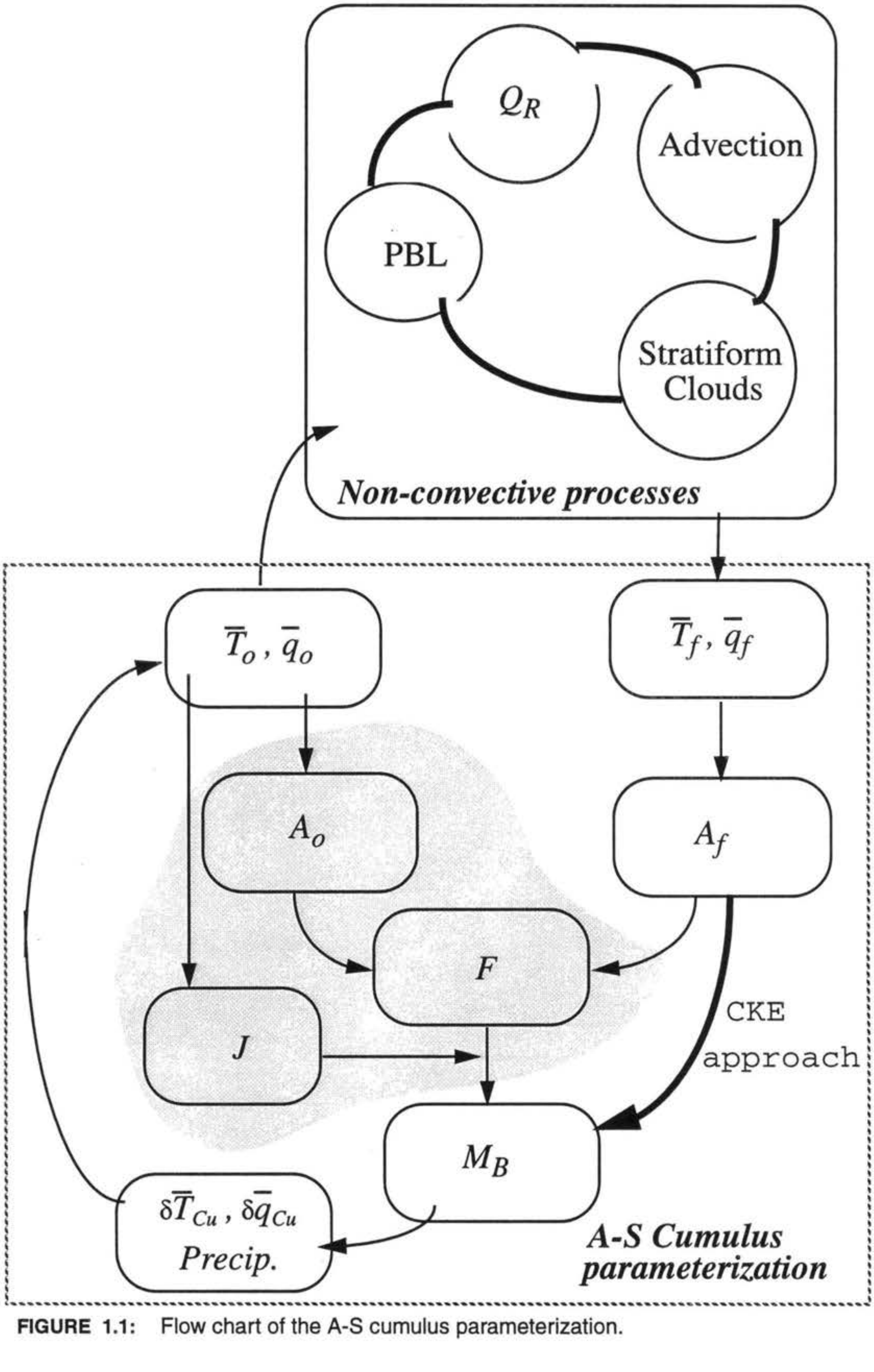

FIGURE 1.1: Flow chart of the A-S cumulus parameterization.

CHAPTER 2

A Prognostic Closure for the Arakawa-Schubert Cumulus Parameterization

In this chapter, we shall discuss a new method to apply the A-S cumulus parameterization. Our approach is to relax the quasi-equilibrium assumption without abandoning the basic concepts on which it is based. As a starting point, we take the ideas of Lord and Arakawa (1980), who extended the concept of quasi-equilibrium by considering the conservation equation for the cumulus kinetic energy, CKE (K), of a cumulus subensemble:

$$\frac{dK}{dt} = M_B A - D = M_B (A - \mathbb{D}) . \tag{2.1}$$

Here K is the vertically integrated kinetic energy of the subensemble per unit area, and D is the rate at which K is dissipated. In the time-scale that we are interested in in a large-scale model, (2.1) reduces to a "kinetic energy quasi-equilibrium"

$$A = \mathbb{D} . \tag{2.2}$$

Lord and Arakawa (1980) further assumed that the dissipation term per unit M_B, $\mathbb{D}$, is only an "intrinsic" property of cumulus subensemble and is independent of the large-scale environment. On the other hand, the cloud work function, A, depends solely on the large-scale thermodynamical structure. The kinetic energy quasi-equilibrium then becomes a balance between the large-scale thermodynamical structure and the cloud-scale dissipation. The time derivative of (2.2) leads to quasi-equilibrium of cloud work function — Eq (1.11). Therefore, the calculation of M_B does not need to use the CKE equation, (2.1), explicitly.

We modify the A-S parameterization by making explicit use of (2.1) to prognostically determine the CKE. The dissipation term is determined by introducing a dissipation time scale, denoted by τ_D, so that the prognostic equation for K becomes

$$\frac{dK}{dt} = M_B A - \frac{K}{\tau_D}. \tag{2.3}$$

τ_D, in other words, is the time it takes to dissipate the CKE when there is no CKE generation. Therefore, τ_D must not be longer than the actual life time of cumulus clouds, and was estimated to be 10^2-10^3 sec by Lord and Arakawa (1980).

Eqs (2.3) and (1.10) together contain three dependent variables: A, K and M_B. We need one more equation to close this problem. We shall derive this equation from the definition of the CKE in the following sections, starting from a more generic form of the CKE equation.

2.1 Cumulus Kinetic Energy

Following the procedure by Stull (1988), we divide variables into the mean and eddy parts in an anelastic system, and derive the eddy kinetic energy equation

$$\frac{\partial \bar{e}}{\partial t} + \overline{U}_j \frac{\partial \bar{e}}{\partial x_j} = \delta_{i3} \frac{g}{\overline{\theta}_v} (\overline{u_i \theta_v}) - \overline{u_i u_j} \frac{\partial}{\partial x_j} \overline{U}_i$$

$$- \frac{1}{\rho_0} \frac{\partial}{\partial x_j} (\rho_0 \overline{u_j u_i^2}) - \frac{1}{\rho_0} \frac{\partial}{\partial x_i} (\overline{u_i p'}) + \varepsilon_\upsilon, \tag{2.4}$$

where the eddy kinetic energy per unit mass is defined as

$$e \equiv \frac{1}{2} u_i^2. \tag{2.5}$$

Here θ_v is the virtual potential temperature; ε_v is the viscous dissipation; ρ_0 is the air density of the mean state; the u_i's denote the perturbation velocities; and δ_{i3} is the Kronecker Delta.

The CKE is defined as the eddy kinetic energy per unit area:

$$K = \frac{1}{2} \int_{z_S}^{z_T} \rho_0 \overline{u_i^2} dz, \tag{2.6}$$

where z_T and z_S are the heights of the cloud top and the earth's surface, respectively. We have assumed that the perturbations are mainly associated with the cumulus convection.

From the definition of K, the CKE equation is a vertical integral of (2.4). The third term on the right hand side of (2.4) is the turbulence transport of the CKE. It neither creates nor destroys CKE. Therefore, this term vanishes when integrated from the surface to the cloud top, because there is no CKE flux across the cloud top or the surface. The fourth term is also a transport term and should be zero after integration. If we further neglect the shear term, the CKE equation then can be written in the form of (2.3). The shear production term was shown to be negligible by Xu (1991) when water loading effect is not included.

The importance of vertical wind shear in convection, however, can be easily found in many studies. Asai (1964) showed that vertical wind shear can suppress convection. Seitter and Kuo (1983) used a simple 2-D model to simulate the up-shear tilting convection. They argued that the water loading is the main mechanism to maintain the up-shear tilting of the convection, in which the ambient wind shear is needed in the first place. Lilly and Jewett (1990) also showed that in their simulated supercell thunderstorms, the kinetic energy from mean flow is comparable with the buoyant energy release. Xu (1991) also found that when vertical wind shear exists, convection becomes organized, and the wind shear production term is of a comparable size with the net buoyancy production term (thermal buoyancy plus water loading).

The shear production term can actually be included in the CKE equation easily by using

$$\rho\overline{u'w'} = M_c(u_c - \overline{U}) . \tag{2.7}$$

Here u_c can be obtained in a similar way by which h_c and q_c are obtained, except that an extra term of convective-scale pressure gradient force must be taken into account, which can also be parameterized (Wu and Yanai, 1994).

In this report as a first step in developing the CKE cumulus parameterization, we shall use only the CKE equation in the form of (2.3). The shear effects will be left in the future work.

2.2 Closure of the Arakawa-Schubert Parameterization Using the CKE equation

To derive a relation between M_B and K, we consider a unit horizontal area in which a small fraction σ is covered by updrafts. The area outside the cumulus clouds undergoes compensating downward motions. Let subscripts u and d represent upward and compensating downward motions, respectively. An overbar denotes the horizontal area-average. We have

$$\overline{w} = \sigma w_u + (1-\sigma) w_d, \tag{2.8}$$

and therefore

$$\begin{aligned}\overline{w'^2} &= \sigma (w_u - \overline{w})^2 + (1-\sigma)(w_d - \overline{w})^2 \\ &= \sigma (1-\sigma)(w_u - w_d)^2.\end{aligned} \tag{2.9}$$

For the flux of any variable q,

$$\rho\overline{w'q'} = \rho\sigma(w_u - \overline{w})(q_u - \overline{q}) + \rho(1-\sigma)(w_d - \overline{w})(q_d - \overline{q})$$
$$\equiv M_c(q_u - q_d), \tag{2.10}$$

where

$$M_C = \rho\sigma(1-\sigma)(w_u - w_d). \tag{2.11}$$

From (2.9) and (2.11), we get

$$\frac{1}{2}\rho\overline{w'^2} = \frac{M_B^2\eta^2}{2\rho\sigma(1-\sigma)}. \tag{2.12}$$

Here we have used $M_c = \eta M_B$, where η is the normalized mass flux, with respect to the cloud-base value. Using the definition of K, Eq (2.6), we can derive

$$K = \alpha \bullet M_B^2, \tag{2.13}$$

which was first proposed by Arakawa and Xu (1990) and Xu (1991). The parameter α is

$$\alpha = \frac{1}{2\varepsilon}\int_{z_S}^{z_T} \frac{\eta^2}{\rho\sigma(1-\sigma)}dz, \tag{2.14}$$

where ε is the fraction of the total kinetic energy that comes from the vertical component of the velocity, or

$$\varepsilon \equiv \frac{1}{K} \int_{z_S}^{z_T} \frac{1}{2} \rho \overline{w'^2} dz. \tag{2.15}$$

Eq (2.14) shows that α mainly depends on ε, σ, and the depth of the clouds. Estimate the order of magnitudes on parts of (2.14): $\eta \sim 1$ (for non-entraining clouds), $\rho \sim 1$ kg m^{-3}, $1/(2\varepsilon) \sim 10^2$, $\sigma(1-\sigma) \sim 10^{-2}$, and the depth of the clouds is on the order of 10^4 m. A change of cloud depth from 8 km to 10 km causes a increase of α by 25%. A change of σ from 0.02 to 0.05 reduces α to 50%. If ε is increased from 1/30 to 1/20, α is reduced by 1/3. Therefore, all these three variables seem to be of comparable significance in contributing to the variation of α.

Xu and Arakawa (1992) found that vertical wind shear acts to increase the fraction of the CKE in the horizontal components of the motion and to decrease the fraction in the vertical component, as shown in Fig. 2.1. The variation of ε seen in Fig. 2.1 suggests that ε may account for the greatest part of the change of α. However, their results also showed significant variation of α [estimated using (2.13), not shown here] with time, following the time change of the prescribed large-scale forcing which is independent of the wind shear.

For a given value of CKE, (2.13) gives a small M_B when α is large. Xu and Arakawa (1992) showed that the existence of vertical wind shear favors a larger α. Since M_B is the agency through which the convection modifies its environment, shear inhibits the feedback of the convection on the mean flow. In particular, shear inhibits convective stabilization of the environment, allowing larger value of the cloud work function (more CAPE) to accumulate in response to the large-scale forcing. Since the shear plays an important role, especially in severe convection, the effects of vertical wind shear should eventually be incorporated into the cumulus parameterization.

In our approach, each cumulus subensemble has its own CKE equation. It seems that the kinetic energy budgets of the various subensembles are formulated independently of one another, and that subensembles do not interact directly. They only interact with one another indirectly by modifying their common environment thermodynamically. We have assumed that the direct dynamical interactions among different subensembles are negligible.

2.2.1 Steady-State Solution

Eqs. (2.1), (2.13) and (1.10) form a closed set of equations that has the steady-state solution:

$$A = -\frac{\alpha}{\tau_D}\frac{F}{J} \equiv A_F, \tag{2.16}$$

$$M_B = -\frac{F}{J} \equiv (M_B)_F, \tag{2.17}$$

$$K = \alpha\left(\frac{F}{J}\right)^2 \equiv K_F. \tag{2.18}$$

Notice that (2.17) can be obtained directly from (1.10) with the quasi-equilibrium assumption. Therefore, this CKE approach reduces to the A-S scheme for a steady state.

The difference between the prognostic CKE approach and the original A-S scheme is mainly in the procedure of calculation. In the CKE scheme, we use the calculated A to predict K, which is then used to obtain M_B (i.e., $\frac{F}{J}$). Unlike the original A-S scheme, neither J nor F needs to be explicitly calculated or defined. After all, M_B is the only variable in the above equations that is actually used in the calculation of the cumulus feedback on the environment. Note also that (2.17) does not involve α or τ_D. According to this equation, it seems that we should get exactly the same solution no matter what values of α and τ_D we use. However, we shall see from the numerical experiments in the following chapter that different α's or τ_D's make the steady-state sounding different. This results in different values of M_B. This also raises the question: To what extent can we apply the CKE scheme with prescribed constant values of α and τ_D?

This procedure of calculation, bypassing the explicit definition of the kernel and the large-scale forcing, sidesteps the ambiguity involved in the separation between the cumulus response and the large-scale forcing.

2.2.2 Behavior of the Parameterized Cumulus in Cloud Time-scale

Quasi-equilibrium of the cloud work function implies that cumulus clouds do not have any memory about their history. Instead, they closely follow the large-scale forcing in a very short adjustment time. With the prognostic CKE approach, we actually have an equation that describes the behavior of cumulus clouds on the cloud time-scale, although our major interest is on the larger time scale.

Combination of (2.1), (2.13) and (1.10), assuming that J is independent of time, gives

$$\frac{d^2 M_B}{dt^2} + \frac{1}{2\tau_D}\frac{dM_B}{dt} - \frac{J}{2\alpha}M_B = \frac{F}{2\alpha}, \tag{2.19}$$

which is a damped-oscillation equation. Notice that this equation holds for each individual cumulus subensemble. We can easily derive a similar equation for A:

$$\frac{d^2 A}{dt^2} + \frac{1}{2\tau_D}\frac{dA}{dt} - \frac{J}{2\alpha}A = \frac{F}{2\tau_D} + \frac{dF}{dt}. \tag{2.20}$$

The second term on the left hand side of (2.19) is the damping term, with a time-scale of $2\tau_D$. Without the third term and the term on the right-hand side, M_B dissipates in a time scale of $2\tau_D$. The third term is an oscillation term. Consider the limit $\tau_D \to \infty$ with $F = 0$, (2.19) reduces to

$$\frac{d^2 M_B}{dt^2} - \frac{J}{2\alpha}M_B = 0. \tag{2.21}$$

Suppose that we initialize M_B at positive values. Although (2.21) appears to predict ensuing free oscillations about $M_B = 0$, the condition that $M_B \geq 0$ implies that these oscillations will halt as soon as M_B has decreased to zero. The time scale for this to occur is proportional to $(\alpha/|J|)^{1/2}$. We can thus interpret $(\alpha/|J|)^{1/2}$ as τ_{adj}, the "adjustment time," defined by Arakawa and Schubert (1974) as the time required for convective processes to reduce A to zero in the absence of large-scale forcing. This shows that the adjustment time is related to α.

According to (2.16), A_F approaches zero as α approaches zero, that is, as the adjustment time becomes short. Arakawa and Schubert argued that the observed values of A are in fact "small" compared to those that would occur if the large-scale forcing acted unopposed over τ_{LS}. The fact that the observed tropical atmosphere is close to neutral stability with respect to moist convection has been emphasized by Xu and Emanuel (1989).

When F varies with time, with time scale τ_{LS}, under what conditions are (2.16) and (2.17) good approximations to (2.19) and (2.19), respectively? To investigate this question, we write,

$$\frac{dF}{dt} \sim \frac{F}{\tau_{LS}}$$

$$\frac{d^2A}{dt^2} \cong \frac{d^2A_F}{dt^2} \sim \frac{A_F}{\tau^2_{LS}}, \tag{2.22}$$

$$\frac{dA}{dt} \cong \frac{dA_F}{dt} \sim \frac{A_F}{\tau_{LS}}$$

Here we define τ_{LS} as the time scale on which the large-scale forcing varies, and we assume that A varies on the same time scale. With this scaling we find that the first term on the left-hand side (lhs) of (2.19) is negligible compared with the third term on the lhs if

$$\frac{\tau_{adj}}{\tau_{LS}} \ll 1, \tag{2.23}$$

and the second term is negligible compared with the third term if

$$\left(\frac{\tau_{adj}}{\tau_{LS}}\right)\left(\frac{\tau_{adj}}{\tau_D}\right) \ll 1, \tag{2.24}$$

and the second term on the rhs is negligible compared to the first term on the rhs if

$$\frac{\tau_D}{\tau_{LS}} \ll 1. \tag{2.25}$$

According to (2.23) and (2.25), both τ_{adj} and τ_D should be much smaller than τ_{LS}, which is easy to understand. In addition, however, (2.24) implies that τ_D should not be significantly shorter than τ_{adj}. An interpretation of the latter condition is that if τ_D is very small compared to τ_{adj}, then cumulus kinetic energy is dissipated so efficiently that the convection cannot become vigorous enough to reduce A to its equilibrium value over time scale τ_{LS}. We conclude that when (2.23) - (2.25) are satisfied, (2.16) is a good approximation to (2.19), and the solution obtained by time integration of (1.10) and (2.3) with (2.13) should closely approximate the quasi-equilibrium solution given by (2.16) - (2.18).

2.3 Estimating the Value of α

To actually use this approach to parameterize the cumulus in numerical models, we need to know the values of α and τ_D. According to (2.14), α depends on η, ε, σ, and the cloud depth, which all vary with cloud type and even with time. However, as a first step, we shall test the scheme with a constant α.

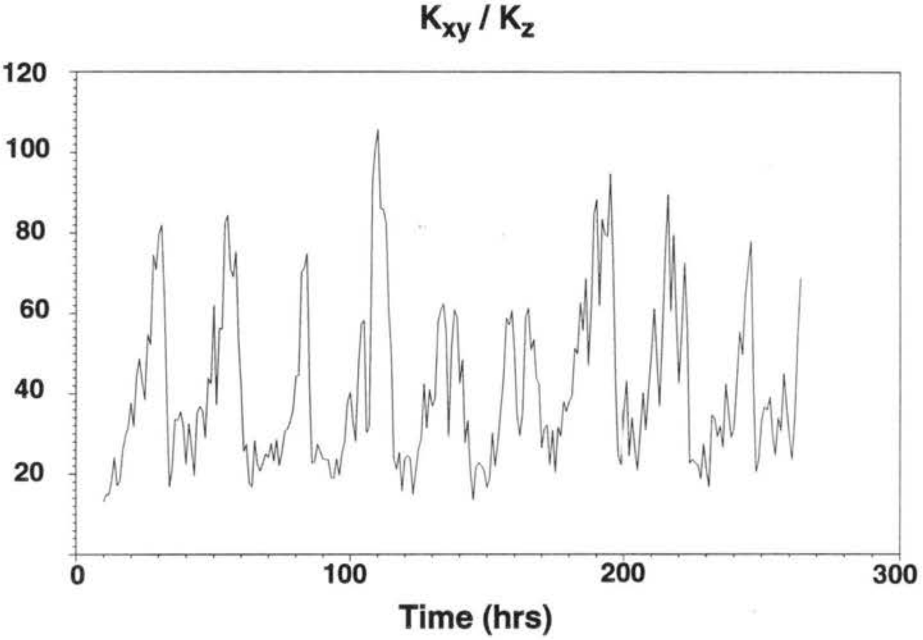

FIGURE 2.1: Time series of the ratio of the horizontal component (K_{xy}) of the eddy kinetic energy to the vertical component (K_z), from a CEM run.

To get a gross estimate of α, we used a set of Cumulus Ensemble Model (CEM) output from Xu's experiments to calculate ε. A CEM has a domain size comparable to a grid box of a GCM, but resolves individual clouds explicitly. This kind of model can provide data that we cannot obtain from observations, and is useful in studying the effects of cumulus convection on the large-scale environment. We can use either (2.13) or (2.14) to estimate α. Here we use the latter. Because cloud tops and bases (z_T and z_B) are not easy to define for the calculation of kinetic energy, the vertical integration is taken from the surface to the tropopause. A time series of K_{xy}/K_z (= $1/\varepsilon$ - 1) is shown in Fig. 2.1, from which we see ε is on the order of 10^{-2} or larger. The oscillation is due to the sinusoidal large-scale forcing prescribed in Xu's experiment. ε is smaller when the convection is stronger (the peaks in the figure). If we choose $\sigma \sim 0.01$, and take the integration over a depth of 10^4 m, we get $\alpha \sim 10^8\ \mathrm{m}^4\ \mathrm{kg}^{-1}$ from Eq (2.14). Keep in mind that the K_{xy}, K_z, and hence ε here refer to the eddies with respect to the whole domain, since it is not easy to distinctly define cloud types with the CEM outputs.

2.4 Summary and Discussions

In this chapter, we discussed the basic idea of the CKE approach. We relax the quasi-equilibrium assumption by explicitly using the CKE equation. To close the problem, we have to use (2.13), which relates M_B to CKE. The steady-state solution of this set of equation does reduce to cloud work function quasi-equilibrium.

This approach greatly simplifies the calculation procedure. This simplification further allows more detailed physics to be included, such as convective downdrafts and convection that originates from above the PBL. Bypassing the explicit definition of the large-scale forcing and the kernel does not only save computer time, it may also modify the way the cumulus convection interacts with the large-scale environment.

Our prognostic closure can be compared to the quasi-equilibrium closure in much the same way as a primitive equation (PE) model is related to a quasi-geostrophic (QG) model. A PE model can produce QG motion by explicitly simulating the geostrophic adjustment process. A PE model is in some respects simpler than a QG model; for example, the QG model determines the vertical motion field through the inconvenient "ω equation," while PE models typically determine the vertical velocity from the much simpler continuity equation. The use of a PE model does not imply a rejection of the idea that the large-scale motions of the atmosphere are approximately geostrophic.

Similarly, our prognostic closure can produce a quasi-equilibrium between the large-scale forcing and the convective response by explicitly simulating the conversion of convective instability into CKE. As explained earlier, the prognostic closure is simpler than the quasi-equilibrium closure; for example, quasi-equilibrium closure entails a "kernel" calculation, while the prognostic closure does not. The use of our prognostic closure does not imply a rejection of the quasi-equilibrium hypothesis.

Just as the study of the geostrophic adjustment process has led to improved understanding of geostrophic motion, the study of our prognostic closure may yield better understanding of the physical basis of quasi-equilibrium.

We have tried to estimate the value of α, assuming τ_D can be well chosen. However, it is not easy to distinctly define cloud types with the CEM outputs, we have thus used only the total CKE in the estimation. Can the estimated number be used for a single cloud type as Eqs (2.3), (2.13), and (1.10) are for? We shall try to answer this question by conducting numerical experiments. In the following chapter, we report results of some simple tests with a 1-D (one-dimensional) model. With these simple experiments, we hope to explore the dependency of the results on the parameters α and τ_D. We try to determine appropriate numbers for these parameters by the sensitivity tests. The method is then used to simulate the GATE observations. Some results from CSU GCM tests will be presented next.

CHAPTER 3

Testing the CKE Approach Using a One-Dimensional Model

We have discussed the CKE approach in the preceding chapter. We relax the quasi-equilibrium of cloud work function by using the prognostic CKE closure. Analysis shows that the steady-state solution reduces to that of the cloud work function quasi-equilibrium regardless of the values of α and τ_D. The purpose of this chapter is to test the prognostic CKE approach using a simple one-dimensional model in simple numerical experiments to analyze the parameterized cumulus convection.

Since we do not know how to formulate α and τ_D at this point, they are treated as disposable parameters and all cumulus subensembles share the same values of α and τ_D. We will demonstrate the feasibility of this approach and investigate the sensitivity of our results to α and τ_D.

3.1 Model Description

The 1-D model is a simplified version from the CSU GCM, obtained by assuming horizontal homogeneity. Large-scale vertical motion and horizontal advection can be prescribed as forcing terms.

The cumulus effects on the large-scale moist static energy ($\bar{h}$) and moisture ($\bar{q}$) can be written as

$$\left(\frac{\partial \bar{h}}{\partial t}\right)_{cu} = g\frac{\partial}{\partial p}M_c(h_c - \bar{h}), \tag{3.1}$$

and

$$\left(\frac{\partial \bar{q}}{\partial t}\right)_{cu} = g\frac{\partial}{\partial p}M_c(q_c - \bar{q}) - C, \tag{3.2}$$

where C is the net condensation. h_c and q_c can be obtained provided λ and the PBL properties, q_M and h_M are known. λ is calculated using the condition that clouds lose their buoyancy at certain model levels. $M_c(z, \lambda)$ can be obtained if $M_B(\lambda)$ is known. A closure is needed to obtain M_B. Eqs. (3.1) and (3.2) can be re-written in the forms of (1.7) and (1.8), which explicitly display the detrainment and subsidence warming and drying effects.

The mechanisms other than cumulus convection that can change the moisture and temperature at a certain level include dry convective adjustment (DCADJ), moist convective adjustment (MSTADJ), and large-scale Saturation Precipitation (LSP). Of course, radiation also can change the temperature. Surface sensible and latent heat fluxes have direct effects only on the PBL. In addition, the layer just above the PBL allows an exchange of moisture and entropy with the PBL, due to PBL-top entrainment. I will briefly discuss these processes in the following sections.

3.1.1 Vertical Discretization and Time Differencing

The experiments were performed with a 9-layer model. The model uses a normalized pressure as the vertical coordinate with a staggered grid. The large-scale temperature and water vapor mixing ratio are predicted in the middle of model layers, while the cloud properties are calculated on layer edges as implemented by Lord *et al.* (1982). Divergence of the heat and moisture fluxes by cumulus clouds, through layer edges, modify the temperature and mixing ratio of the layer. The grid variables' arrangement and cumulus fluxes are shown in Fig. 3.1.

To use the CKE scheme in a numerical model, we combine (2.1) and (2.13) to get

$$\frac{dM_B}{dt} = \frac{A}{2\alpha} - \frac{M_B}{2\tau_d}, \tag{3.3}$$

where the first term on the right hand side comes from the CKE generation term. We discretize (3.3) by applying the forward scheme on the generation term and the backward implicit scheme on the dissipation term. This gives

$$\frac{M_B^{n+1} - M_B^n}{\Delta t} = \frac{A^n}{2\alpha} - \frac{M_B^{n+1}}{2\tau_d}, \tag{3.4}$$

where superscripts n and $n+1$ denote time levels, and Δt is the time step for the integration. The time step is chosen small enough to maintain numerical stability.

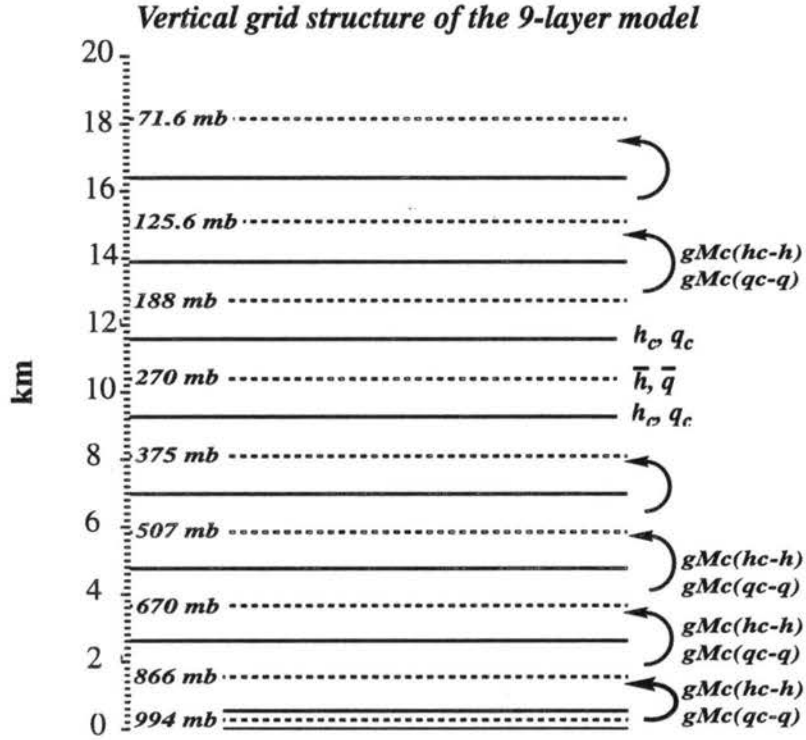

FIGURE 3.1: Vertical grid structure of the 9 - layer model. Solid lines (—) are layer edges, and dashed lines are layer centers. $\bar{h}$ and $\bar{q}$ are staggered with respect to h_C and q_C. Vertical transport of moist static energy and mixing ratio are indicated by arrows.

3.1.2 Some Other Features of the Cumulus Parameterization

Following Lord (1978), there are three phases of water in the model: water vapor, liquid water, and ice. Moist static energy is defined so as to include the effects of ice. Ice formation in clouds is a linear function of cloud temperature between -10°C and -40°C. When the temperature in clouds is above -10°C, all condensate is liquid water. Ice starts to form when the temperature goes below -10°C, and only ice exists when the temperature is lower than -40°C. All detrained condensate from cumulus clouds is subject to immediate evaporation. On the other hand, when the environment is supersaturated with respect to ice, the excessive environmental vapor is assumed to sublimate before being entrained into the clouds.

The calculation of the cloud work function does not take into account water loading effects. Details of the cloud model are included in Appendix A.

3.1.3 Large-Scale Saturation Precipitation

As discussed in Chapter 1, anvil clouds have strong and long-lasting radiative effects and must be included in a GCM. A large-scale saturation precipitation (LSP) parameterization is used to grossly represent the existence of anvils. Whenever supersaturation occurs, the temperature and water vapor mixing ratio are adjusted to a saturated state. The surplus of the liquid water or ice after the adjustment falls. The falling condensates can either evaporate or reach the ground as surface precipitation. This parameterization has been widely used to avoid large-scale supersaturation and is especially necessary when all the condensates detraining from cumulus clouds evaporate and tend to cause supersaturation aloft. Radiative effects then can be parameterized according to the thickness of the stratiform clouds. The assumption that cumulus-detrained condensates evaporate, and that LSP drains the condensates is an example of unrealistic coupling as discussed in Chapter 1. In this case, the LSP should be considered as part of the cumulus process in the model.

3.1.4 Moist Convective Adjustment

MSTADJ is used to avoid possible local moist convective instability beyond that which is removed by the cumulus scheme. MSTADJ is triggered whenever any two adjacent layers show static instability and at least one of the layers is supersaturated. MSTADJ then mixes two layers in potential temperature and mixing ratio. The final adjusted-state is statically neutral and without supersaturation. For simplicity this process is turned off in our 1-D experiments. After all, we already have DCADJ to prevent static instability and the cumulus scheme to take moist convective instability away.

3.1.5 Dry Convective Adjustment

DCADJ is employed to avoid unstable temperature lapse rates. Dry convection is assumed to happen in a much shorter time scale than moist convection. For this reason, DCADJ is applied before the cumulus scheme. Whenever local dry convective instability occurs, the potential temperature and water vapor mixing ratio of two layers are mixed, and a neutrality is obtained. The DCADJ is turned off in our 1-D experiments because the abrupt mixing of water vapor between layer often causes noise. It turns out that this process can be ignored in our 1-D experiments.

3.1.6 The Planetary Boundary Layer (PBL)

Following Suarez et al. (1983), the PBL is treated as a bulk entity. The top of the PBL is a model layer edge but is allowed to move (change its pressure and height) with time due to PBL-top entrainment, the cumulus mass flux, or large-scale convergence/divergence. The PBL conservation equations for mass, moist static energy, and mixing ratio are written as:

$$\frac{\partial \pi}{\partial t} + \nabla \bullet (\pi v_M) = (\pi \dot{\sigma})_{\sigma = 1} = g(E - M_B), \quad (3.5)$$

$$\frac{\partial}{\partial t}(\pi h_M) + \nabla \bullet (\pi v_M h_M) = g[(E - M_B) h_{B+} - M_B (h_M - h_{B+})] + S_h, \quad (3.6)$$

$$\frac{\partial}{\partial t}(\pi q_M) + \nabla \bullet (\pi v_M q_M) = g[(E - M_B) q_{B+} - M_B (q_M - q_{B+})] + S_q, \quad (3.7)$$

where E is the PBL-top entrainment, subscript $B+$ denotes the level just above the transition zone, and subscript M denotes a vertical mean through the PBL. S_h and S_q are the surface fluxes and radiation terms. σ is the normalized pressure, and $\dot{\sigma} = \frac{d\sigma}{dt}$. $\sigma = 1$ is the PBL top. π is the pressure depth of the PBL, and v is the horizontal velocity.

Originally, the CSU GCM, following Suarez et al. (1983), used (3.6) and (3.7) by taking (for weak M_B)

$$h_{B+} = h_L \text{ and } q_{B+} = q_L \text{ for } E - M_B > 0, \quad (3.8)$$

and for strong M_B

$$h_{B+} = h_M \text{ and } q_{B+} = q_M \text{ for } E - M_B < 0. \quad (3.9)$$

Here h_L and q_L are the values in the layer just above the PBL. The cumulus feedback in the model was originally written in the form of (1.7) and (1.8), which are not consistent with the flux forms of (3.6) and (3.7) for the PBL. Using (3.8) and (3.9) in (3.7) gives

$$\frac{\partial}{\partial t}(\pi q_M) + \nabla\bullet(\pi v_M q_M) = g(Eh_L - M_B q_M) + S_h, \text{ for } E-M_B > 0, \tag{3.10}$$

and when M_B is strong

$$\frac{\partial}{\partial t}(\pi q_M) + \nabla\bullet(\pi v_M q_M) = g(Eq_M - M_B q_M) + S_h, \text{ for } E-M_B < 0. \tag{3.11}$$

The equations for h_M take a similar form. This approach guarantees conservation of $\overline{h}$ and $\overline{q}$, but is not physically realistic. However, when convection is strong, the model tends to moisten the PBL and produce an extremely dry layer just above the PBL. (Compare Eq 3.11 to Eq 3.10, where gEq_M is usually much larger than gEq_L.)

To solve this problem, we rewrite the cumulus feedback in flux form — (3.1) and (3.2), which easily couples the PBL equations — (3.6) and (3.7). We then reduce (3.6) and (3.7) to

$$\frac{\partial}{\partial t}(\pi h_M) + \nabla\bullet(\pi v_M h_M) = g(Eh_{B+} - M_B h_M) + S_h, \tag{3.12}$$

and

$$\frac{\partial}{\partial t}(\pi q_M) + \nabla\bullet(\pi v_M q_M) = g(Eq_{B+} - M_B q_M) + S_q. \tag{3.13}$$

For the values at B+, the upstream scheme is used:

$$h_{B+} = h_L \text{ and } q_{B+} = q_L \text{ for } E > 0, \tag{3.14}$$

$$h_{B+} = h_M \text{ and } q_{B+} = q_M \text{ for } E < 0. \tag{3.15}$$

For simplicity in our 1-D experiments, we assume a constant PBL depth and $\nabla \bullet \pi v_M = 0$. From (3.5), we have $E = M_B$. Then (3.6) and (3.7) reduce to:

$$\frac{\partial}{\partial t}(\pi h_M) = -gM_B(h_M - h_{B+}) + S_h, \tag{3.16}$$

$$\frac{\partial}{\partial t}(\pi q_M) = -gM_B(q_M - q_{B+}) + S_q. \tag{3.17}$$

3.2 Experiments with a constant radiative Cooling

The purpose of our experiments is to test the cumulus scheme discussed in Chapter 2. The simplest way to generate convective instability is to impose a differential cooling of the atmosphere relative to the surface. We can do this by fixing the surface temperature while cooling the atmosphere at a constant rate. Observations show that the net radiative heating rate in the atmosphere without cloud cover is approximately -2 K day^{-1} at all elevations (e.g. Frank, 1976). Therefore, it is reasonable to experiment with a 2 K day^{-1} cooling rate.

With a fixed surface temperature, a constant 2 K day^{-1} cooling is a constant destabilizing effect which promotes cumulus convection. To reach a steady state, the radiative cooling must be balanced by the cumulus-induced subsidence warming. Meanwhile, the supply of water vapor to higher levels by cumulus detrainment makes the environment moist enough to allow cumulus convection.

3.2.1 Experiment Design

We fixed the PBL depth and the surface temperature at 60 mb and 299 K, respectively. The PBL wind speed was set at 7.5 m s^{-1}. There is no large-scale vertical motion or advection so that the 2 K day^{-1} radiative cooling along with the surface evaporation and sensible heat flux are the only destabilizing effects.

To reach a steady state, the model has to satisfy two integral constraints — the total diabatic heating must balance the 2 K day^{-1} cooling, and total surface evaporation must balance the total precipitation. In other words, the steady state should satisfy

$$\mathcal{E}_0 = \frac{1}{g}\int_{p_S}^{p_T} C(p)\,dp = P_0, \tag{3.18}$$

and

$$\frac{1}{g}\int_{p_S}^{p_T} c_p(-R)\,dp = L \bullet P_0 + \mathcal{S}_0, \tag{3.19}$$

where $\mathcal{E}_0$ is the surface evaporation rate, $\mathcal{S}_0$ is the surface sensible heat flux, both calculated by aerodynamic formulas. $\mathcal{E}_0$ depends on surface temperature, wind speed, and PBL mixing ratio. $\mathcal{S}_0$ depends on surface and PBL temperature. R = -2 K day^{-1} is the prescribed radiative cooling rate. P_0 is the total precipitation rate. p_S and p_T are the pressures at the surface and top of the model, respectively.

For all the other layers, we have

$$\left(\frac{\partial T}{\partial t}\right)_{Total} = -R = \left(\frac{\partial T}{\partial t}\right)_{Cu} + \left(\frac{\partial T}{\partial t}\right)_{LSP} + \left(\frac{\partial T}{\partial t}\right)_{DCADJ}, \tag{2.26}$$

and for conservation of water vapor

$$\left(\frac{\partial q}{\partial t}\right)_{Cu} + \left(\frac{\partial q}{\partial t}\right)_{LSP} + \left(\frac{\partial q}{\partial t}\right)_{DCADJ} = 0. \tag{2.27}$$

3.2.2 Numerical Stability

We tried different values of α ranging from 10^9 to 10^6 m^4 kg^{-1}, with $\tau_D = 600$ s. Two different time-steps were used. The time-step for integrating the CKE equation was 450 s, while cumulus convection modified the environment once an hour. Our experiments show that the latter time-step is the key to numerical stability, for a given value of α. Noise starts to appear when α is 10^7 m^4 kg^{-1} or smaller, with a one-hour time step for the cumulus heating and drying. Experiments show that to reach a steady state for small α, we have to use a smaller time step. We chose time steps small enough to avoid numerical instability.

We can estimate the stability criterion as follows. For a time step much larger than τ_D, Eq. (3.3) reduces to $M_B \sim A \dfrac{\tau_D}{\alpha}$. Substituting this into (1.10) gives

$$\frac{dA}{dt} = \left(J \bullet \frac{\tau_D}{\alpha}\right) A + F. \tag{2.28}$$

Since $J < 0$, the first term on the right hand side of (2.28) is a damping term. Use of forward time differencing for the damping term gives $A^{n+1} = A^n \left(1 - |J| \dfrac{\tau_D}{\alpha} \Delta t\right)$. Numerical stability requires $-|J| \dfrac{\tau_D}{\alpha} \Delta t \le 2$. For $|J| \sim 10$ kg m^{-4} s^{-2}, $\tau_D = 600$ s and $\alpha = 10^7$ m^4 kg^{-1}, we need $\Delta t \le \dfrac{1}{3} 10^4 \sim 3000\ (s)$. Similarly, we have $\Delta t \le 300\ (s)$ for $\alpha = 10^6$ m^4 kg^{-1}. The time steps used are shown in Table 1.

3.2.3 Results

We started with an observed tropical sounding as the initial condition. The vertical distribution of the moist static energy is shown in Fig. 3.2. Since the large-scale forcing in the real world is very different from the idealized 2 K day^{-1} cooling, an adjustment is to be expected. In the beginning, the tallest clouds can only reach layer 3 of the model. Since we have fixed surface temperature and the given radiation keeps cooling the upper levels, clouds 2 and then 1 eventually emerge. Strong noise appears in the "transition" when a taller cloud type starts to emerge. This is a numerical problem caused by the inappropriate definition (identification) of cloud types, and will be discussed in Chapter 5. The model reaches a steady state after 50 ~ 100 days. Since we are using a constant "forcing" in this experiment, we are interested in the steady-state solution.

3.2.3.1 $\alpha = 10^8$ m^4 kg^{-1}

Compared to the initial condition, the steady-state for $\alpha = 10^8$ m^4 kg^{-1} has a deep dry layer at the lower atmosphere as shown in Fig. 3.3. Notice that the labels of the abscissa are much smaller than those in Fig. 3.2. The upper levels are close to neutrality.

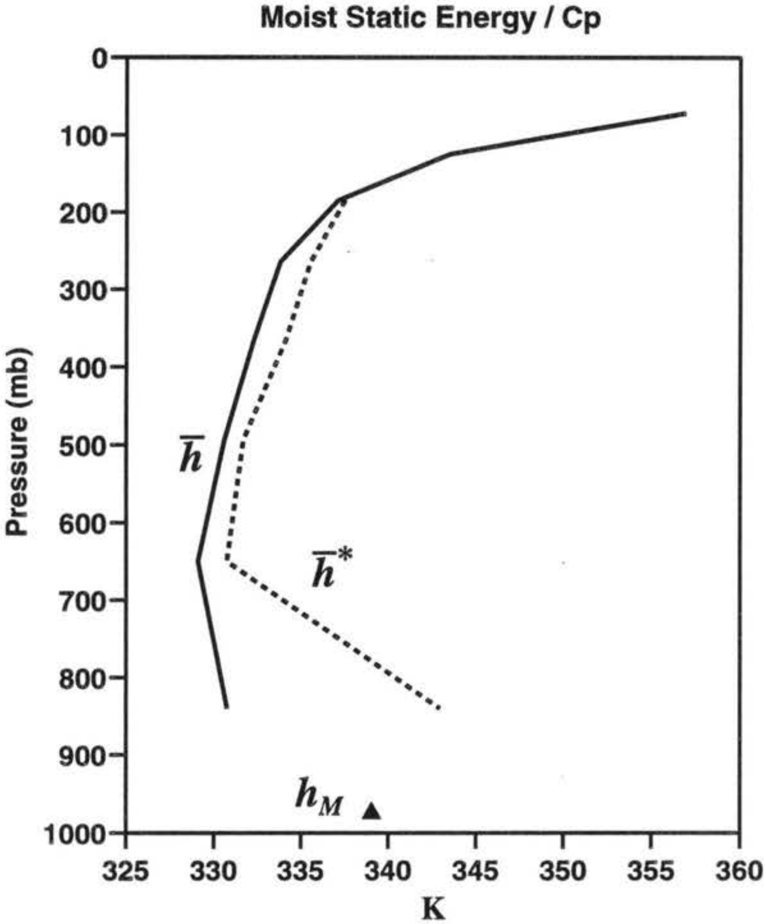

FIGURE 3.2: Initial condition in moist static energy ($\overline{h}$) and saturation moist static energy ($\overline{h}^*$). h_M is the $\overline{h}$ of the mixed layer. All have been divided by C_p and thus have units of K.

The LCL (lifting condensation level) is high and shallow clouds cannot survive. Since the cumulus clouds originate from the PBL which is dry, little condensation occurs to provide buoyancy for the ascending cumulus clouds. However, to balance the radiative cooling aloft, deep convection must exist. For deep convection to exist, the sounding at high elevations must be close to neutral, so that not much buoyancy is needed.

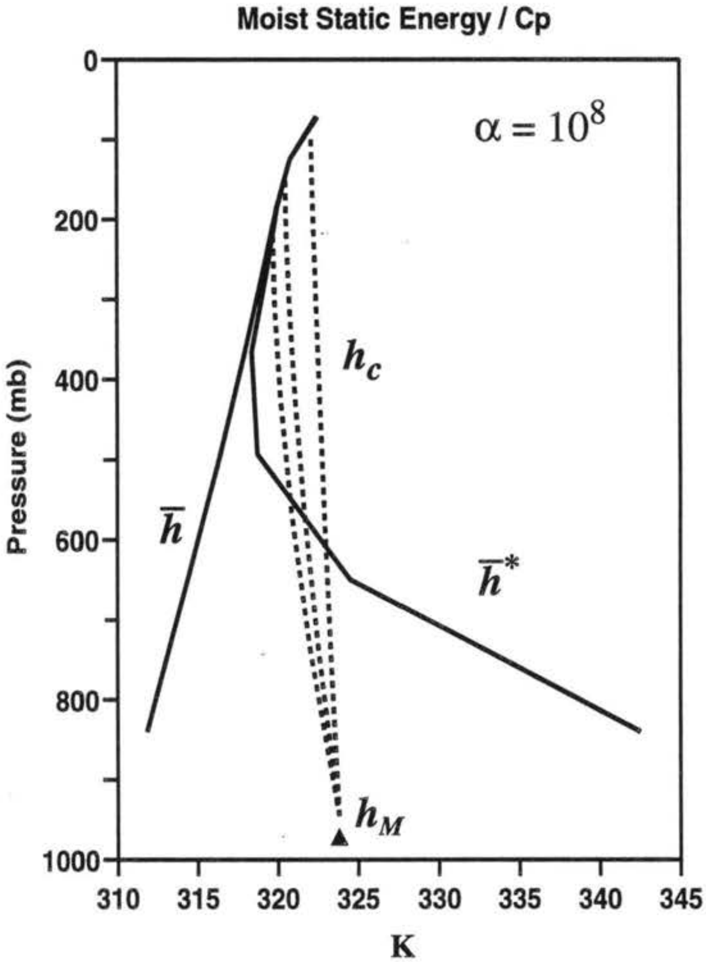

FIGURE 3.3: Steady-state moist static energy ($\bar{h}$), saturation moist static energy ($\bar{h}^*$), and h_c of the three active cloud types. $\alpha = 10^8\ m^4\ kg^{-1}$ is used. The solid triangle represents the moist static energy of the PBL (h_M). All have been divided by C_p and thus have a unit of K.

The cumulus-induced subsidence warming depends on both the static stability of the environment and the cumulus mass flux. The near neutrality at the upper levels must be associated with a large cloud-base mass flux in order for the subsidence warming to balance the radiative cooling.

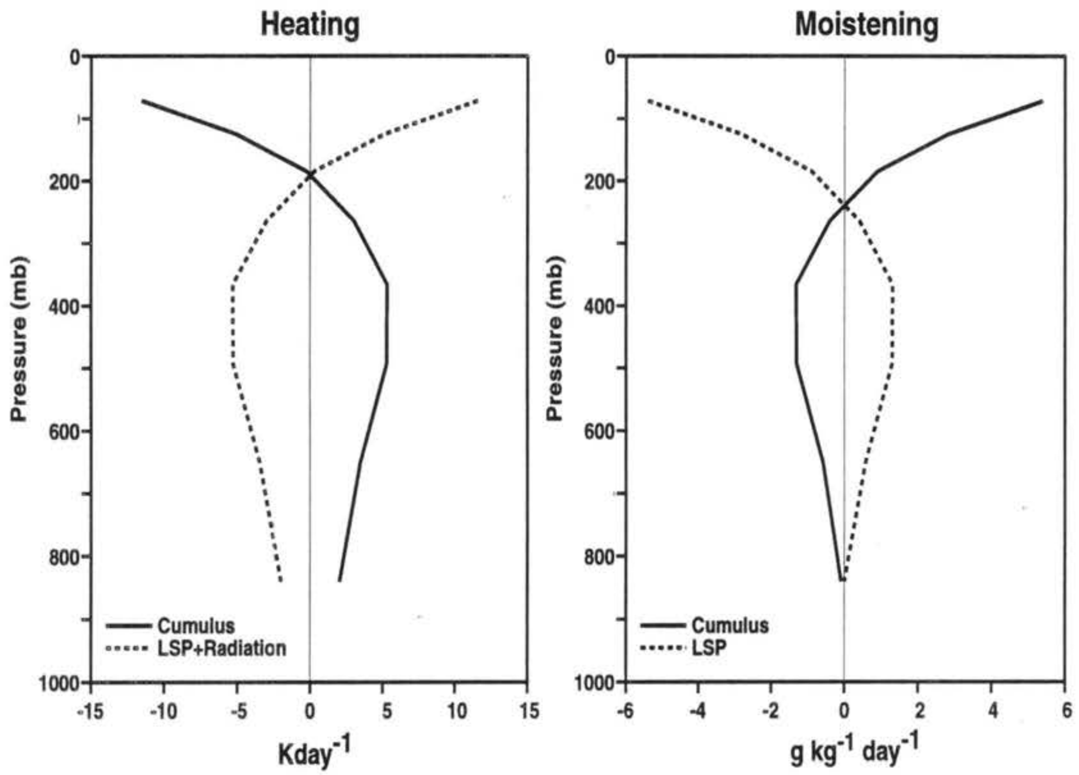

FIGURE 3.4: Steady-state vertical distribution of heating (left) and moistening. Solid lines are cumulus and dashed lines are LSP. The radiation cooling has been included in the LSP heating in the figure.

Also shown in Fig. 3.3 are the profiles of moist static energy of the three cloud types that are active in the steady state. We can see that the cloud moist static energy decreases with height due to the entrainment, and smaller entrainment corresponds to taller clouds. Shallower clouds do not have positive cloud work functions and hence do not exist. The positive cloud work function for the three cloud types may not be obvious by looking at profiles of h_c and $\bar{h}^*$ alone, because the mass flux of an entraining cloud increases with height.

The cumulus heating, as shown in Fig. 3.4, has a maximum in the middle layers. Very strong evaporative cooling (relative to the heating maximum) occurs in the highest layers of the model. LSP heating (plus the radiative cooling) has the exactly opposite vertical distribution. LSP condenses the evaporated condensates detrained by cumulus convection and causes warming at the high levels, the liquid water then falls to lower layers, re-evaporates and causes cooling. Cumulus heating (cooling) must balance LSP plus the radiative cooling in the steady state. In the PBL (not shown), where no LSP evaporation is allowed, the surface sensible heat flux is the mechanism to balance the cumulus heating.

The vertical distributions of LSP heating and drying must be identical, since the LSP process conserves moist static energy in each layer; the loss (gain) of water vapor must be associated with the gain (loss) of heat. LSP is the only mechanism to balance the drying (moistening) caused by cumulus convection in our experiments. Therefore, the cumulus moistening profile coincides with the cumulus heating profile, except horizontally shifted because of the radiative cooling. In particular, the height of the maximum cumulus drying coincides with the height of the cumulus heating maximum. This is different from observations in which usually the cumulus heating maximum is above the cumulus drying maximum. The vertical transport of latent energy, however, is reflected in the difference between the heights of zero cumulus heating and zero cumulus moistening.

Cumulus heating exactly balances the radiative cooling in the layer just above the PBL. All LSP liquid water falling from above has been completely evaporated before reaching this layer. (Hence, no large-scale precipitation occurs.) Without the evaporative cooling from falling large-scale precipitation, extra heating by the cumulus subsidence is "transferred" into the PBL where sensible heat flux is effective. This "transport" of heat is accomplished by the PBL-top turbulent mixing between these two layers.

Since the LSP cools by re-evaporating the falling liquid water, the cooling should decrease downward as the liquid water gradually runs out on the way down. The cumulus heating, therefore, also tapers to zero at the layer just above the PBL. For that reason, the shape of the heating profile of the cumulus convection in this experiment is largely determined by LSP. If we do not allow the re-evaporation of the falling liquid water from LSP, the heating profile of the cumulus will be a vertically-uniform 2 K day^{-1}, except for the uppermost few layers where LSP can still condense. This further demonstrates that the LSP is in some ways a (large-scale) "forcing" for the cumulus convection, and that how we represent the LSP in the model has direct impact on the parameterized cumulus convection. Meanwhile, the LSP is also a direct response to convective detrainment. This means that we cannot really separate forcing and response, as Arakawa and Schubert (1974) tried to do.

3.2.3.2 Dependence on α

Although the steady-state solution for M_B does not explicitly involve α as mentioned earlier, the steady-states of our numerical experiments do show significant dependence on α. This is because a part of the large-scale forcing is from the LSP which varies with α. The variation of LSP with α is, in turn, due to the dependence of M_B on α.

Starting with the same initial condition, a larger α gives a smaller cumulus mass flux. The cumulus-induced subsidence warming is smaller. Table 1 summarizes the steady-state conditions for different values of α.

a . Energy Balance

In the steady state, the sum of the surface sensible and latent heat fluxes should be approximately 225 W m^{-2}, which is also the vertical integral of the prescribed radiative cooling rate. We can see from Table 1 that most of the energy loss due to the prescribed radiation is balanced by the surface latent heat flux. The latent energy is transported from the surface into the PBL by evaporation and then from the PBL into the free atmosphere by cumulus convection in the form of water vapor. The water vapor is later transformed into heat by condensation in the process of cumulus convection. The surface evaporation rate is only determined by the mixing ratio of the PBL since the PBL wind speed and the sea surface temperature are fixed. Cumulus convection dries the lower free atmosphere and, through the PBL-top entrainment, it also indirectly dries the PBL. (Since we assume a constant PBL depth, with no large-scale convergence or divergence, the PBL-top entrainment mass flux actually equals the upward cumulus mass flux.) When the PBL is dry, the surface evaporation is strong.

The surface sensible heat flux can be either upward or downward, and mostly it is much smaller in magnitude than the latent heat flux. The sensible heat flux is downward for $\alpha = 10^8\ m^4\ kg^{-1}$ or smaller. When α is $3 \bullet 10^8\ m^4\ kg^{-1}$ or larger, the sensible flux becomes upward. The direction of the surface sensible heat flux reflects the difference between the surface air temperature and the sea surface temperature. When the sensible flux is upward, it helps balance the radiative energy deficit. When the sensible flux is downward, on the other hand, it cools the air and so works against the cumulus heating. However, since the sum of the sensible and latent heat fluxes must balance the total radiative energy loss, a stronger latent heat flux is needed when the sensible flux is downward. More latent energy means more vigorous cumulus convection. This is the case when α is small. In short, a smaller α results in a drier (lower relative humidity) and warmer steady-state PBL. The downward surface sensible heat flux becomes stronger, and so does the surface evaporation rate. The precipitation rate is larger and a stronger mass flux crosses the PBL top. As mentioned earlier, the stronger surface evaporation is associated with the drier PBL. The decrease of the precipitation rate due to the change of α from $10^8\ m^4\ kg^{-1}$ to $10^9\ m^4\ kg^{-1}$ amounts to 20%.

The large downward sensible heat flux must be associated with a large latent heat flux due to the constant "radiative" cooling of the atmosphere as a whole. In the meantime, the Earth's surface interacts directly only with the PBL, which then interacts with the free atmosphere. A large surface latent heat flux means a dry PBL, and a downward sensible heat flux means a warm PBL. Therefore, in our experiments, a dry PBL usually goes with a high temperature, and vice versa. The PBL moist static energy is thus almost a constant.

α (m^4 kg^{-1})	$\alpha = 10^9$	$\alpha = 3*10^8$	$\alpha = 10^8$	$\alpha = 3*10^7$	$\alpha = 10^7$	$\alpha = 3*10^6$	$\alpha = 10^6$
gM_B (mb hr^{-1})	3.12	4.24	5.44	6.63	7.46	8.34	8.67
q_M (g kg^{-1})	11.63	10.25	9.17	8.35	7.91	7.52	7.4
Δq (g kg^{-1})	-8.54	-7.15	-6.10	-5.31	-4.93	-4.60	-4.55
S.H. (W m^{-2})	33.0	4.8	-16.7	-33.0	-42.8	-51.8	-55.3
L.H. (W m^{-2})	193	220	242	258	268	277	280
Surface air temp. (K)	294.84	298.40	301.11	303.16	304.38	305.48	305.91
h_M / C_p (K)	324.0	324.1	324.1	324.1	324.2	324.4	324.0
Cu precip. (mm day^{-1})	6.61	7.56	8.30	8.86	9.19	9.50	9.60
Precipitable water (mm)	21.29	20.97	20.57	20.19	19.98	19.79	19.74
Cloud types active	1/2/3/4/5/6/7	1/2/3/4/5	1/2/3	1/2	1/2	1	1
Time step (s)	3600	3600	3600	3600	1200	300	150
A_1 (J kg^{-1})	5300	2800	1500	800	350	125	40
A_2 (J kg^{-1})	3500	1600	690	150	10	0	0
A_3 (J kg^{-1})	2600	1000	370	0	0	0	0
$\lambda_1 \bullet 10^{-5}$ (m^{-1})	2.15	2.10	2.12	2.12	1.81	2.39	1.9
$\lambda_2 \bullet 10^{-5}$ (m^{-1})	6.80	5.99	5.06	5.13	3.19	/	/

TABLE 1: Summary of experiments with different values of α from 10^6 to 10^9 m^4 kg^{-1}, and with τ_D = 600 sec. Listed variables are cloud-base mass flux, PBL specific humidity, jump of specific humidity across the PBL, surface sensible and latent heat flux, surface air temperature, moist static energy of PBL, cumulus precipitation, precipitable water, active cloud types and time step for numerical integrations. Cloud type 1 is the deepest cloud type possible in the model. Cloud types 2 and 3 detrain at the 2nd and 3rd highest levels in the model, and so forth. Also shown is the steady-state cloud work function for clouds 1, 2, and 3 and the fractional entrainment rate of clouds 1 and 2.

For the PBL, from (3.16) and (3.17), we have

$$\mathfrak{E}_0 = -M_B(q_M - q_{B+}), \tag{3.20}$$

and

$$-L \bullet \mathfrak{E}_0 + \mathfrak{S}_0 + c_p R = -M_B(h_M - h_{B+}). \tag{3.21}$$

As α becomes smaller, shallower clouds gradually disappear. Five types of clouds coexist when $\alpha = 3 \bullet 10^8\ \mathrm{m^4\ kg^{-1}}$. Three types of clouds are present when $\alpha = 10^8\ \mathrm{m^4\ kg^{-1}}$. Only the deepest cloud type survives when $\alpha = 3 \bullet 10^6\ \mathrm{m^4\ kg^{-1}}$ or smaller. Many active cloud types with $\alpha = 10^9\ \mathrm{m^4\ kg^{-1}}$ can be partly explained by the high relative humidity of the PBL. The PBL moist static energy is almost identical in all cases, although the relative humidity is very different. Compared to a smaller α, the deepest cloud must precipitate less because of the contributions from shallower clouds. For a unit cloud-base mass flux, same type of cloud precipitates more if originating from a PBL of higher relative humidity (e.g. the deepest clouds with $\alpha = 10^9\ \mathrm{m^4\ kg^{-1}}$ against those with $\alpha = 10^8\ \mathrm{m^4\ kg^{-1}}$). Again for the energy balance (latent energy released from precipitation), the cloud-base mass flux must be smaller with $\alpha = 10^9\ \mathrm{m^4\ kg^{-1}}$ than with $\alpha = 10^8\ \mathrm{m^4\ kg^{-1}}$.

b . Steady-state Environmental Sounding

Besides the energy balance, changes due to using different α's can also be seen in the steady-state soundings. Fig. 3.5 shows the moist static energy and saturation moist static energy for $\alpha = 10^7\ \mathrm{m^4\ kg^{-1}}$, $10^8\ \mathrm{m^4\ kg^{-1}}$, and $10^9\ \mathrm{m^4\ kg^{-1}}$, respectively. The

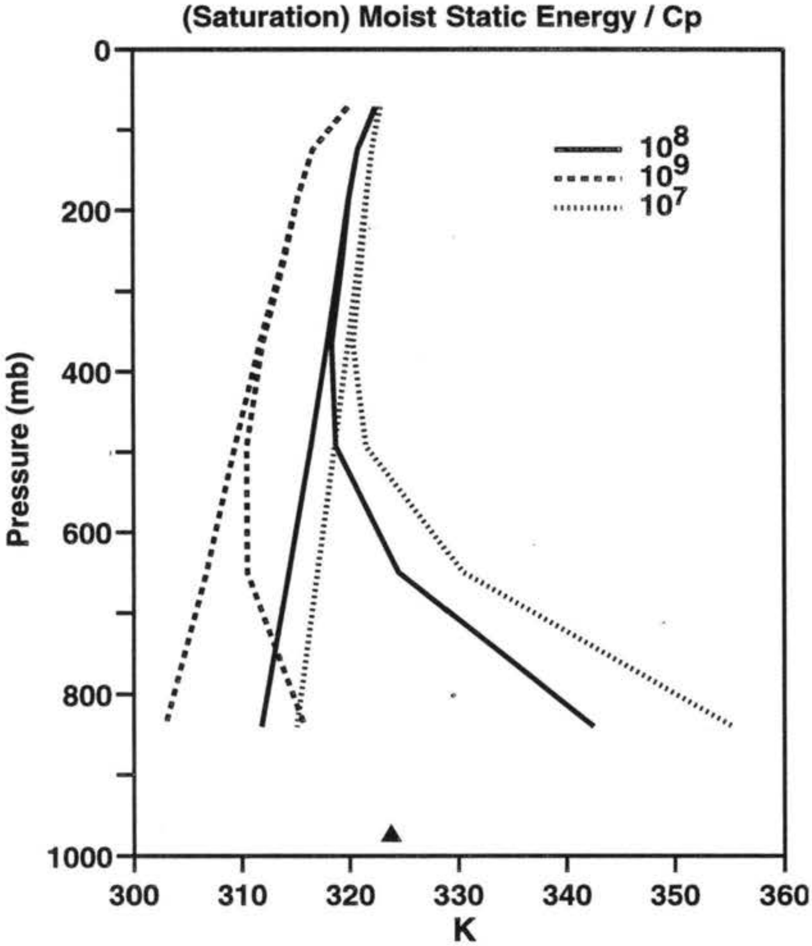

FIGURE 3.5: Moist static energy and saturation moist static energy for three different α's: 10^7 m^4 kg^{-1} (dotted lines), 10^8 m^4 kg^{-1} (solid lines), and 10^9 m^4 kg^{-1}. The solid triangle represents the moist static energy of the PBL (h_M), which are almost identical for all cases.

steady state strongly depends on the value we choose for α. When we use a larger α, the descent of the LCL along with the moistened PBL (as mentioned earlier) favors shallower convection.

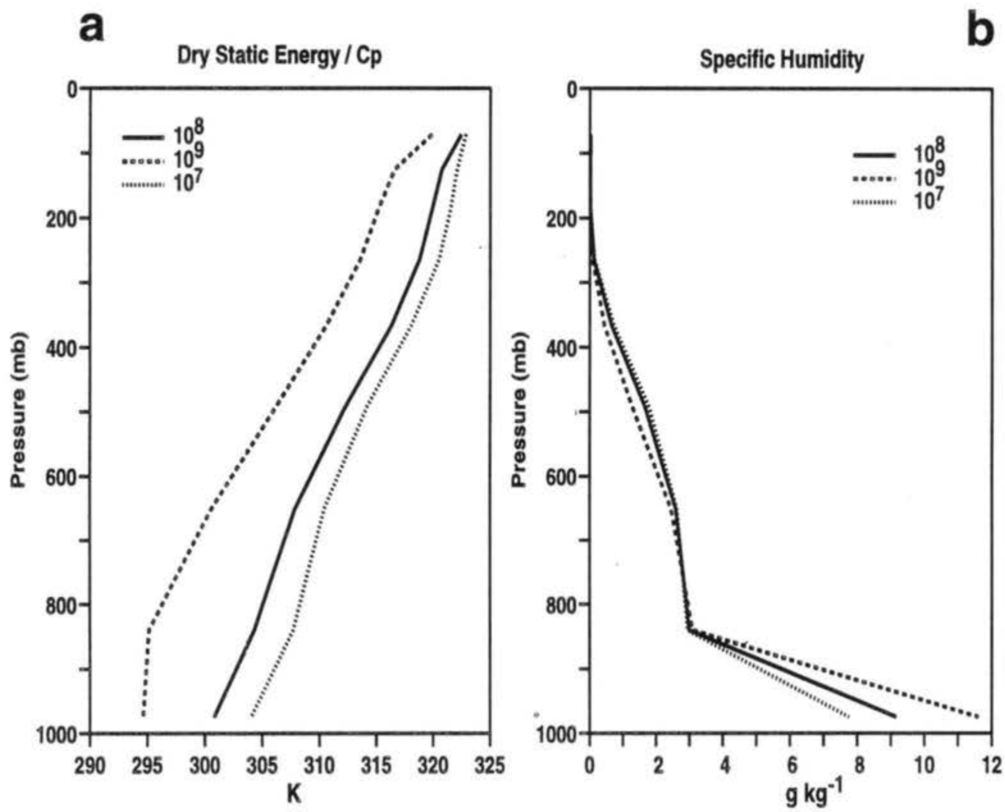

FIGURE 3.6: Steady-state dry static energy (a) and specific humidity for $\alpha = 10^7$ $m^4\ kg^{-1}$ (dotted line), $10^8\ m^4\ kg^{-1}$ (solid line), and $10^9\ m^4\ kg^{-1}$.

The differences in temperature and mixing ratio are shown in Fig. 3.6. The larger α leads to a colder atmosphere as a whole and, in the meantime, a stronger static stability. Higher relative humidity is associated with the lower temperature, since the mixing ratio is not very different except for in the PBL. The dramatic increase with α in the PBL relative humidity is obvious in the figure.

The colder atmosphere (especially with a PBL of high relative humidity) means more convective instability of the atmosphere with respect to the surface, while the stronger static stability means moist convection will be more efficient in subsidence warming. A smaller cumulus mass flux is needed to balance the same amount of radiative cooling.

When the environment is closer to saturation (higher relative humidity), LSP can reach the surface more easily. In a sense, this is closer to reality, since LSP can occur even when the whole grid box is only partially saturated. The low temperature is due to the weaker cumulus activity which causes less subsidence heating.

c. *Cumulus Heating/Moistening and LSP*

Differences caused by different α's can also be seen in the steady-state vertical distributions of cumulus and LSP heating and moistening. Fig. 3.7 compares the cumulus heating profile for $\alpha = 10^9$ m^4 kg^{-1} with that for $\alpha = 10^8$ m^4 kg^{-1}. Since the vertical profiles of these four fields are either the same or of opposite signs, we only show the profiles of cumulus heating here.

Both the cumulus cooling above 200 mb and the subsidence warming below are significantly reduced when $\alpha = 10^8$ m^4 kg^{-1} is replaced by $\alpha = 10^9$ m^4 kg^{-1}. The level of zero cumulus heating also descends. In order to maintain energy balance, the LSP condensation and re-evaporation must become weaker at the same time.

Despite the weakening of the cumulus and LSP heating, they can still manage to balance the radiative cooling. It seems to be unnecessary to evaporate liquid water, if LSP eventually recondenses it. This is an unrealistic interaction between the cumulus convection and the environment. In reality, the detrained condensates may not evaporate espe-

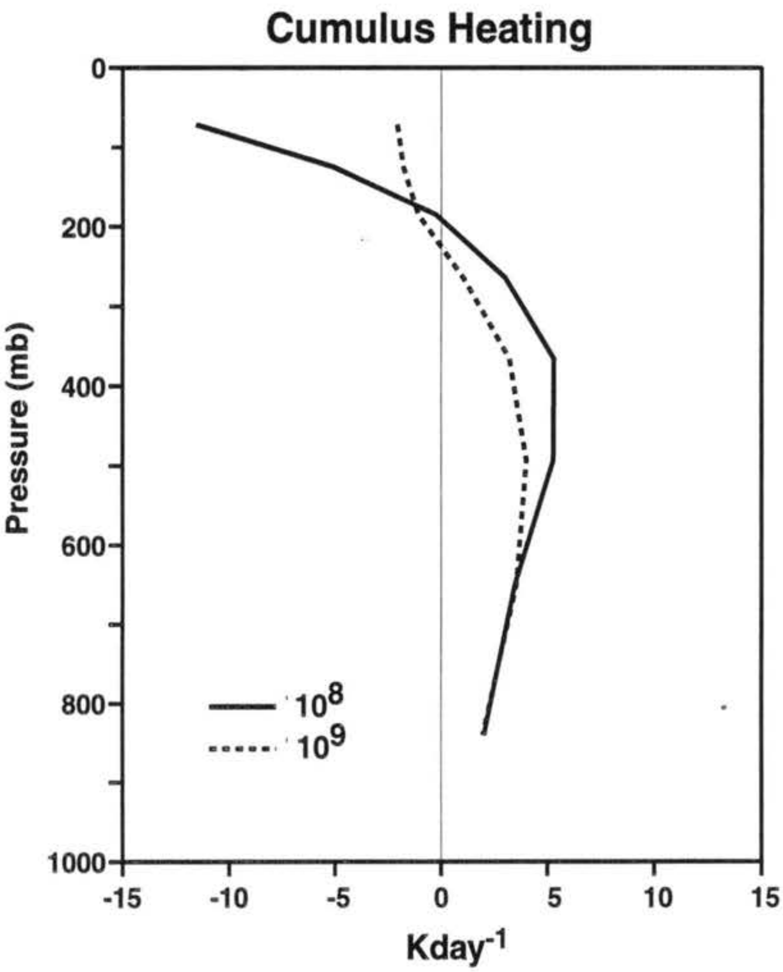

FIGURE 3.7: Cumulus heating in layers except the PBL for $\alpha = 10^8$ m^4 kg^{-1} (solid) and $\alpha = 10^9$ m^4 kg^{-1} (dash).

cially when the elevation is high and the temperature is low. On the other hand, the large-scale precipitation may occur even when the grid-box is only locally saturated.

3.2.3.3 Value of α

We have seen how the steady-state solutions depend on α. Can we infer, from what we have seen, that adopting a different α for each subensemble is better than a "one-α"

approach? From the formula we derived in Chapter 2, α is a function of cloud depth and hence it should vary with cloud type. However, can we see the significance of doing so? If yes, how should we do it? Since the formula shows that α depends on ε which may involve wind shear, the Richardson number that measures the relative size of the thermal and shear forcings for convection can be a candidate for parameterizing α.

The formula for α derived in Chapter 2 involves σ, ε, η, and the cloud depth. None of these variables are related to the large-scale variables in a simple way. Given a cloud model that can determine the cloud depth and η, we still cannot determine σ or ε.

We did a simple test to check the significance of using different α's for different sub-ensembles. We used a larger α of 5×10^8 m^4 kg^{-1} for the deepest three types of clouds and a smaller α of 10^8 m^4 kg^{-1} for all shallower clouds. These two numbers were chosen so that the steady-state precipitation rate and surface latent heat flux, etc. are close to those from a uniform $\alpha = 3 \times 10^8$ m^4 kg^{-1}. The steady-state cumulus heating rate is thus compared to that run and is shown in Fig. 3.8.

From Fig. 3.8, we see that the cumulus heating is stronger below because the mass flux of the shallow clouds increases. (Apparently, these shallow clouds do not detrain much moisture.) In the meantime, the cooling at high levels is weaker because the mass flux in the deepest three cloud types are reduced. There is a discontinuity in the heating profile in the 4th layer. It seems that the difference in the assigned α's for deep and shallow clouds is too large, or somehow inappropriate. The main structure of the cumulus heating profile is still mainly determined by the large-scale forcing. We therefore believe that the "one-α" approach is feasible to some degree.

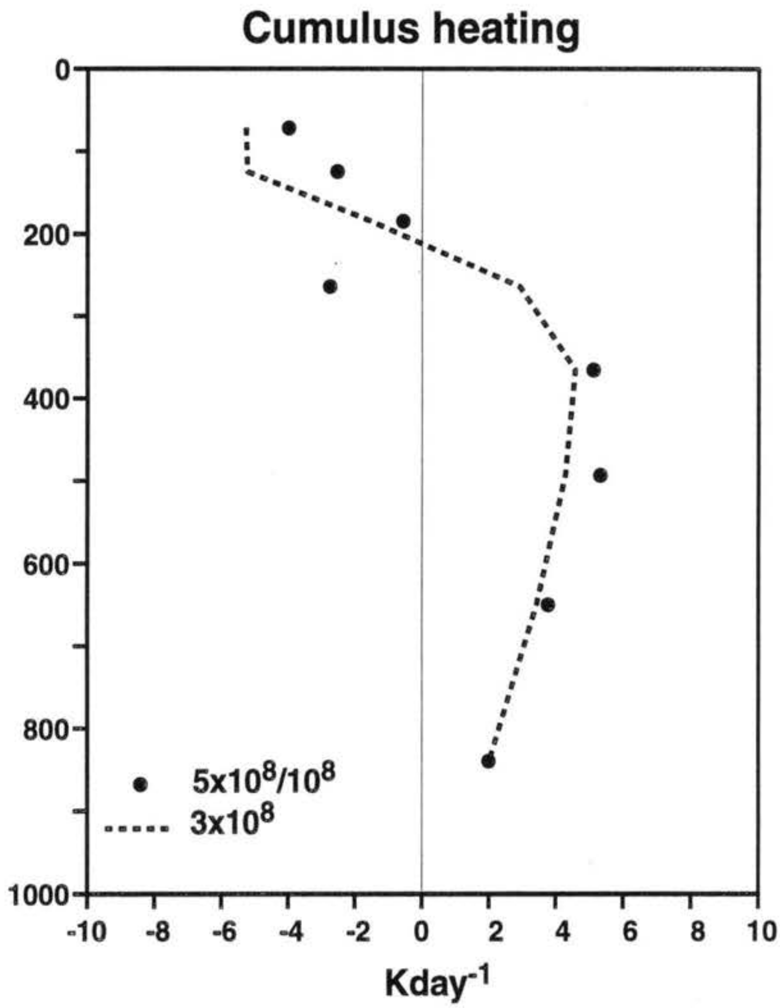

FIGURE 3.8: Cumulus heating using two α's: 5×10^8 m^4 kg^{-1} for deep clouds and 10^8 m^4 kg^{-1} for shallow clouds, compared to that from a uniform $\alpha = 3 \times 10^8$ m^4 kg^{-1} (dashed line).

3.2.3.4 Discussions

Here we try further to explain (interpret) the dependence of our results on the value of α. For a larger α, a unit cloud-base mass flux corresponds to a larger CKE from eq. (2.13). A larger CKE for unit cloud-base mass flux demands a larger cloud work function. A larger cloud work function means more potential energy available to be released for unit cloud-base mass flux. This, in turn, means larger absolute values of the kernels. In other words, the cumulus clouds have to be able to modify the environment more efficiently. In order to have a larger kernel, the steady-state sounding has to be more statically stable. When the static stability is larger, same mass flux results in stronger heating. However, for a unit mass to reach the same height when the static stability is large, more buoyancy is needed. More buoyancy can be acquired if the PBL mixing ratio is higher and/or the lower free atmosphere is wetter. Such low-level moistening can be achieved by having more shallow clouds. When the cumulus heating is more efficient and the large-scale forcing is the same, we expect less mass flux across the PBL top.

Although we do not explicitly assume quasi-equilibrium, the cumulus convection calculated using the CKE approach is still close to a quasi-equilibrium with the environment. After all, the mechanisms that can provoke cumulus convection are still the same and cumulus convection still consumes convective instability (cloud work function). A colder atmosphere with a wetter PBL gives a larger cloud work function. When the same radiative cooling is imposed on this environment, it provides a smaller "large-scale forcing" (the rate of increase in cloud work function). It should be true that the same radiative cooling will provoke weaker cumulus convection when the atmosphere is colder with a wetter PBL.

3.3 GATE Simulation

We have investigated the steady states under a constant large-scale forcing by imposing a constant radiative cooling rate, using the CKE approach. However, the large-scale forcing usually is a combination of many processes which vary with time. Also, it usually has a vertical structure, unlike the uniform 2K day^{-1} radiative cooling that we have used. A useful cumulus parameterization should be able to capture the time evolution of the cumulus activity and the vertical distributions of its effects on the environment, Q_1 and Q_2.

The GATE (Phase III, 1974) observations have been used to perform semi-prognostic tests by Lord (1982) and Kao and Ogura (1987), in which both the observed sounding and large-scale processes are inputted every hour, including the observed PBL moist static energy. Lord (1982) was able to closely reproduce the evolution of the precipitation, and the time average vertical distribution of Q_1 and Q_2, using the A-S scheme.

3.3.1 Experiment Design

We start with the sounding of September 2, 1974 of the GATE phase III observation. Observed hourly radiative heating from Cox and Griffith (1979) and moisture and temperature advection from Thompson and Reed (1979) are used. We rewrite (1.1) and (1.2) in pressure coordinates as

$$\frac{\partial T}{\partial t} + \boldsymbol{V} \bullet \nabla_p T + \frac{\omega}{C_P}\frac{\partial s}{\partial p} = \frac{Q_1}{C_P}, \qquad (3.22)$$

and

$$\frac{\partial q}{\partial t} + \boldsymbol{V} \bullet \nabla_p q + \omega\frac{\partial q}{\partial p} = -\frac{Q_2}{L}. \qquad (3.23)$$

Here Q_1 and Q_2 are defined as

$$Q_1 \equiv Q_R + L \bullet C - \frac{\partial}{\partial p}(\overline{\omega' s'}) , \tag{3.24}$$

and

$$Q_2 \equiv L \bullet C + L\frac{\partial}{\partial p}(\overline{\omega' q'}) . \tag{3.25}$$

All overbars have been omitted here, except for the eddy transport terms. The second and third terms on the left hand side of (3.22) and (3.23), as well as Q_R, can be obtained from hourly observations. (Q_1-Q_R) and Q_2 are calculated from the cumulus parameterization. We can, therefore, get the tendency of the temperature and mixing ratio.

We use an interactive PBL for the surface fluxes. In other words, no observed surface fluxes are inputted as forcing. The PBL mixing ratio and temperature are used as the cloud-base conditions. Cumulus convection modifies the PBL, and surface fluxes are calculated according to the PBL conditions using the bulk aerodynamic formulae. The surface fluxes, in turn, participate in determining the cloud-base condition. However, as in the experiment with constant radiative cooling, we use a fixed PBL depth and wind speed. The fixed 60 mb PBL-depth is close to what Lord (1982) used. The PBL wind speed is 7.5 m s^{-1}. We use τ_D = 600 sec and $\alpha = 10^8$ m^4 kg^{-1} or 10^9 m^4 kg^{-1}.

3.3.2 Results

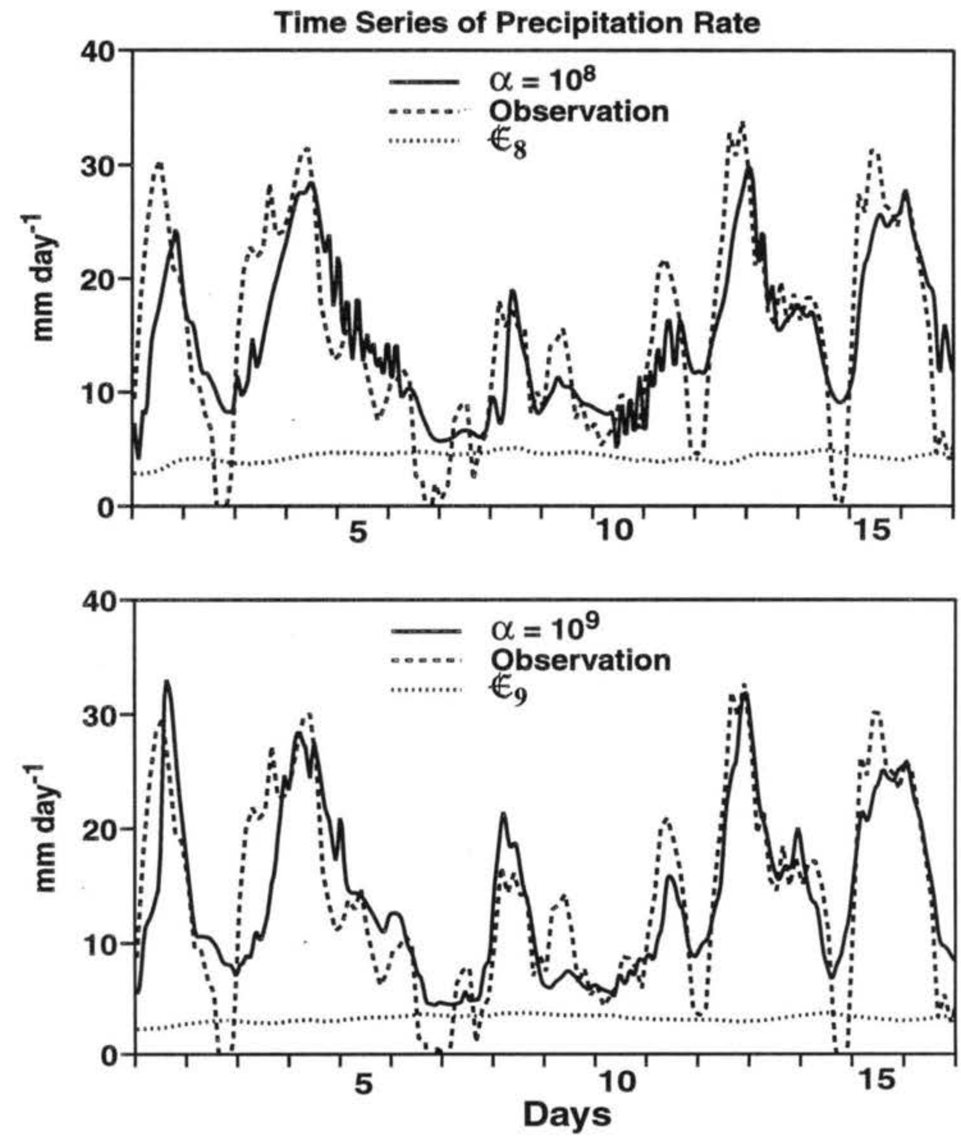

FIGURE 3.9: Simulated and GATE-observed precipitation rate and simulated surface evaporation. $\alpha = 10^8$ m^4 kg^{-1} (upper panel) and $\alpha = 10^9$ m^4 kg^{-1} have been used.

Since an arbitrary initial condition for CKE is used, we ignore the first three days as a spin-up of the model. Only the results of a 16-day simulation, which includes five major convective events, will be shown. The results are somewhat noisy due to the way the cloud type is defined. The noise becomes stronger especially when we use a smaller α, when the cumulus convection is more vigorous. To eliminate the noise, we try later to use λ rather than $\hat{p}$ as the cloud spectral parameter. We will discuss this in more detail in Chapter 5. In this chapter, we apply a 5-hour moving average in time, in the plots of Q_1, Q_2, and precipitation, to make the plots easier to read.

3.3.2.1 Precipitation

For convenience of comparison, the observed precipitation rate is obtained by vertically integrating Q_2. Since we do not have the observed surface evaporation, we use the simulated surface evaporation, instead. Because we have assumed constant wind speed, constant PBL depth, and constant sea surface temperature, we do not expect to have a very realistic simulation of the PBL. By using the simulated surface evaporation in the calculation of the "observed" precipitation simplifies the comparison between our results and the observations. Another set of observed precipitation will also be compared later.

The time evolution of the GATE-observed precipitation rate is generally well reproduced in the simulation. Fig. 3.9 compares the simulation with observations on the precipitation rate. Keep in mind that since we used the simulated surface evaporation in the "observed" precipitation, the "observations" are slightly different in the comparisons using different α's. The simulation tends to over-estimate the precipitation rate during the

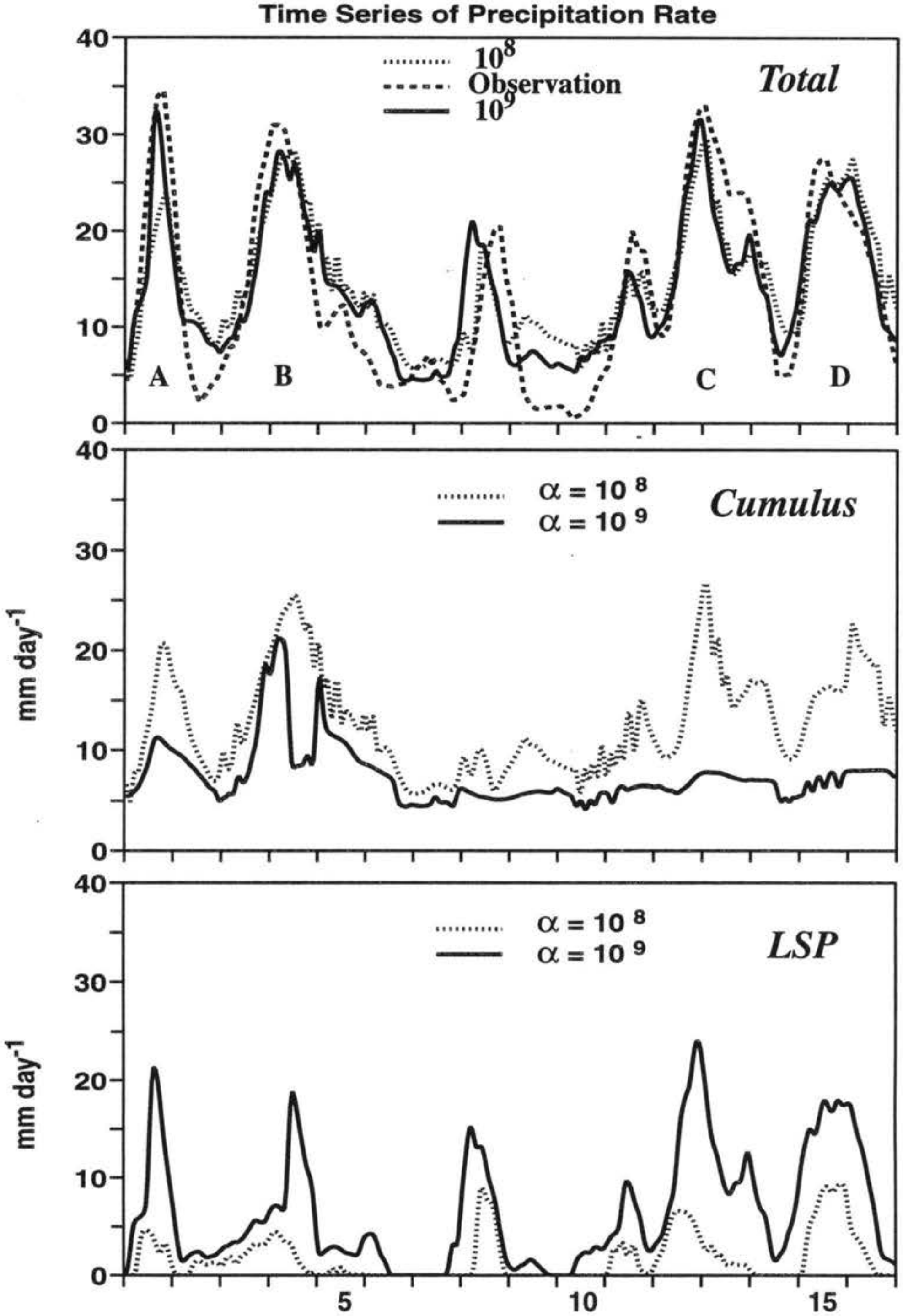

FIGURE 3.10: Simulated total precipitation rate compared with observation (dashed, from Lord, 1982) and the simulated precipitation from cumulus convection and LSP. The dotted and solid lines represent the results with $\alpha = 10^8$ m^4 kg^{-1} and $\alpha = 10^9$ m^4 kg^{-1}, respectively. Letters A, B, C, and D mark four major convective events to be discussed later.

"break" periods between major convective events, e.g the second day, between the 6th and 7th day, between the 11th and 12th day, and the end of 14th day. Generally, $\alpha = 10^9$ $m^4\ kg^{-1}$ seems to work better, except for the precipitation peak on the 8th day. The time-average total precipitation through the 16-day period is 15 mm day^{-1} for the "observation" and 14.6 mm day^{-1} for the simulation, when $\alpha = 10^8\ m^4\ kg^{-1}$. The corresponding figure is 13.8 mm day^{-1} for the "observation" and 14 mm day^{-1} for the simulation, when $\alpha = 10^9\ m^4\ kg^{-1}$. The surface evaporation is larger with $\alpha = 10^8\ m^4\ kg^{-1}$ than with $\alpha = 10^9\ m^4\ kg^{-1}$.

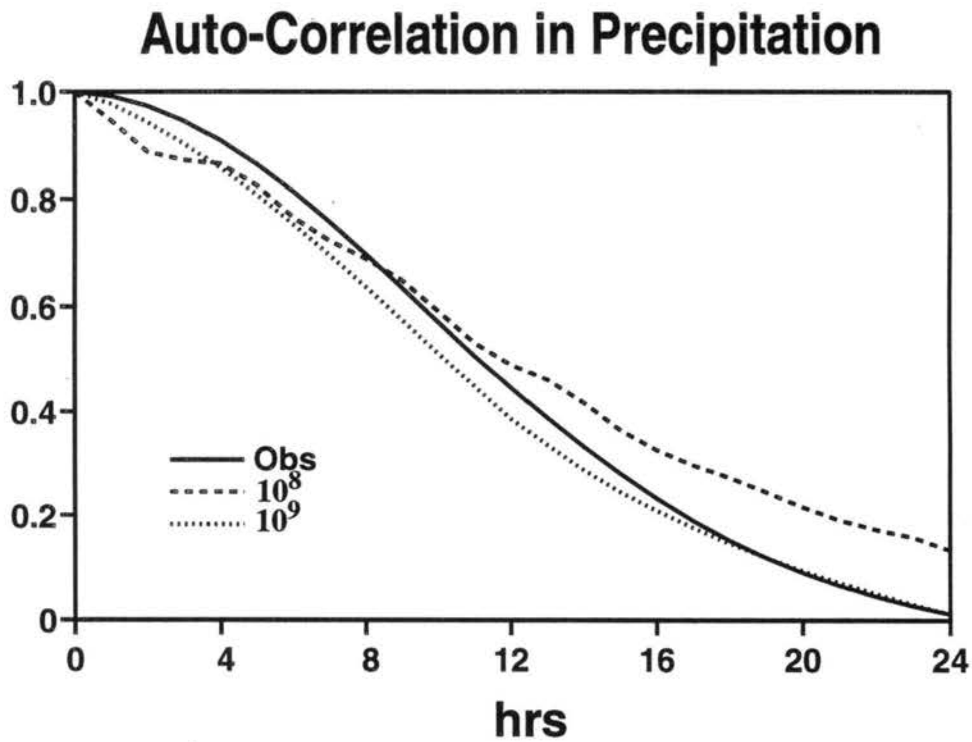

FIGURE 3.11: Auto-correlation of total precipitation rate with $\alpha = 10^8\ m^4\ kg^{-1}$, $\alpha = 10^9\ m^4\ kg^{-1}$, and observations.

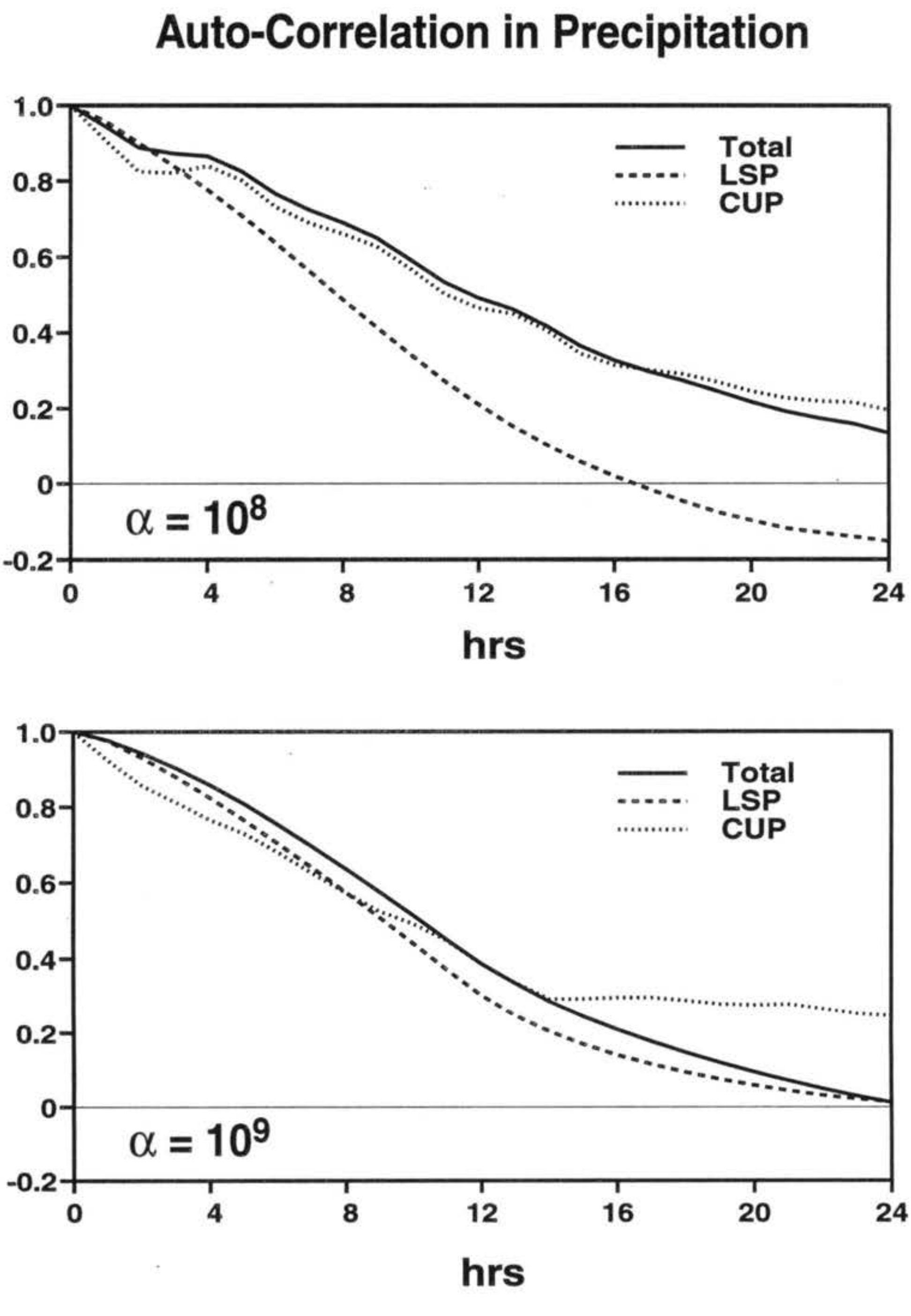

FIGURE 3.12: Auto-correlation of cumulus precipitation (CUP), LSP, and total precipitation for $\alpha = 10^8$ m^4 kg^{-1} and $\alpha = 10^9$ m^4 kg^{-1}, respectively.

The simulated surface evaporation is relatively constant with time, compared to the variation of the precipitation rate. The "observed" precipitation including this surface evaporation is negative at three points in the time series. This is similar to one of the observed precipitation data used in Lord (1982) in which they used Deardorff (1972)'s method to estimate surface evaporation.

Comparison with the radar-observed precipitation used in Lord (1982) is shown in Fig. 3.10. Also shown in Fig. 3.10 is the time evolution of the simulated LSP and cumulus precipitation, with $\alpha = 10^8$ m^4 kg^{-1} compared to $\alpha = 10^9$ m^4 kg^{-1}. For $\alpha = 10^8$ m^4 kg^{-1}, 91% of the precipitation comes from cumulus convection; while LSP contributes more than 41% of the total precipitation when $\alpha = 10^9$ m^4 kg^{-1} is used. Observations indicate that stratiform clouds contribute nearly 40% of the GATE precipitation (Cheng and Houze, 1979). The correlation coefficient is 0.85 for $\alpha = 10^8$ m^4 kg^{-1} and 0.88 for $\alpha = 10^9$ m^4 kg^{-1}. This suggests that $\alpha = 10^9$ m^4 kg^{-1} is a better choice.

When $\alpha = 10^9$ m^4 kg^{-1}, the variation of the cumulus convection with time is almost flat. The variation of the input advection and radiation is responded to by LSP, which is also a part of the large-scale forcing for the cumulus convection. These two parts largely compensate each other such that the total large-scale forcing for the cumulus convection does not vary much with time. As a result, the cumulus convection is less sensitive to the variation of the input observed large-scale processes.

We have mentioned the correlation coefficient between the simulated and the observed total precipitation, which both simulations showed better than 0.88. However, since the A-S parameterization assumes quasi-equilibrium, we also compare the simula-

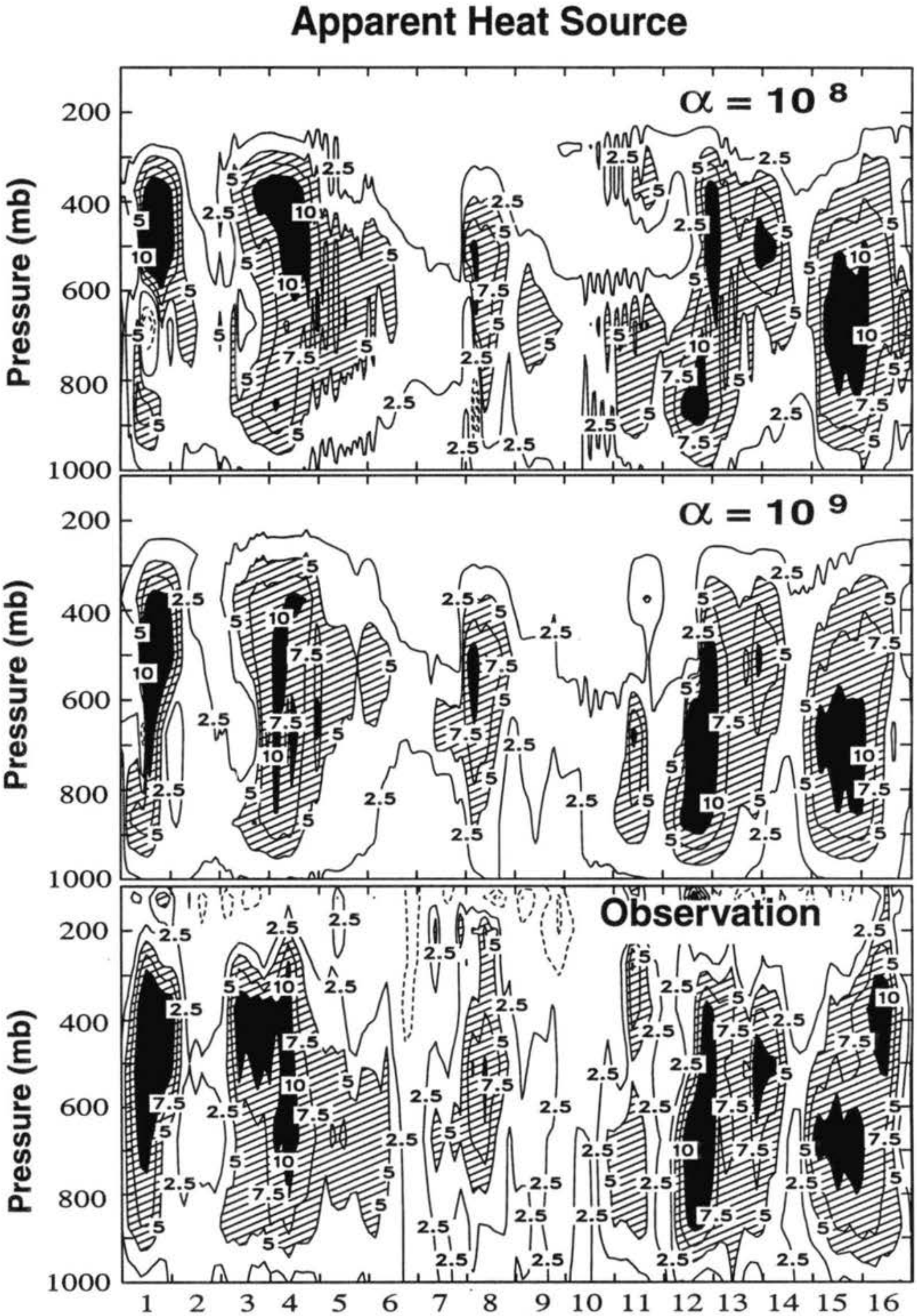

FIGURE 3.13: Apparent heat source (Q_1-Q_R) from simulations with $\alpha = 10^8$ m^4 kg^{-1}, $\alpha = 10^9$ m^4 kg^{-1}, and observations. Light-shaded areas are where the values are above 5 K day^{-1}, and dark-shaded above 10 K day^{-1}. The contour interval is 2.5 K day^{-1}. Dashed lines represent negative values.

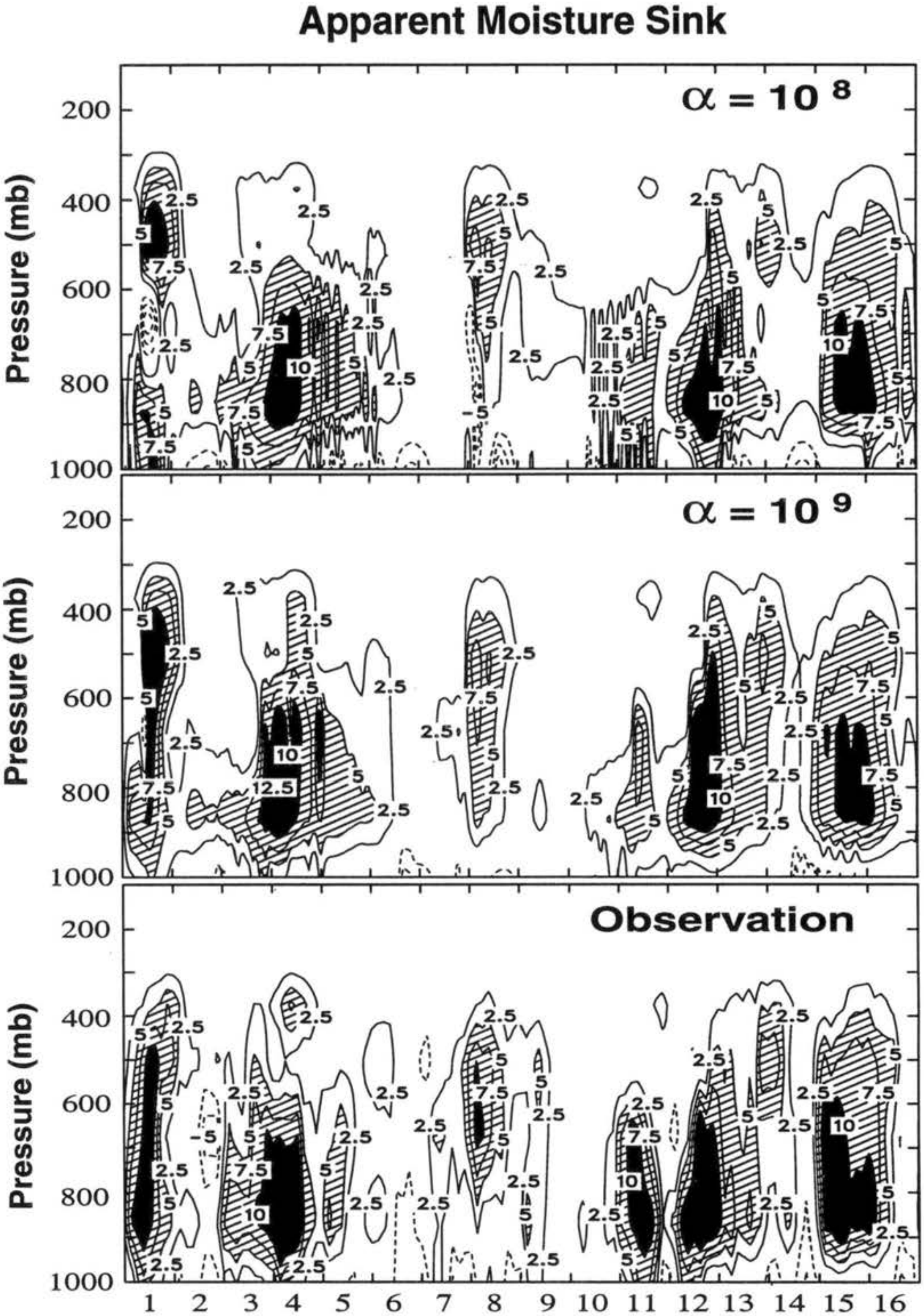

FIGURE 3.14: Same as Fig. 3.13, except for the apparent moisture sink (Q_2/C_p).

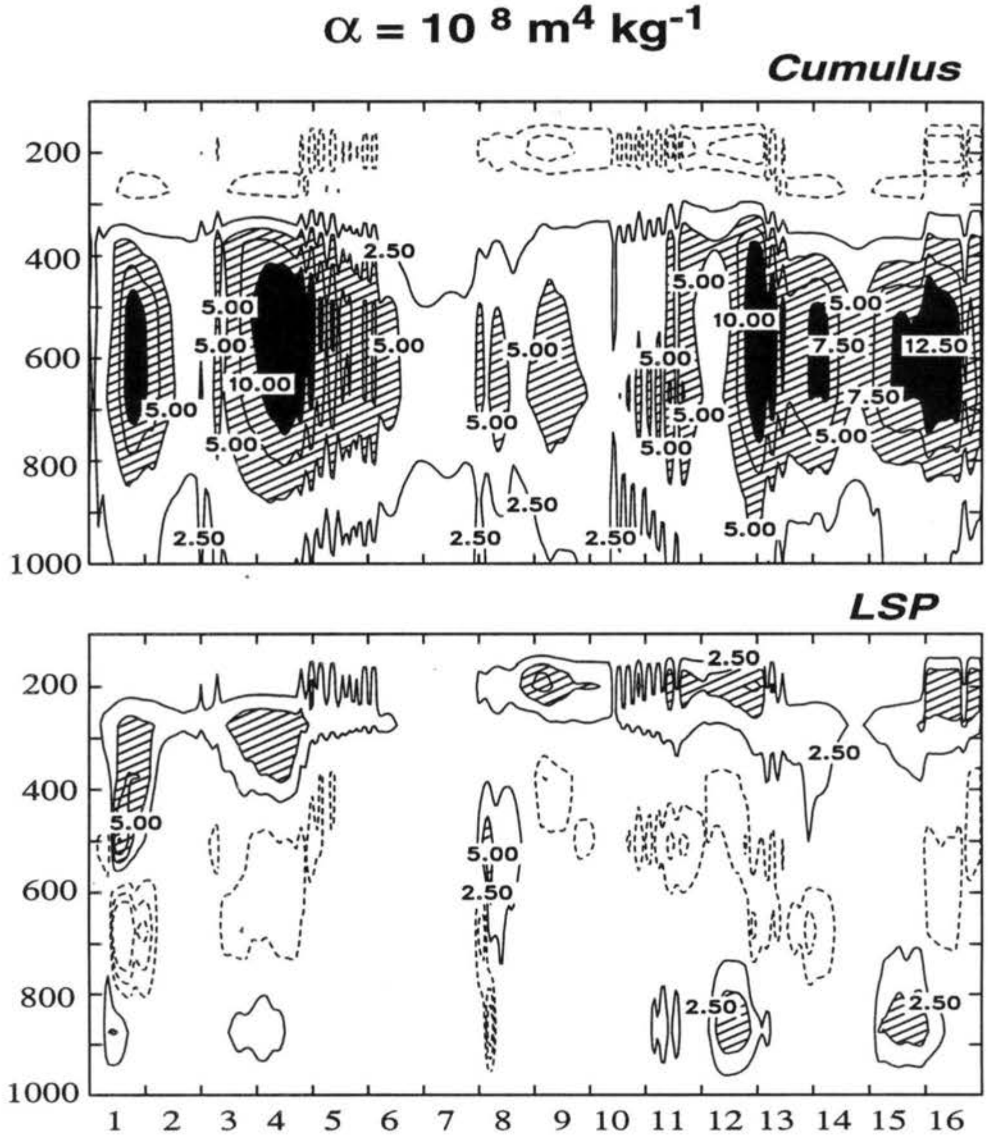

FIGURE 3.15: Components of the apparent heat source: the cumulus heating (above) and the LSP heating, for $\alpha = 10^8$ m^4 kg^{-1}. Contour interval and shading are the same as in Fig. 3.13.

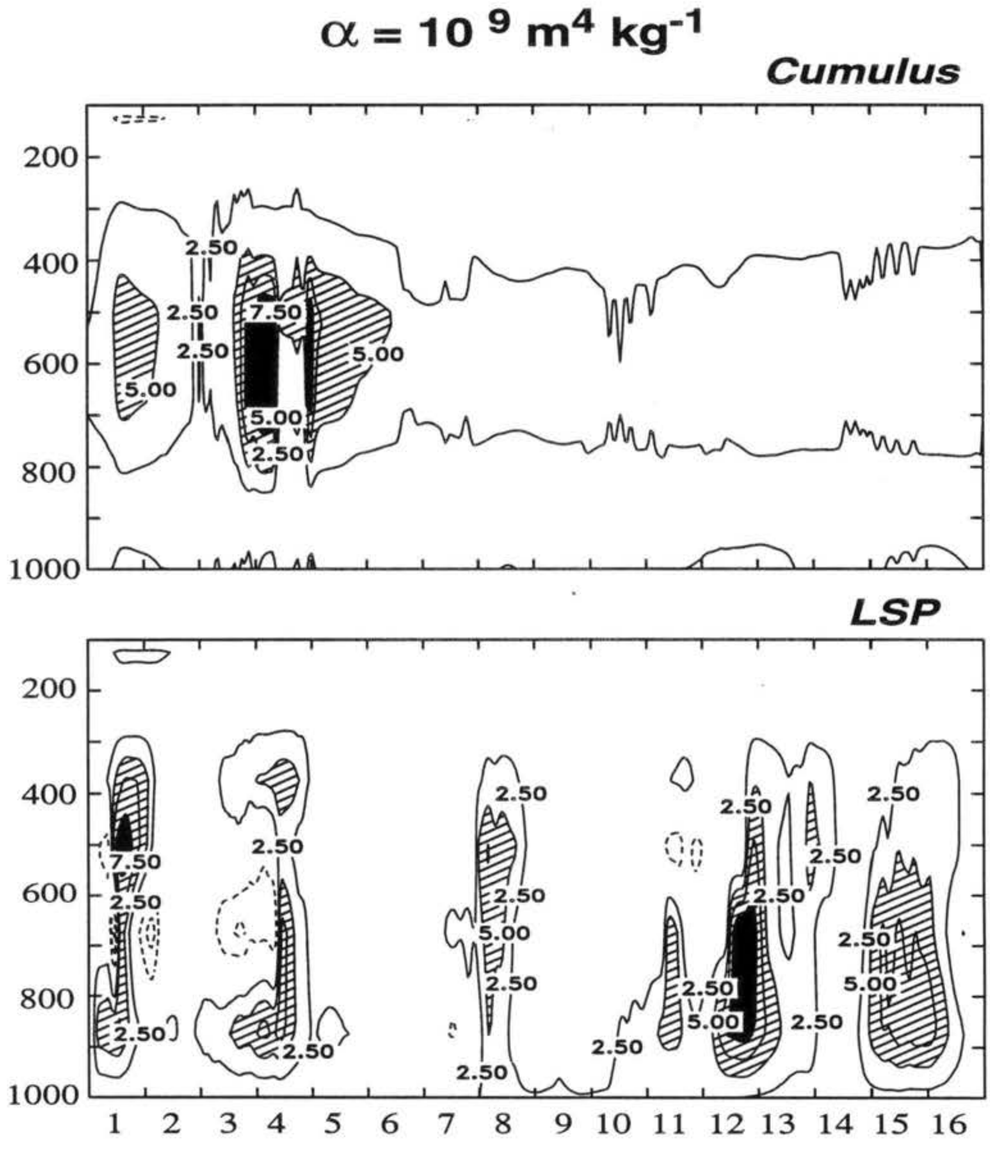

FIGURE 3.16: Same as Fig. 3.15, except for $\alpha = 10^9$ m^4 kg^{-1}.

tions with observations in auto-correlation. Fig. 3.11 shows the auto-correlation coefficient as a function of time. For $\alpha = 10^8$ m^4 kg^{-1}, the auto-correlation after 9 hours does not taper away as efficient as observations, while the correlation is lower than observed within the first 4 hours. Again, results with $\alpha = 10^9$ m^4 kg^{-1} is obviously closer to the observations than those with $\alpha = 10^8$ m^4 kg^{-1}.

Fig. 3.12 shows the auto-correlation of cumulus precipitation and LSP compared with that of the total precipitation. The LSP auto-correlation does not last as long as cumulus precipitation, even though it is a large-scale process. The parameterized LSP responds spontaneously to the cumulus convection in the model. In addition, the LSP can occur only when the large-scale environment is close enough to saturation in the convective layers so that the re-evaporation does not consume all the falling LSP midway to the surface. This further reduces the auto-correlation of LSP.

The auto-correlation of LSP goes to zero faster with $\alpha = 10^8$ m^4 kg^{-1} than with $\alpha = 10^9$ m^4 kg^{-1}. However, with $\alpha = 10^8$ m^4 kg^{-1}, the auto-correlation of the total precipitation is close to that of the cumulus precipitation because less than 10% of precipitation is from LSP, as mentioned above. Three curves of $\alpha = 10^9$ m^4 kg^{-1} are closer to one another, because of the large contribution of LSP to the total precipitation. The curve of cumulus auto-correlation starts to depart from the other two curves after 14 hours, while the total precipitation curve remains closer to the LSP. This implies that for variation in a time scale of 14 hours or longer, the precipitation mainly comes from LSP. The auto-correlation with cumulus precipitation at the right end is higher but the actual precipitation is small.

3.3.2.2 Q_1 and Q_2

Q_1 and Q_2 are the sums of the cumulus and LSP effects, surface fluxes, and radiation. Before breaking them down into their components, we first compare the simulated and the observed Q_1 and Q_2. Fig. 3.13 shows the time-pressure cross-section contours of Q_1 for $\alpha = 10^8$ m^4 kg^{-1}, 10^9 m^4 kg^{-1}, and observations. Fig. 3.14 shows the Q_2 counterparts. The positions of the heating and drying maxima are generally well reproduced by the model. The most obvious difference between the observation and the simulations is that the model seems not to produce cooling as strong as observed, especially above 300 mb.

The Q_1 and Q_2, in this experiment, are actually only the sum of the cumulus and the LSP effects, since MSTADJ is turned off and DCADJ is not active through the whole period of simulation. Fig. 3.15 shows the contributions to Q_1 from the cumulus and LSP heating, separately, for $\alpha = 10^8$ m^4 kg^{-1}. $\alpha = 10^9$ m^4 kg^{-1} is shown in Fig. 3.16.

With $\alpha = 10^8$ m^4 kg^{-1}, heating by cumulus convection dominates LSP. The LSP is most active above 400 mb and is usually directly associated with cumulus cooling caused by detrainment evaporation. On the other hand, the LSP cooling in the middle atmosphere is associated with cumulus heating there. Overall, the LSP heating has a similar structure as the cumulus heating except of opposite sign, and the former is a "response" of the latter. However, this is not as obvious with $\alpha = 10^9$ m^4 kg^{-1}, which shows almost no vertical structure of cumulus heating after the fifth day. Variation with time is also mostly reflected in LSP.

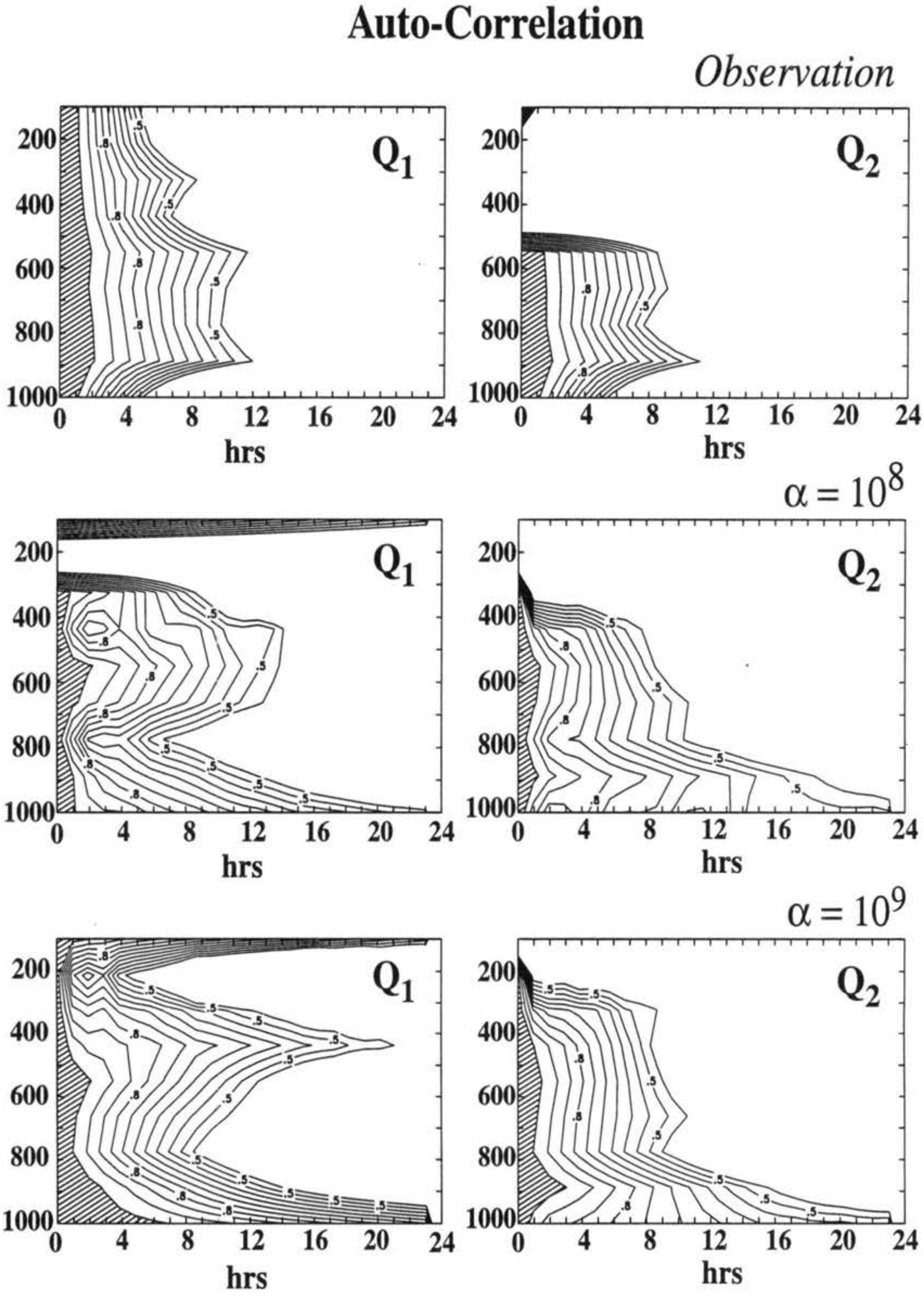

FIGURE 3.17: Auto-correlation of Q_1 and Q_2 as a function of pressure for $\alpha = 10^8$ m^4 kg^{-1} and $\alpha = 10^9$ m^4 kg^{-1}. Contour interval is 0.2, only contours larger than 0.4 are plotted. Shaded areas are larger than 0.95.

Fig. 3.17 compares the auto-correlation functions of Q_1 and Q_2 from the two simulations and the observed. The high and long-lasting auto-correlations at very high levels may not be very meaningful, because the correlation coefficients have been normalized by variance, which can be very small there. Both simulations also show high and long-lasting auto-correlation in the PBL which can also be explained by small variance there (e.g. surface evaporation as shown in Fig. 3.9). When the variance is zero, we let the auto-correlation be zero. $\alpha = 10^9$ m^4 kg^{-1} shows much better results above 300 mb than $\alpha = 10^8$ m^4 kg^{-1}.

To compare the results with observations more clearly in their vertical structures, we calculated time-averaged Q_1 and Q_2. We chose four of the major convective events during the period of simulation (as marked by letters A, B, C, and D in Fig. 3.10) by selecting the hours when the precipitation is over 13.5 mm day^{-1}. The results are shown in Fig. 3.18 and Fig. 3.19.

The vertical distributions of Q_1 and Q_2 during the periods of "severe" convection are generally well recovered. The results with $\alpha = 10^8$ m^4 kg^{-1} are closer to the observed than those with $\alpha = 10^9$ m^4 kg^{-1}, except for in event A at the low levels where LSP evaporation causes strong cooling and moistening. In events B and C, Q_1 with $\alpha = 10^9$ m^4 kg^{-1} is too small in the middle to low-level atmosphere. With $\alpha = 10^8$ m^4 kg^{-1}, it seems that we get better simulations for events B and D. Note that, according to Frank (1978), events A and C are cloud clusters and events B and D are squall lines; and that the major difference seen in the environment between these two types of severe convection is the vertical wind shear. Although we did not input the wind field in the simulation, it was au-

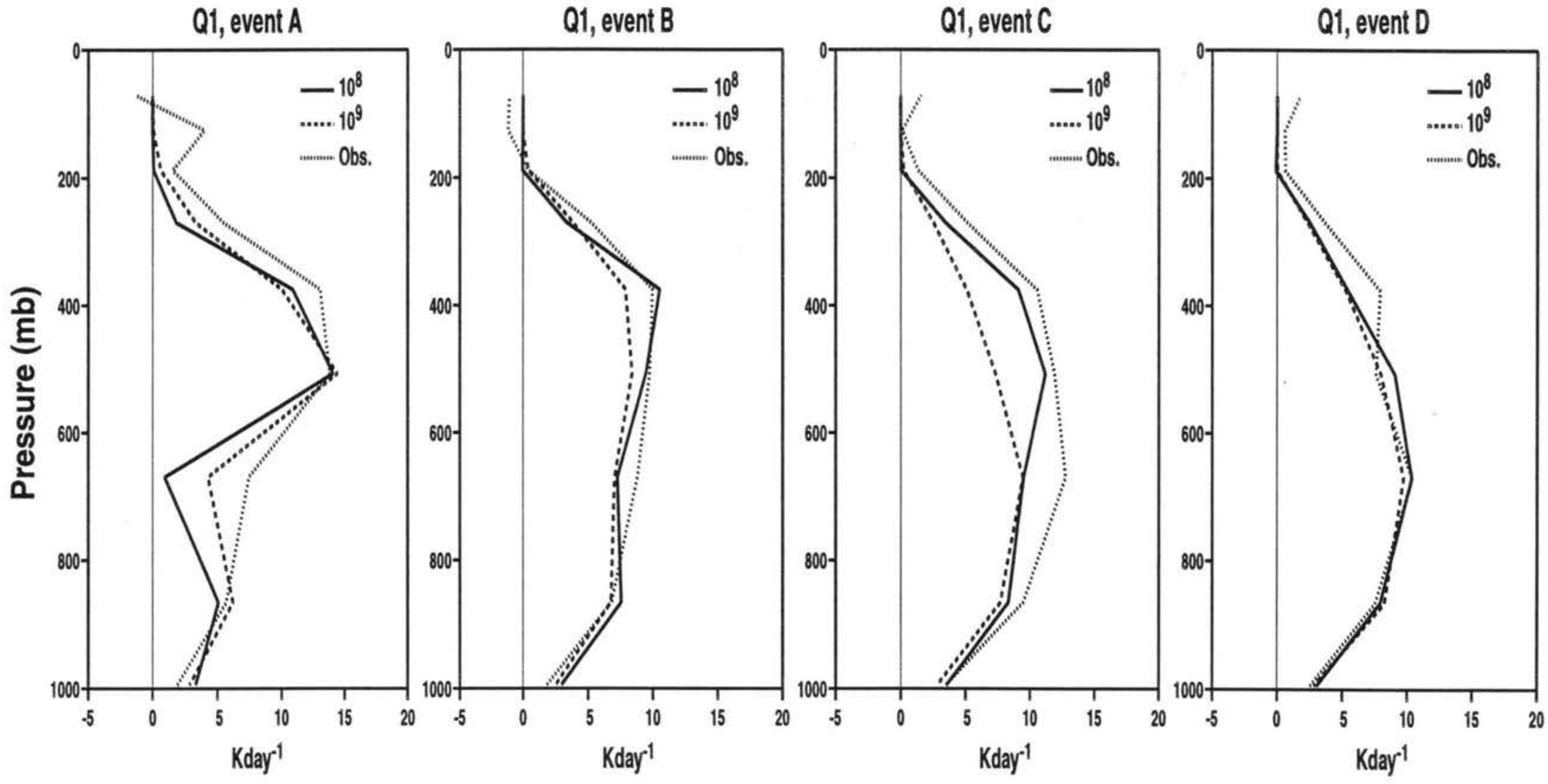

FIGURE 3.18: Time-averaged vertical distribution of Q_1 in the four major convective events.

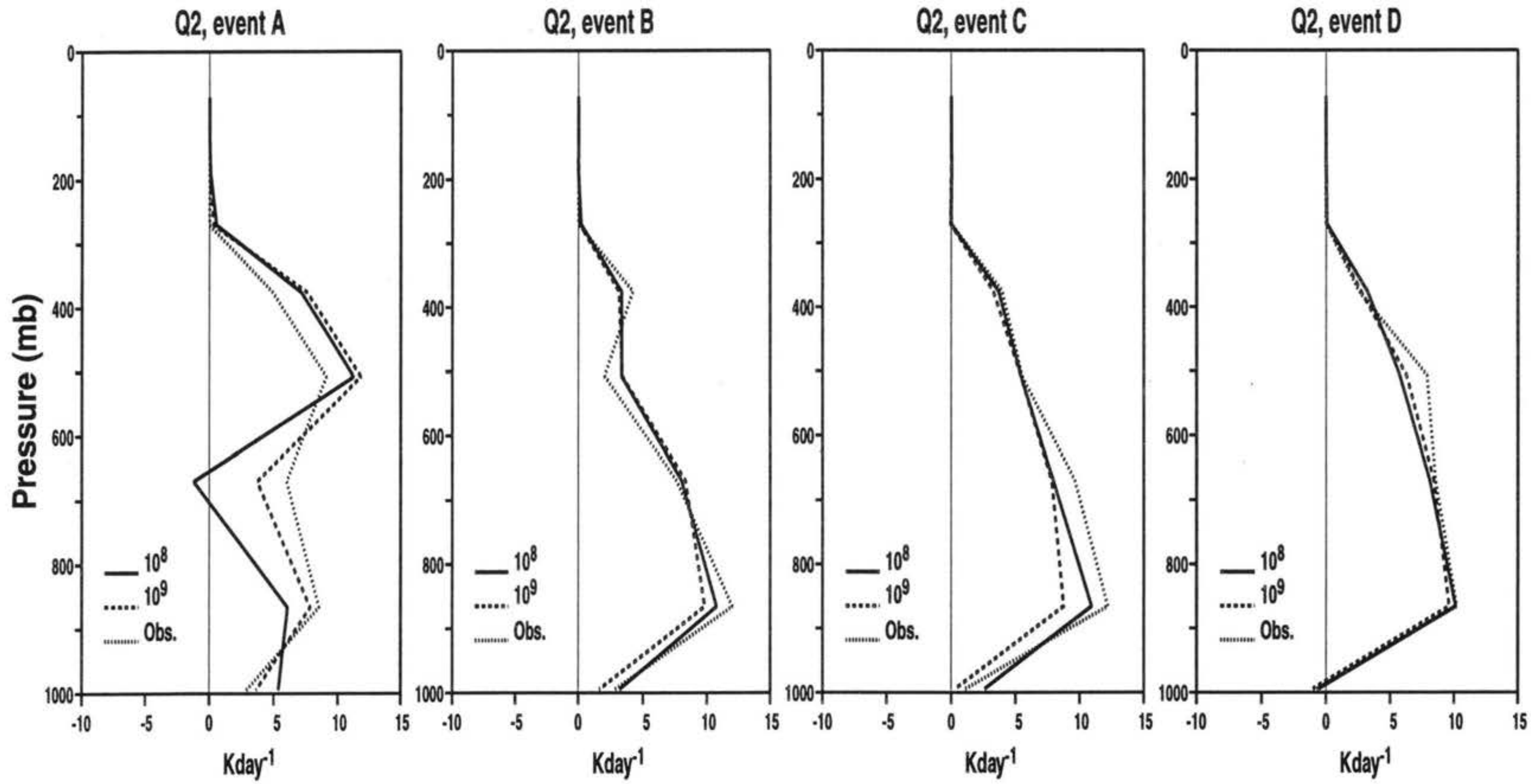

FIGURE 3.19: Time-averaged Q_2 during the four major convective events.

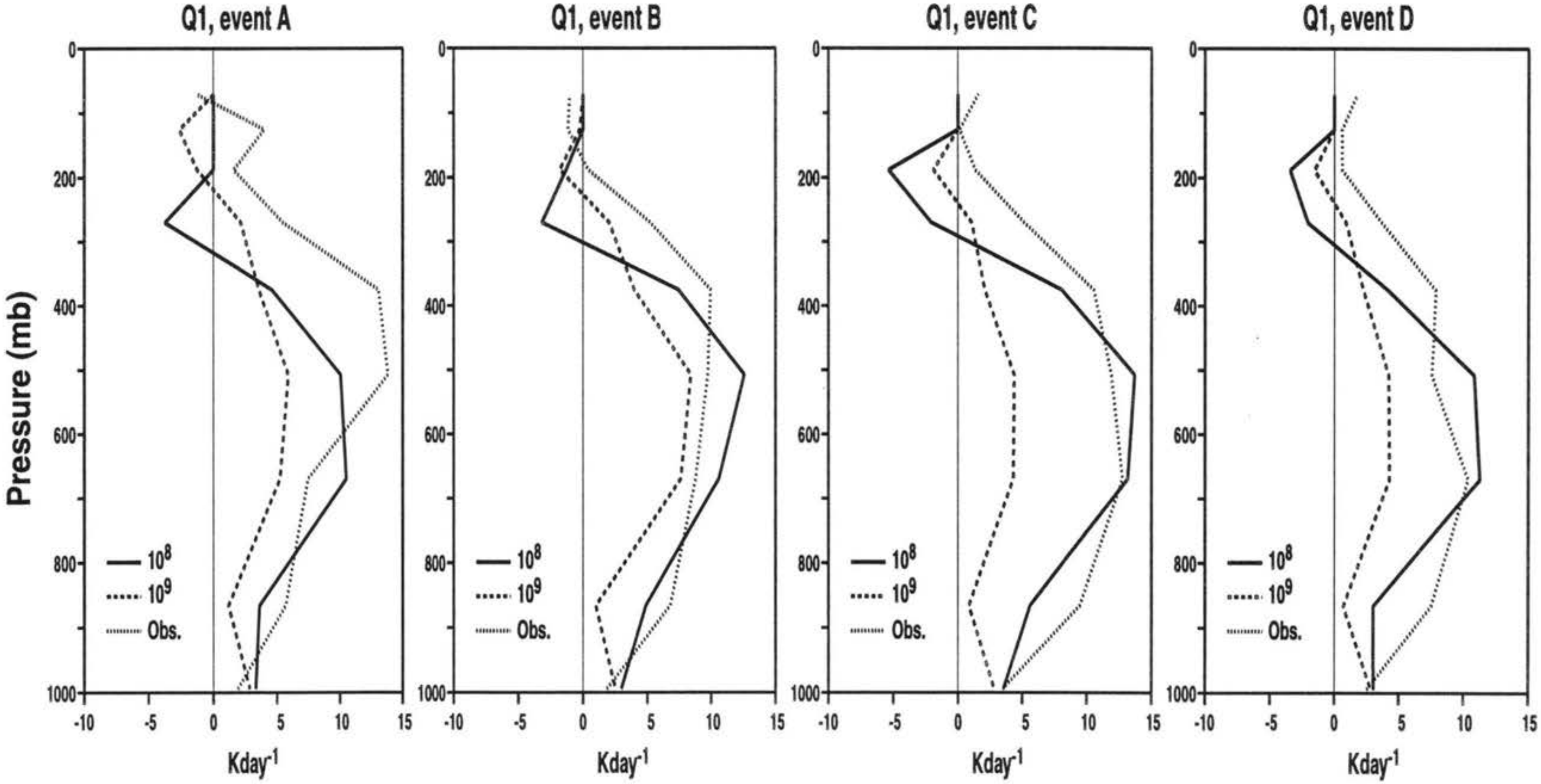

FIGURE 3.20: Same as Fig. 3.18, except that LSP heating is excluded.

tomatically included in the large-scale advection. As mentioned in Chapter 2, the parameter ε in the formula of α — Eq (2.14), implies effects of wind shear.

The apparent heating excluding LSP heating is shown in Fig. 3.20, which shows a major difference between the results with the two different α's. The LSP heating usually has opposite signs with the convective heating when $\alpha = 10^8\ m^4\ kg^{-1}$ while the LSP heating and cumulus heating are "cooperative" when $\alpha = 10^9\ m^4\ kg^{-1}$.

Note that it is not easy to compare our simulations with the semi-prognostic tests of e.g. Lord (1982). The "predicted Q_1" in Lord (1982) includes only convective effects, while our Q_1 also includes the LSP effects. The excessive warming and drying at low levels due to the neglect of downdraft effects cannot be seen in our prognostic simulations.

3.3.2.3 Soundings

The simulated temperature, mixing ratio, and relative humidity are compared with the observations in Fig. 3.21. Fig. 3.22 shows the time average through the period of simulation. The simulation shows lower temperature throughout the troposphere, compared to the GATE observations. Water vapor mixing ratio is increased above 500 mb but decreased below. Results also show that the simulated mixing ratio and temperature have stronger variations with time than the observed.

The relative humidity (only the saturation mixing ratio with respect to water considered) of the simulated atmosphere is saturated above 400 mb almost all the time. This high relative humidity can also extend down to 900 mb, quite often during the peak-

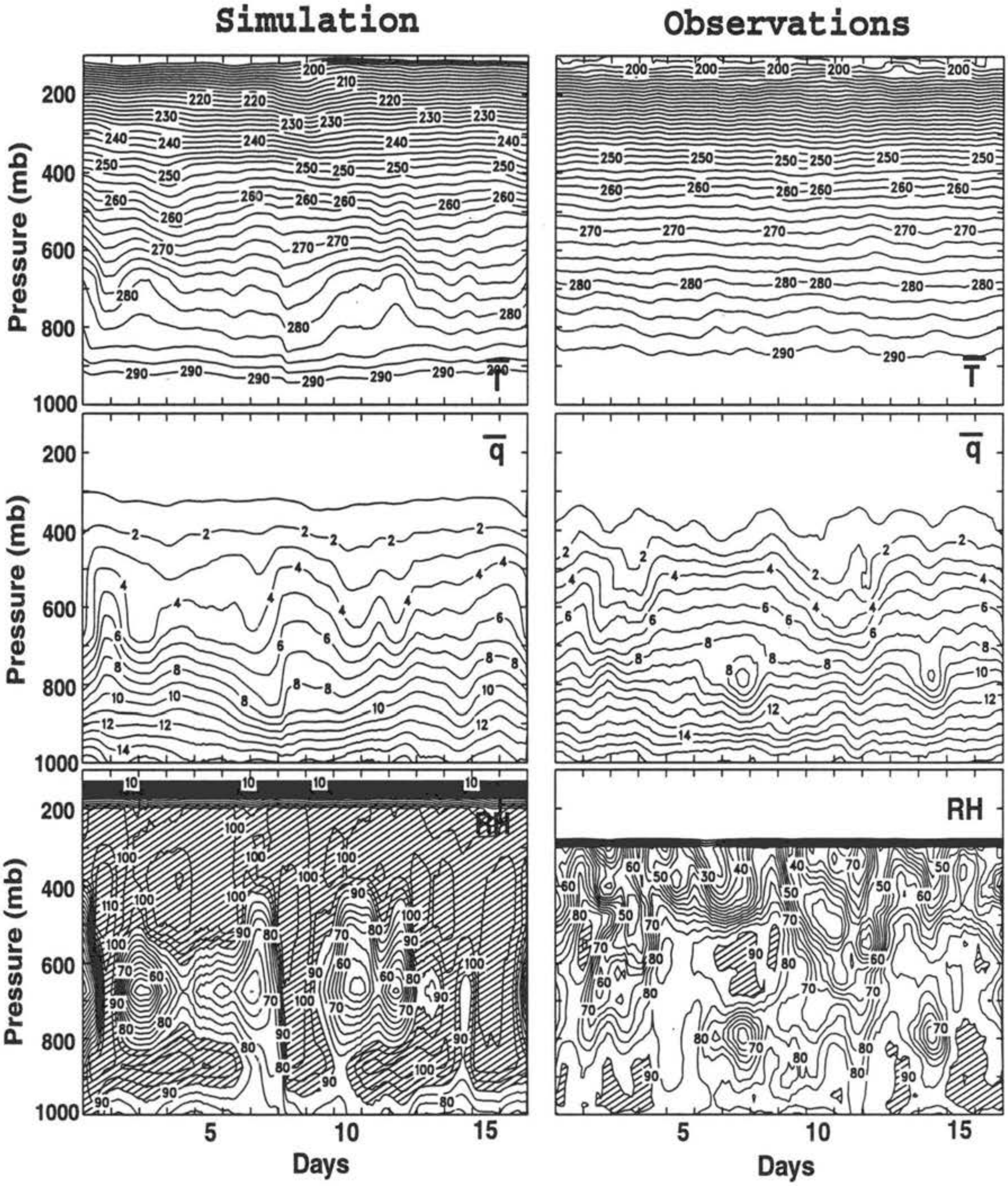

FIGURE 3.21: Time-pressure cross section for temperature, mixing ratio, and relative humidity of the model simulation and the observations. Contour intervals are 2.5 K for temperature, 1 g kg^{-1} for mixing ratio, and 5% for relative humidity. Relative humidity above 90% is shaded.

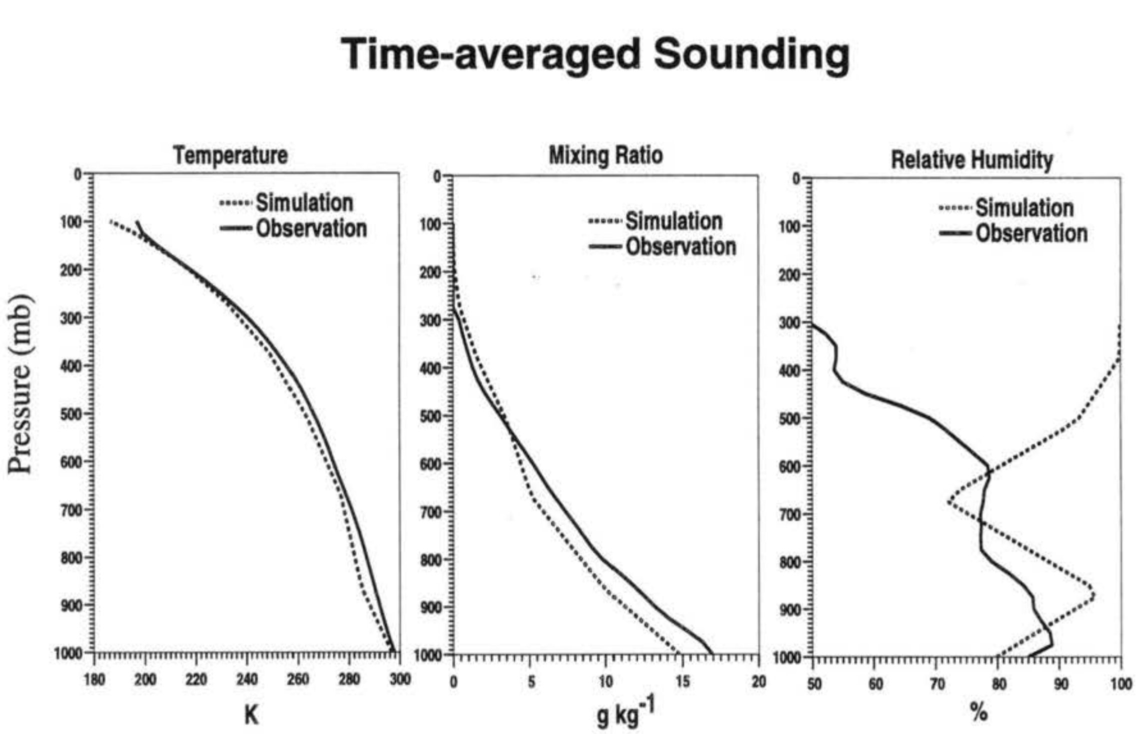

FIGURE 3.22: Time-averaged vertical distribution of temperature, mixing ratio, and relative humidity of the GATE simulation compared with the observations. Relative humidity above 300 mb is omitted.

hours of cumulus convection. The high relative humidity is partly due to the LSP process which is not triggered until (gridbox-averaged) supersaturation occurs. In reality, anvil clouds can rain even if they do not occupy a whole grid box. Meanwhile, in the 1-D simulation, we do not have interactive large-scale dynamics. Therefore, there is no mechanism, other than the cumulus-induced subsidence, that can reduce the relative humidity to sub-saturation. Because of the LSP, the high relative humidity, in turn, changes the sensitivity of cumulus convection to large-scale processes.

3.4 Summary and Discussion

We tested the prognostic CKE method in a 1-D model. We used a constant external forcing — a 2 K day^{-1} radiative cooling, to examine the parameterized cumulus convection. $\alpha = 10^8\ m^4\ kg^{-1}$ was chosen in the first place. The simulated cumulus convection modifies the environment by subsidence warming below and detrainment cooling above. The evaporation of the detrained condensates often causes supersaturation and triggers the LSP. The vertical distribution of the cumulus heating is determined by the LSP for the balance of energy and that the radiative cooling has no vertical structure. This means that the LSP is a "forcing" for the cumulus convection, and that how LSP is parameterized has a direct effect on the results.

We tested the model using different values of the parameter α, with a fixed $\tau_D = 600$ sec. We found that the steady-state solutions vary quite significantly with α, e.g. a change of α from $10^8\ m^4\ kg^{-1}$ to $10^9\ m^4\ kg^{-1}$ causes a 20% decrease in precipitation. The steady-state environment is much colder and has a much drier PBL. It contains more active cloud types, including some shallower clouds, but less total mass flux is transferred vertically. Different α's, however, all have saturated steady-state upper-level atmosphere. A simple test showed that the "one-α" approach performs reasonably well.

The 1-D model was used to simulate GATE observations. Different from the constant radiative cooling, the large-scale "forcing" in this case is time-dependent and has vertical structures. This results showed that the prognostic CKE can well capture the time evolution of precipitation. The atmosphere is saturated too often especially at high levels, because the LSP in the model cannot bring the atmosphere to sub-saturation.

We tested with two different values of α in the GATE simulation. Generally speaking, $\alpha = 10^8$ m^4 kg^{-1} gives better vertical distribution of Q_1 and Q_2, while $\alpha = 10^9$ m^4 kg^{-1} produces the time behavior that is closer to the observed. $\alpha = 10^9$ m^4 kg^{-1} also gives more realistic partition between the cumulus precipitation and LSP. These may suggest the use of different α's for different cloud types.

The use of the CKE approach substantiates the problem with the LSP parameterization in the model, which cannot be seen in a semi-prognostic tests of the quasi-equilibrium approach. Because of the LSP, the high relative humidity, in turn, changes the sensitivity of cumulus convection to large-scale processes. Results show that the simulated mixing ratio and temperature have stronger variation with time than the observed.

The comparison between the simulated Q_1 and Q_2, and the observed Q_1 and Q_2 does not show the excessive warming and drying at low-levels as those seen in Lord (1982). The low-level excessive warming and drying have been attributed to the neglect of downdrafts (Johnson, 1976; Cheng, 1989). Apparently, our interactive PBL processes have "compensated" the differences caused by the neglect of downdrafts. When the excessive warming and drying occur at the low-level atmosphere, the "signal" is transferred into the PBL through the PBL-top entrainment. The excessive warming and drying of the PBL turn on the surface evaporation and sensible heat flux.

In Lord (1982)'s semi-prognostic test, he compared the time-average Q_1 and Q_2 profiles with the observations. He calculated the cloud-base mass flux using the observed temperature and mixing ratio soundings and large-scale advection and radiation. He assumed that a part of the suspended liquid water turns into precipitation. A conversion constant $2 \times 10^{-3}\ \mathrm{m}^{-1}$, same as in our model, was used. The condensates that do not drop as precipitation finally detrain in the cloud-top layers. The detrained condensates were assumed to evaporate and cause cooling and moistening in the detrainment layer. The precipitation obtained this way is only a part of the total precipitation in our model, in which large-scale precipitation is also grossly represented by the LSP parameterization. On the other hand, Lord (1982) used only cumulus precipitation to compare with the observed total precipitation.

The time integration of the semi-prognostic tests does not conserve energy or water substances, but our prognostic tests do. The water vapor that comes into the system (e.g. by large-scale advection or surface evaporation) either stays in the atmosphere or rains out. In a time average over the period of simulation, the water that comes into the system should equal what goes out. In the semi-prognostic tests, observed soundings [*T(z)* and *q(z)*] are used every time step. The soundings after the cumulus feedback are not used for the next time-step. This means that the non-quasi-equilibrium part of the cloud work function does not have any effect afterwards, in the semi-prognostic tests.

In the semi-prognostic test, both the observed sounding and the large-scale forcing are used to calculate the cumulus mass flux. The environmental sounding was used to calculate the kernels, the cloud work function and its change due to the large-scale processes (i.e., the large-scale forcing). In other words, the "large-scale forcing" forces the subgrid-scale cumulus convection. The large-scale forcing is defined as the rate of increase of the cloud work function due to the large-scale processes. Therefore, the large-scale forcing depends not only on the large-scale processes that tend to increase the cloud work function, but also on the environmental sounding that the large-scale processes are imposed on (e.g., the same cold front passing over surfaces of temperatures 290K and 300K results in different large-scale forcings.) Since both the kernels and the large-scale forcing depend on the sounding, the prediction after the first timestep will carry the error from the first-timestep prediction, and so forth. Semi-prognostic tests avoid the accumulation of error with time and demonstrate the adequacy of cloud work function quasi-equilibrium but do not explain the cause of the non-quasi-equilibrium part of the results. Take precipitation as an example. Observations show that stratiform clouds account for a large part of the GATE precipitation. Vertical profiles of Q_1 and Q_2 of stratiform clouds are almost identical (Johnson and Young, 1983), while the peak of Q_2 usually are lower than that of Q_1 for cumulus convection. However, the semi-prognostic tests cannot distinguish cumulus precipitation from large-scale precipitation. They produce the necessary amount of precipitation solely by heating the environment in the cumulus way.

In our approach, the CKE is predicted continuously in time. We do not explicitly calculate the kernel or the large-scale forcing. The cloud work function is calculated from the predicted sounding. Only the observed large-scale advection and radiation was inputted as an external forcing. Also the LSP is a part of the "forcing".

For a non-linear system, a small difference in the initial condition will cause dramatic differences after a period of time. What makes us expect that we can get a comparable time series as the observation, given only the initial sounding and the hourly large-scale forcing? If we can still catch the time evolution of e.g. the precipitation rate, it means that the quasi-equilibrium assumption holds quite well for this approach, and that the cumulus activity mainly follows the time evolution of the large-scale forcing. However, the time series of the environmental sounding is not expected to be identical. How can we explain the difference of the simulation from the observation? From the semi-prognostic tests, we cannot see how the cumulus convection interacts with other physics, such as LSP. After all, the purpose of the semi-prognostic tests is to investigate the cumulus parameterization scheme. With our method, the interaction between the cumulus and LSP automatically occurs in the model.

CHAPTER 4

Three- Dimensional Tests Using the CSU GCM

In the 1-D experiments discussed in the preceding chapter, interactive radiation was not used. The cumulus clouds could not change the radiative heating rate in these experiments. However, as we have discussed, cumulus convection is closely related to the existence of radiatively important stratiform clouds. The interaction between radiation and cumulus convection is an important factor in determining the atmospheric general circulation.

The general circulation determines the "large-scale forcing" for the cumulus convection, while the cumulus convection modifies the environment and the general circulation. The response of the simulated general circulation to changes in the cumulus parameterization may help us understand more about the interactions between cumulus convection and the large-scale dynamics.

We applied the prognostic CKE approach in the Colorado State University (CSU) GCM. The results were compared with those using the cloud work function quasi-equilibrium (the control run). We found that both results (especially the CKE approach) show stronger tropical planetary albedo than observed. A different way to represent the radiative effects of the anvil clouds was therefore tested, in which we allowed the anvil areal coverage of a grid-box to be fractional. For convenience, we call this method the "fractional" anvil and the original method the "binary" anvil (where anvils cover the whole grid-box if they exist at all). The fractional anvils were first tested with the CKE approach and this change produced significant changes in the simulated general circulation. Later the fractional anvil approach was applied with the cloud work function quasi-equilibrium; in this case the change from the binary anvil to the fractional anvil can be considered as a change in the "large-scale forcing."

We give a brief description on the CSU GCM in Section 4.1. In Section 4.2, we compare the results of the four experiments and discuss the impact of the prognostic CKE and the fractional anvils on the simulated general circulation. Section 4.3 shows the comparison between our model results with the observations. Section 4.4 gives a summary and discussion.

4.1 Model Description and Experiment Design

4.1.1 The Colorado State University GCM

The CSU GCM originates from the UCLA GCM. The most important changes made up to now are revised solar and terrestrial radiation parameterizations (Harshvardhan *et al.*, 1987). The prognostic variables of the GCM are: potential temperature, the water vapor mixing ratio, the horizontal velocities, the surface pressure, the depth of the PBL, and turbulence kinetic energy, the ground temperature and snow depth at land points, and the ice temperature at land ice and sea ice points. The governing equations are finite-differenced, using highly conservative schemes (Arakawa and Lamb, 1977, 1981). Fourier filtering of the mass flux and pressure gradient vectors is used to maintain computational stability near the poles (Arakawa and Lamb, 1977).

The radiation parameterization of the model is that of Harshvardhan *et al.* (1987). The terrestrial radiation includes cooling due to water vapor, carbon dioxide, and ozone. The solar radiation parameterization includes Rayleigh scattering and absorption by water vapor and ozone. It simulates both the diurnal and seasonal cycles. A complete (solar and terrestrial) radiation calculation is done once per simulated hour, in order to resolve adequately the diurnal cycle and the effects of transient cloudiness. A zonally uniform ozone distribution is prescribed as a function of latitude and height.

Cloudiness can occur in any GCM layer, and can be associated with large scale saturation, PBL stratocumulus clouds, or the anvils of deep cumuli. For simplicity, when and where the large-scale saturation cloudiness occurs, it has been assumed to fill an entire grid box; no parameterization of subgrid fractional cloudiness has been attempted up to now. One is introduced in this study, for reasons to be explained later.

The shortwave optical depth for the cirrus clouds is

$$\tau_{sw} = \begin{cases} a(T_c - T_0)^2 \Delta p_c, & T_0 \le T_c \le -10^\circ C \\ b\Delta p_c, & T_c \ge 0^\circ C \end{cases} . \tag{4.1}$$

Anvil clouds are assumed to occur whenever convection penetrates above the 500-mb level. The optical depth of the anvil clouds depends only on the physical depth of the convection above this level:

$$\tau_{sw} = 0.16 \, (p_T - 500) \, , \tag{4.2}$$

where p_T is the pressure (in mb) at the top of the highest cumulus clouds.

The longwave optical depth is assumed proportional to τ_{sw} with a constant, and the longwave emittance of the anvil clouds is given by

$$\varepsilon_0 = 1 - exp \, (-b \Delta p_c) \, , \tag{4.3}$$

where $\Delta p_c = p_T - 500$ (mb) is the pressure thickness of the anvil, and the constant $b = 0.12$ is given by Harshvardhan *et al* (1989).

Stratocumulus clouds are assumed to be present in the PBL whenever the temperature and mixing ratio at the PBL top (as determined by a mixed-layer assumption) correspond to supersaturation, provided that cloud-top entrainment stability does not occur. The presence of the stratocumulus clouds is felt through both the radiation and entrainment parameterizations. The latter takes into account the generation of turbulence kinetic energy through increased buoyancy fluxes associated with phases changes and highly concentrated cloud-top radiative cooling (Randall, 1980, 1984). As a result of these cloud-enhanced buoyancy fluxes, the presence of a stratocumulus layer in the PBL tends to favor more rapid entrainment and, therefore, a deeper PBL. A very simple parameterization of cloud-top entrainment stability is also included in the model.

The prescribed boundary conditions of the GCM include realistic topography, and the observed climatological seasonally varying global distributions of sea-surface temperature and sea-ice thickness. The surface albedo of the ocean is zenith-angle dependent. We also prescribe the soil characteristics and the seasonally varying morphological and physiological parameters for the land-surface vegetation.

4.1.2 Experiment design

Simulations were made with a grid spacing of 4^o of latitude by 5^o of longitude, with 17 layers. The control run used the original A-S parameterization with the cloud work function quasi-equilibrium (as developed by Lord *et al*, 1980) and binary anvils (also referred to as the BQ run). The second run used the prognostic CKE with binary anvils (hereafter BK), in which we chose $\alpha = 10^8$ m^4 kg^{-1} and $\tau_D = 600$ s. The third run used fractional anvils (to be introduced later) and the prognostic CKE (hereafter FK). The fourth run used fractional anvils with the cloud work function quasi-equilibrium (hereafter FQ). The four runs are summarized in Table 4.1. All four runs start at December 1 and end at January 31. The first month is ignored as the model spin-up, and the second-month data are used for calculation of January means.

	Quasi-equilibrium of cloud work function	Prognostic CKE
Fractional anvil	FQ	FK
Binary anvil	BQ	BK

TABLE 4.1: Four simulations.

4.2 Results

Since all of the runs are for January conditions, the discussions in the following subsections will be focused only on January means. We shall investigate the diabatic heating and the mean fields from the four runs. We first compare BK with BQ, and examine the differences the prognostic CKE makes when the anvils are binary. We then introduce the fractional anvils in FK. From the comparison of FK and BK, we can see the effects of the fractional anvils. Finally, we compare the effects of the change from the binary anvil to the fractional anvil in the quasi-equilibrium approach and in the prognostic CKE approach.

4.2.1 BK vs. BQ: Effects of the Prognostic CKE in a Binary

Anvil Environment

4.2.1.1 Precipitation

The prognostic CKE method produces a global-mean January precipitation rate of 3.32 mm day^{-1}, which is a 7.3% decrease from that of the control run (3.58 mm day^{-1}). The observed global-mean precipitation rate is 3.63 mm day^{-1}. Fig. 4.1 compares the January total precipitation rate from the control run, the BK run, and the observations of Legates and Willmott (1990). The pattern is similar for the two runs. Both have ITCZ (intertropical convergence zone) precipitation maxima and precipitation minima in the subtropics where high-pressure systems prevail, as also seen in the observations. Other precipitation maxima are off the east coasts of continents Asia and North America (in the middle latitudes), where the storm tracks are located.

The difference between the two runs is also shown in Fig. 4.1. The prognostic CKE generates much stronger precipitation than the control run in the area of tropical western Pacific. Weaker precipitation is seen elsewhere in the tropics. Maximal increases of precipitation are also found in some mid- latitude locations.

The zonal-mean precipitation, from BQ to BK, decreases in the tropics but increases in the mid-latitudes. The zonal mean January precipitation rates from the two simulations and the observations are shown in Fig. 4.2, which also shows the differences between the two runs. The ITCZ peaks for both runs occur between the Equator and 10^{o}S. The prognostic CKE reduces the precipitation everywhere between 30^{o}N and 30^{o}S. It can be seen from Fig. 4.2 that cumulus precipitation decreases at almost all latitudes while the LSP

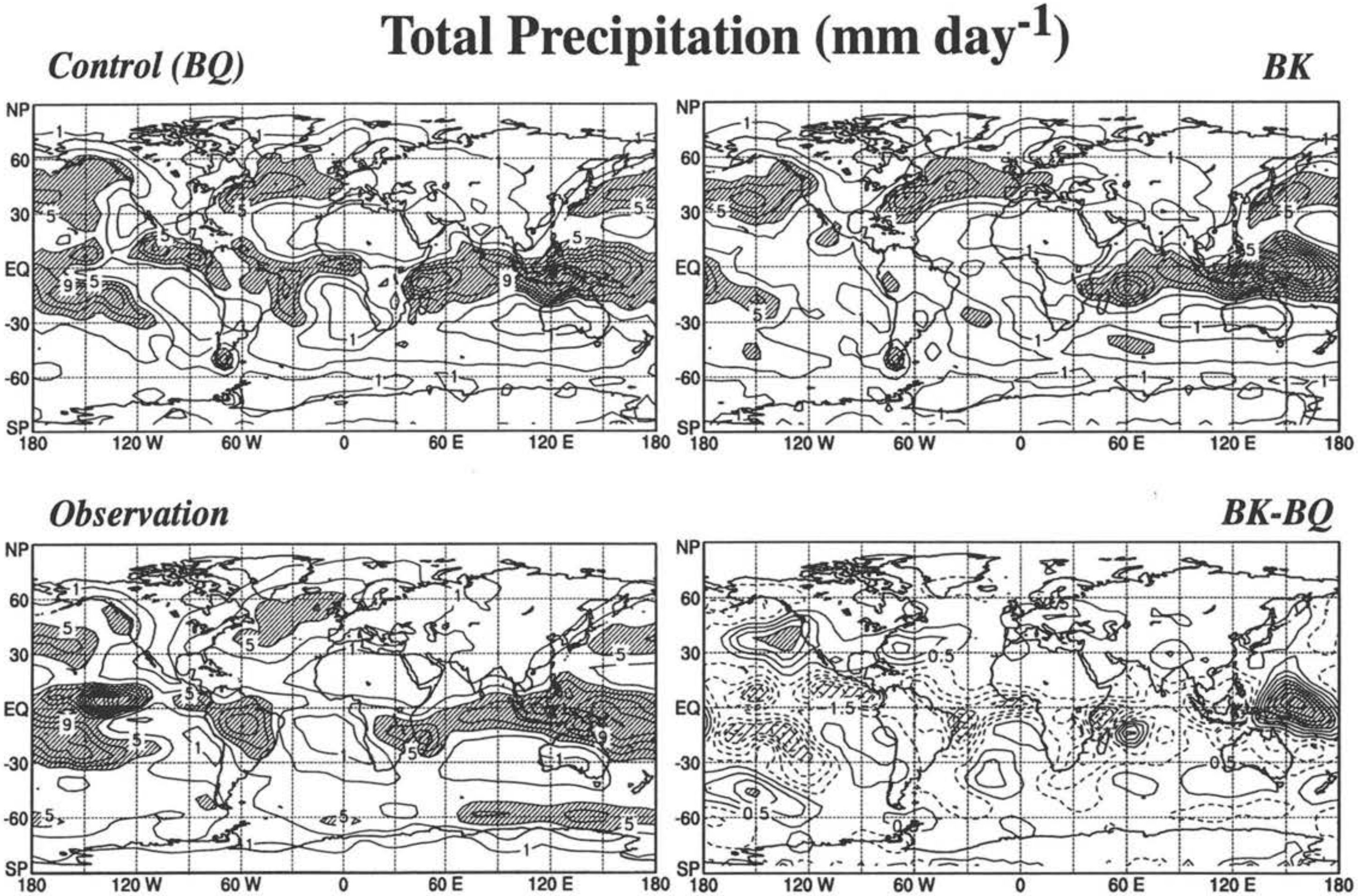

FIGURE 4.1: January monthly-mean total precipitation rate. Displayed are the results of the control run (top left), the BK run (top right), the observations, and the difference between the two runs (BK-BQ). The contour interval is 2 mm day^{-1}. Areas with precipitation rate larger than 5 mm day^{-1} are shaded. For the difference plot, contour interval is 1 mm day^{-1} and shaded areas are above 3.5 mm day^{-1} or below -3.5 mm day^{-1}.

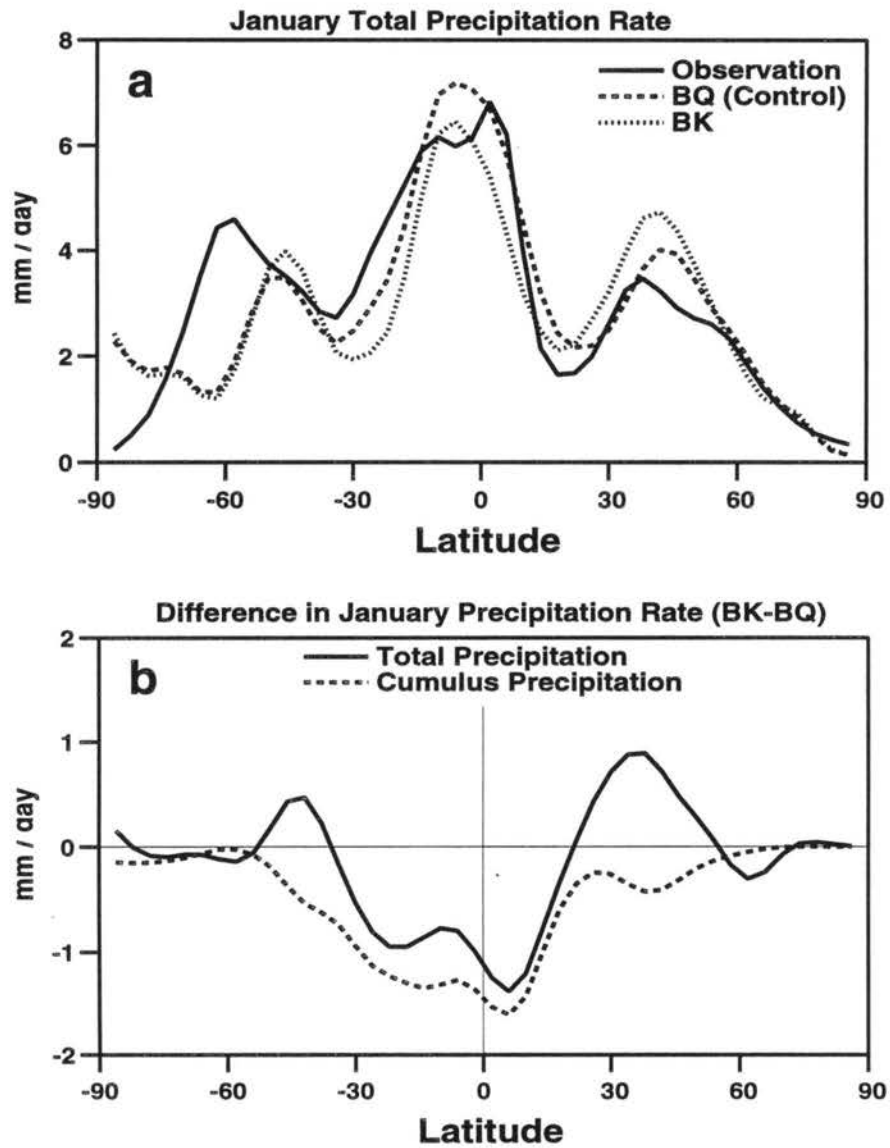

FIGURE 4.2: Zonal mean of the January monthly-mean precipitation rate (a) and its difference between BK and BQ. Three curves in (a) are observations (solid) and results from the BQ run (dashed) and the BK run.

mostly increases, especially in the middle latitudes. The global mean cumulus precipitation is reduced by 34% (from 2.08 mm day^{-1} to 1.38 mm day^{-1}), while the LSP increases from 1.51 to 1.94 mm day^{-1} (a 28% increase).

4.2.1.2 Cumulus and Anvil Incidences and Radiation Budgets

The cumulus (anvil) incidence is defined as the fraction of all time-steps (in a month) for which one or more types of cumulus clouds exist (penetrate 500 mb), in a grid box. The anvil incidence is the only factor in the model, other than the pressure depth of the anvil, through which the cumulus convection can directly change the monthly-mean radiation field.

Both cumulus and anvil clouds occur much more frequently in the BK run than in the control run, as shown in Fig. 4.3. As a global mean in the control run, cumulus convection occurs 11% of the time, while the anvil clouds occur 8% of the time. In the BK run, it is 30% for the cumulus and 21% for the anvils. The reasons for the large differences in the cumulus and anvil incidences are to be discussed later.

The substantially larger anvil incidence in the BK run changes the Earth radiation budget. Fig. 4.4 shows the January zonal-mean absorbed solar radiation at the top of the atmosphere from the two runs and observations. The observations are taken from the 1987 data of the Earth Radiation Budget Experiment (ERBE). The major difference between the two model results occurs in the area between 40^{o}S and 20^{o}N. The prognostic CKE reduces the absorbed solar radiation throughout the tropics and by up to 78 W m^{-2} close to the Equator. This indicates that the simulated anvil clouds are optically too thick,

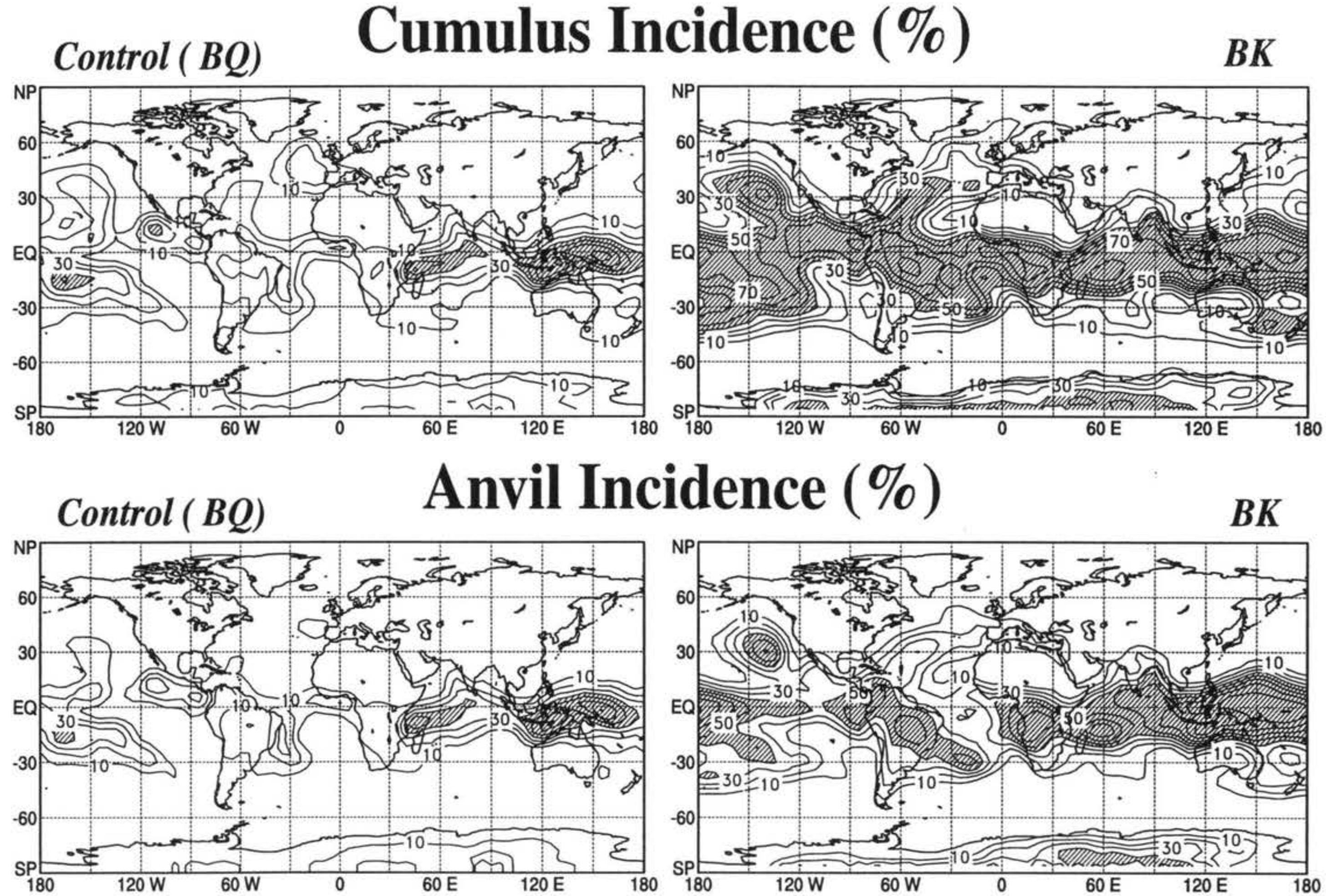

FIGURE 4.3: Monthly mean cumulus (above) and anvil incidences from the control run (left panel) and the BK run. The contour interval is 10%. Shaded areas are where incidence is larger than 40%.

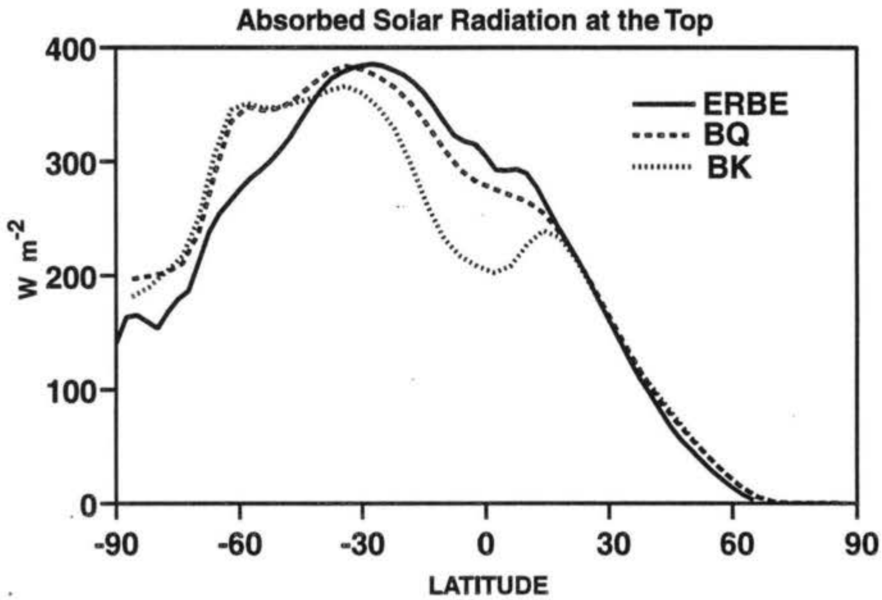

FIGURE 4.4: January zonal mean of the absorbed solar radiation at the top of the atmosphere. The three curves shown are from the BK run (dotted), the control (BQ) run (dashed), and the ERBE observations.

especially when we use the prognostic CKE. The large albedo in the BK run is associated with a high anvil incidence. However, the large albedo in the control run cannot be explained by the anvil incidence which is lower than observed as seen in Fig. 4.5, which shows the January-mean frequency of high cloudiness from 1990 ISCCP (International Satellite Cloud Climatology Project) data. The maximal frequency (up to 60%) along the region of the ITCZ in the figure should mostly be associated with deep convection. The global-mean anvil incidence in the control run is about 8%, which is much smaller than the global mean in Fig. 4.5 (14%). It should also be kept in mind that the area of a horizontal grid box in the ISCCP observation (2.5^{o} X 2.5^{o}) is about 1/4 of the grid area of the

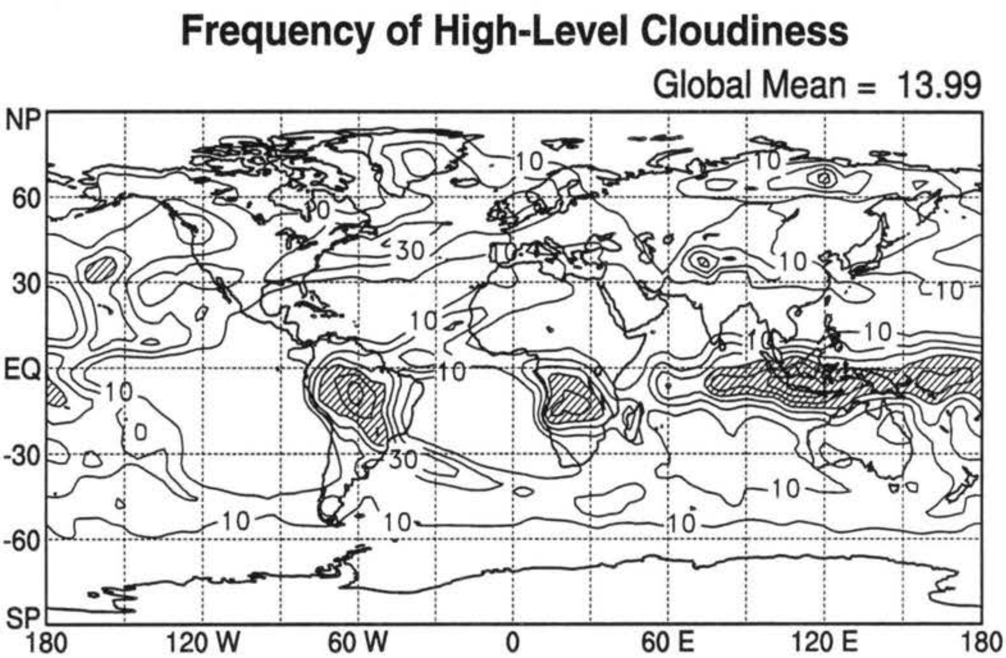

FIGURE 4.5: January mean frequency of high-level cloudiness from 1990 ISSCP data. Contour interval is 10% and above 40% is shaded.

GCM. For that reason, the observed frequency of cloudiness can be much larger when "mapped" onto the GCM grid. Since both runs show stronger planetary albedo in the tropical area than the ERBE observation, it appears that a better method is needed to represent the radiative effects of the anvil clouds.

4.2.1.3 Cumulus Convection

Cumulus convection and large-scale condensation are the major mechanisms in the model to balance the radiative cooling. The LSP associated with convective detrainment, however, can be considered as just an "extension" of the cumulus convection, since it re-

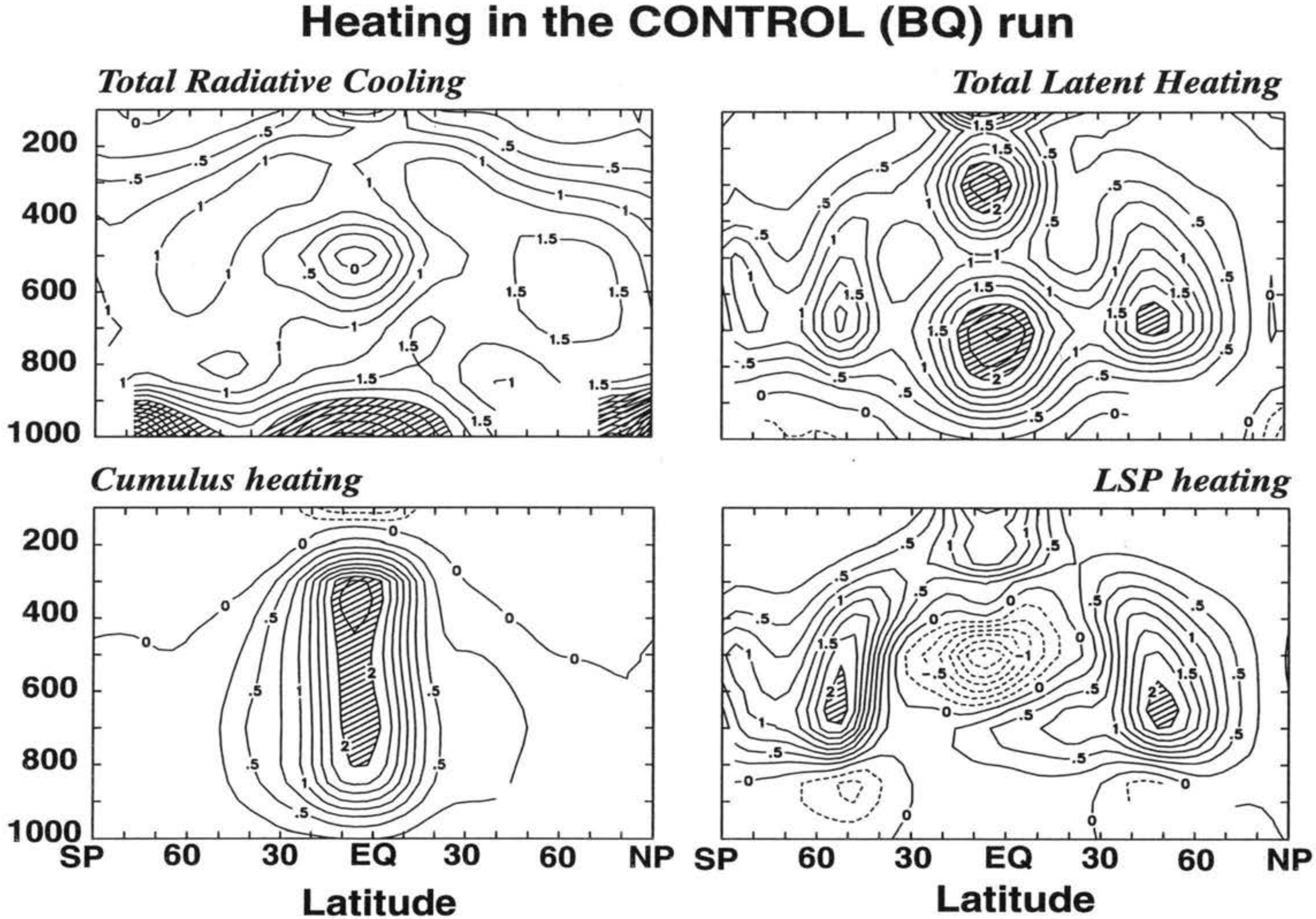

FIGURE 4.6: Zonal-mean January radiative cooling, total latent heating, cumulus heating, and LSP heating in the BQ run. The contour interval is 0.25 K day^{-1}. Areas larger than 2 K day^{-1} and smaller than -2 K day^{-1} are shaded.

sponds immediately to the supersaturation caused by the cumulus detrainment. Fig. 4.6 shows the cumulus heating, LSP heating, total latent heating, and the total radiative cooling of the control run.

The total radiative cooling has a minimum at 500 mb, the anvil cloud base, in the tropics. Strong and extended radiative cooling due to water vapor continuum appears near the surface in the summer hemisphere. The minimum at 500 mb indicates that the anvil in the model puts a "scale selection" on the cumulus convection. It is a forcing (destabilization) for deep cumulus but resistance (stabilization) for shallow cumulus. This can be seen in the Fig. 24 of Randall *et al.* (1989) which shows the change of cumulus incidence due to the cloud radiative forcing. Their tropical cumulus incidence increased from 35% to 85%, when the cloud radiative forcing (mainly anvil effects) was removed. Without much change in the precipitation, the increase of cumulus incidence most likely comes from shallow convection.

The cumulus cooling above 200 mb is due to the evaporation of the detrained condensates. LSP then recondenses and causes warming. Re-evaporation of the falling LSP results in the LSP cooling between 400 mb and 600 mb. Two mid-latitude maxima of the latent heating are due to LSP, which also exhibits a maximal evaporative cooling near the tropical anvil cloud base. The radiative cooling minimum at 500 mb actually becomes a radiative warming in BK. Fig. 4.7 shows the same fields from the BK run. The differences between these two runs in the same fields are shown in Fig. 4.8.

The heating fields from the BK run are qualitatively similar to those from the BQ run but intensities are different. The minima of radiative cooling and cumulus heating at

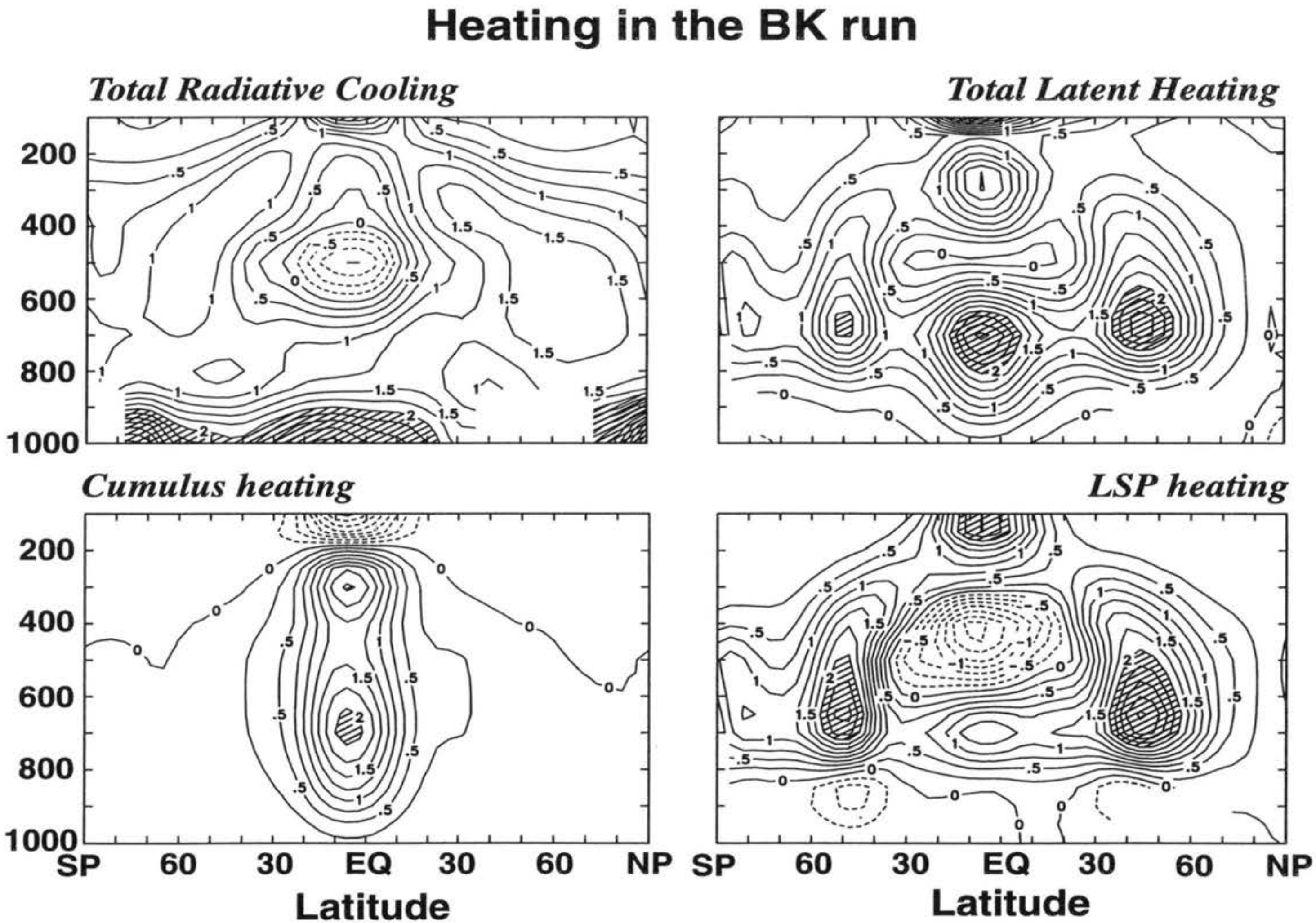

FIGURE 4.7: Same as Fig. 4.6, except for the BK run.

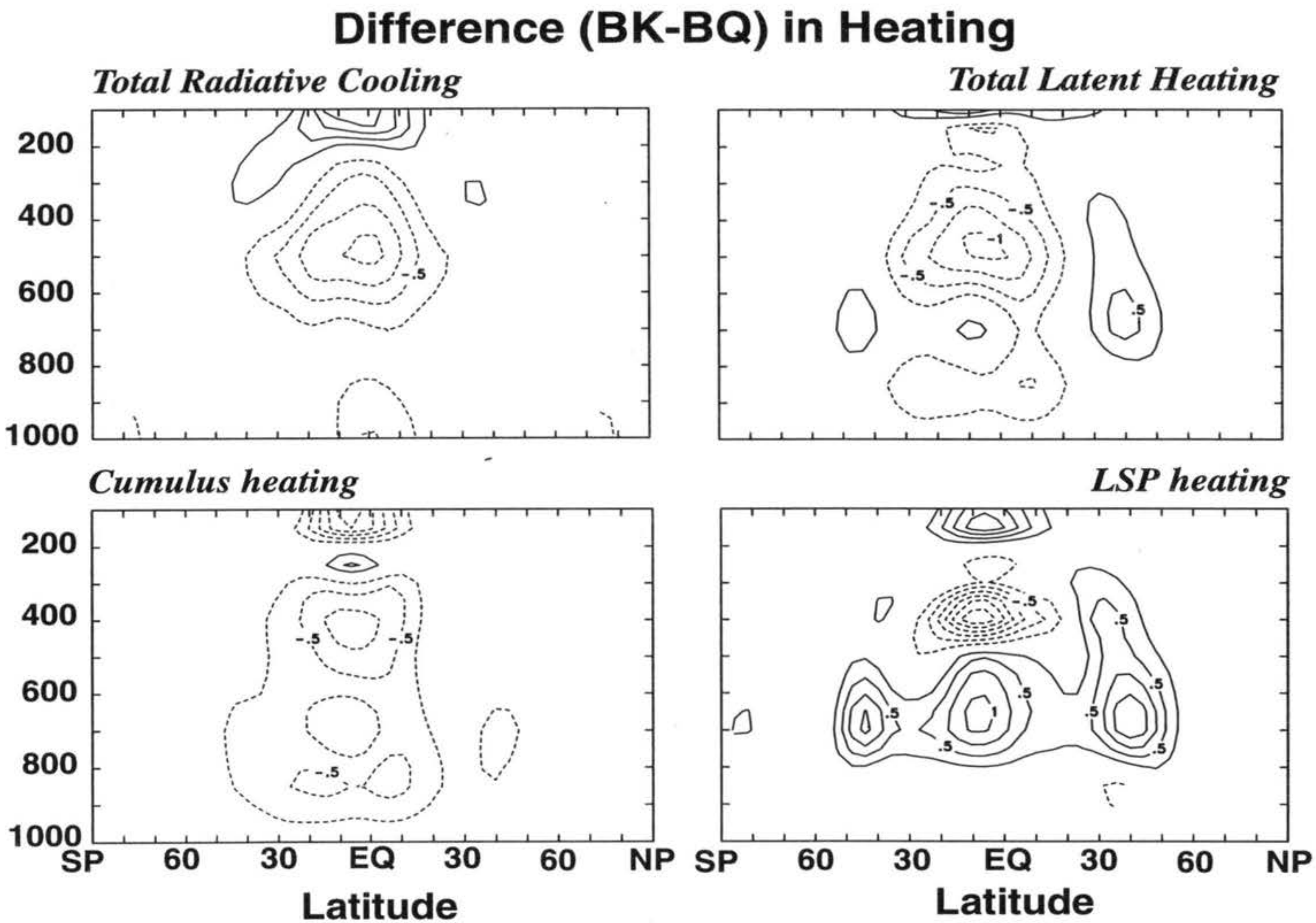

FIGURE 4.8: Difference between Fig. 4.7 and Fig. 4.6.

500 mb in the tropics both intensify. We can see in Fig. 4.8 that both the total latent heating and the total radiative cooling generally decrease from BQ to BK. The decrease of radiative cooling minimum (actually increased warming) at the anvil cloud base in the BK run is apparently associated with the increased anvil incidence.

We have mentioned that the anvil clouds favor deep convection over shallow convection. The intensified anvil in the BK run further favors deep convection, because the radiative warming at 500 mb tends to enhance the static stability below and reduce it above. (The increased radiative cooling above 200 mb also helps.) We can consider the January zonal mean as the state of "quasi-equilibrium". The enhanced anvil-radiative effects are then a "large-scale forcing" for the cumulus convection. This forcing is positive for deep convection but negative for shallow convection. Put in another way, the weaker static stability above 500 mb makes cumulus heating less efficient there, and the stronger static stability below does the opposite. (For same amount of cumulus mass flux, strong static stability means strong cumulus-induced subsidence warming. The same amount of mass flux is efficient in cumulus-induced warming.) This explains why the cumulus heating maximum moves down to 700 mb (comparing Fig. 4.6 and Fig. 4.7).

In the BK run, the cumulus clouds detrain less mass almost everywhere except near the tropical tropopause above 200 mb. The difference in detrainment mass flux between BK and BQ is shown as a function of latitude and pressure in Fig. 4.9. The increased detrainment mass near the tropical tropopause in the BK run corresponds to stronger detrainment cooling there, which in turn leads to a stronger large scale condensation and stronger re-evaporative cooling between 300 and 500 mb.

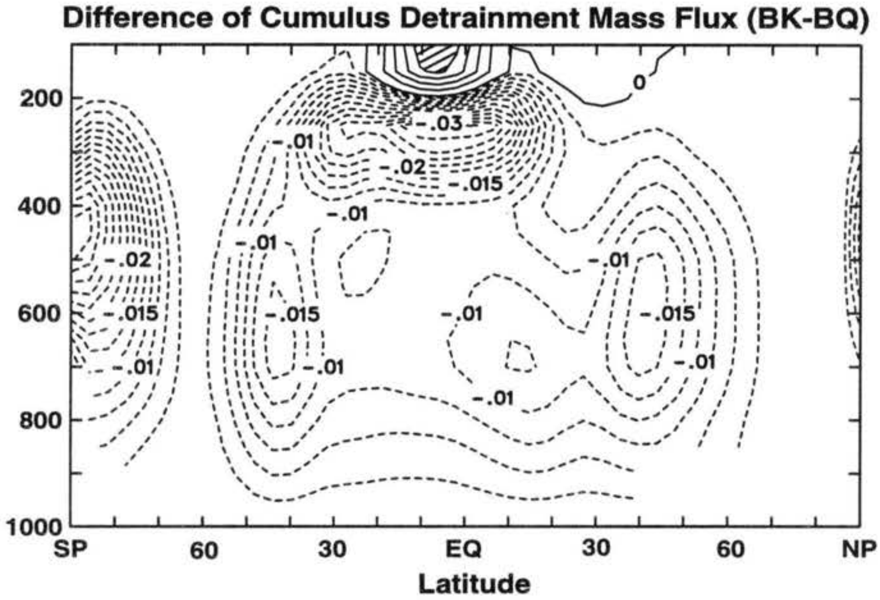

FIGURE 4.9: Difference between BK and BQ in cumulus detrainment mass flux. Dashed lines are contours below zero with an interval of 0.0025 hr^{-1}. Values of the solid lines are .0, .01, .02, .03, and .04 hr^{-1}, respectively. Shaded region is larger than 0.04.

Fig. 4.10 shows the cumulus drying of the BQ and BK runs and their difference. The prognostic CKE elevates the drying maximum and at the same time weakens it. As a result, the prognostic CKE tends to cause less cumulus drying at 800 mb and below, but stronger drying between 800 mb and 500 mb. In other words, less moisture is transported upward by cumulus clouds in the BK run.

Fig. 4.11 shows the differences between the experiments BK and BQ (BK-BQ) in monthly-mean latitude-pressure plots. Three panels are temperature, relative humidity, and water vapor mixing ratio. The major differences occur in the tropics. The prognostic CKE results in a warming up to 2.5 K at 500 mb and a cooling up to -3.5 K at the tropo-

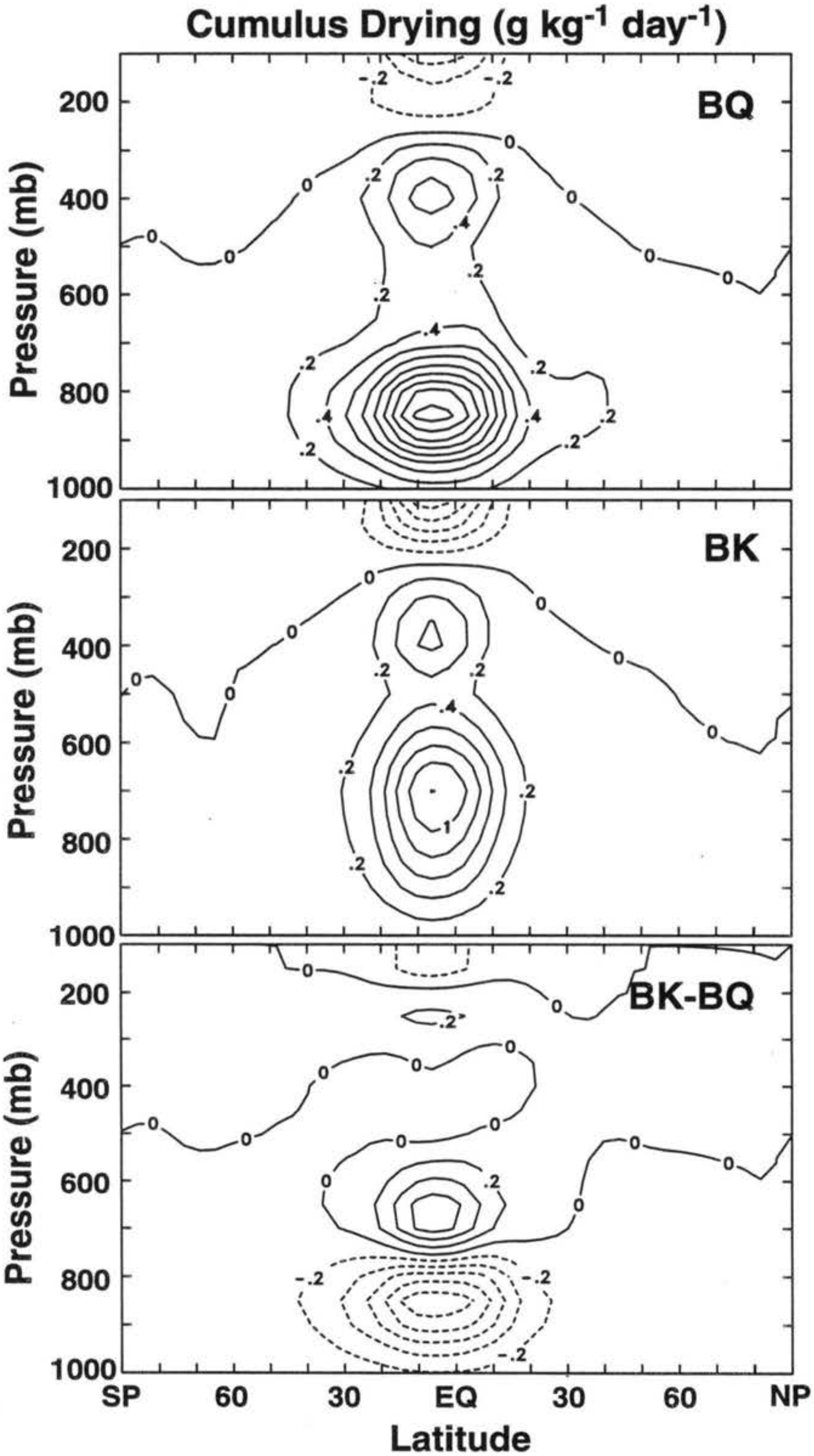

FIGURE 4.10: Cumulus drying of BQ, BK, and (BK-BQ). Contour interval is 0.2 g kg^{-1} day^{-1}.

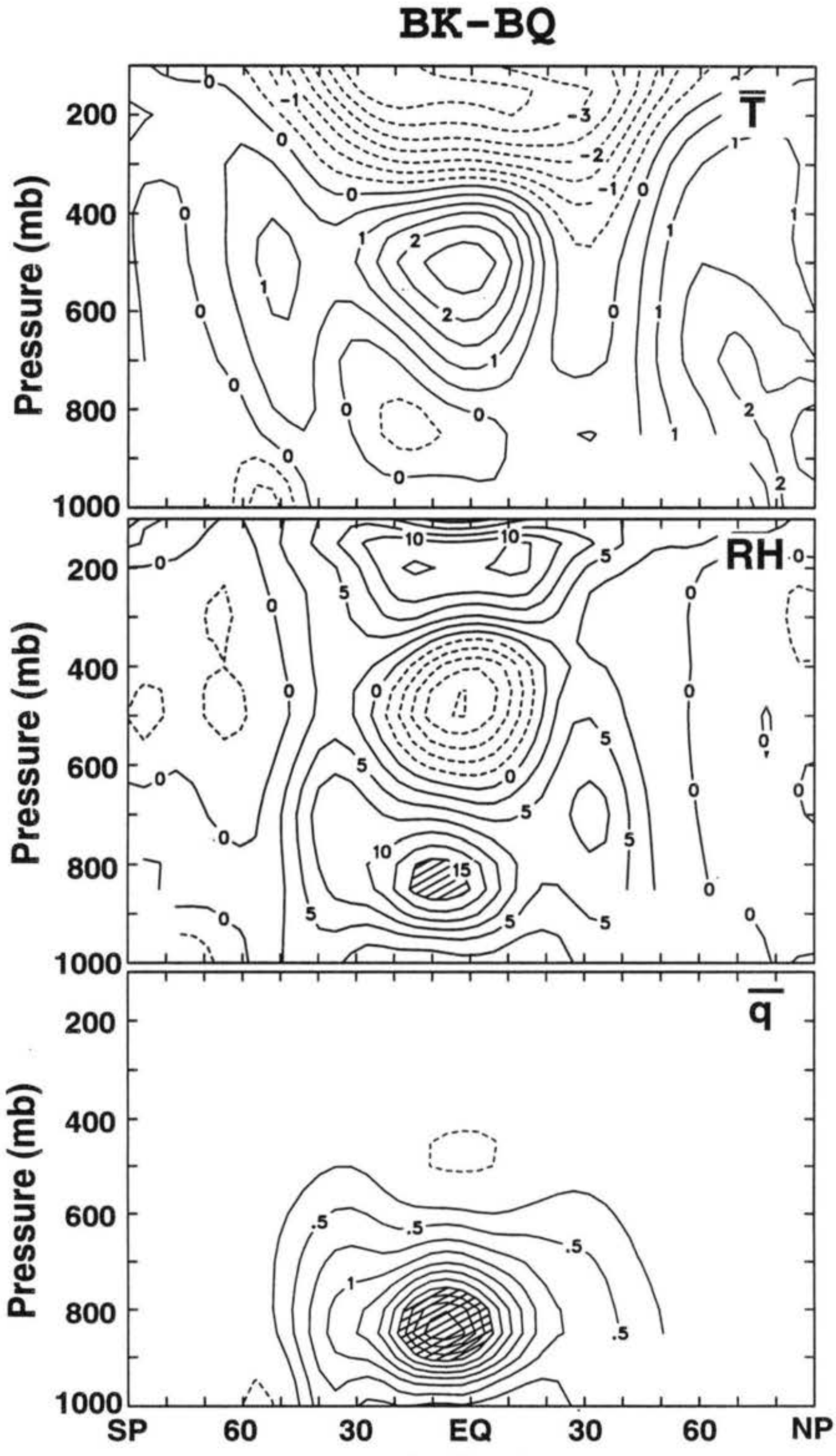

FIGURE 4.11: Difference of temperature, relative humidity, and mixing ratio between experiments BK and BQ. The contour intervals are 0.5K, 5%, and 0.25 g kg^{-1}, respectively. Shaded areas are above 15% for relative humidity, and above 2 g kg^{-1} for specific humidity. The zero-contour lines are omitted in the mixing ratio plot.

pause. This coincides with the change in radiative heating but contradicts the change in latent heating, as shown earlier. The cooling (warming) coincides with the higher (lower) relative humidity at the same positions. The relative humidity maximum at 850 mb (15% increase) in the summer tropics is due to the mixing ratio increase (of up to 2.75 g kg^{-1}). The change in the mean moisture field agrees with the change in cumulus drying.

The temperature in the tropics is determined by a balance among radiation, cumulus convection, and the large-scale vertical motion, since the effects of horizontal advection are weak in this region. The similarity between the change in total radiative cooling and that in total latent heating means little contribution from the change in the large-scale vertical motion and hence the mean meridional circulation (to be discussed later). Both the incoming solar radiation and cumulus convection are most active in the tropics. Less latent heating is associated with a weaker radiative cooling in the BK run and hence the precipitation decreases, both globally and in the tropics. As expected, most of the precipitation decrease occurs in the tropics, except for the local increase of up to 6.5 mm day^{-1} North of Australia. Most of the precipitation decrease is over the oceans.

4.2.1.4 Cloud-Radiation Interactions

Broadly speaking, there are two mechanisms of cloud-radiation interaction: the "albedo effect" and the "greenhouse effect" (e.g. Tiedke, 1985 and Randall *et al.*, 1989). The albedo effect is a negative feedback that occurs over land. When the cumulus convection produces anvil clouds that block the sunlight, less solar radiation reaches the land surface. This reduces the surface sensible and latent heat fluxes. Reduced surface heat fluxes in turn reduce the cumulus convection. The greenhouse effect is a positive feedback that dominates over the oceans. The existence of anvil clouds reduces the OLR. Since the oceans have much larger thermal inertio (heat capacity), surface heat fluxes do not change much regardless of the change in the incoming solar radiation. (In the model, the SST is actually fixed.) Therefore, the anvil clouds tend to warm the whole atmospheric column in the region of convection, relative to neighboring columns. Enhanced large-scale rising motion due to this warming favors even more cumulus convection.

However, neither of these two mechanisms is obvious when we compare BQ and BK, where the increased anvil incidence in BK does significantly change the radiation budgets at the top of the model atmosphere. The sensible heat flux decrease in BK (not shown) does have maxima over the South-hemisphere land surfaces, while most of the changes in surface evaporation occur over the oceans. The global-mean changes in sensible and latent heat fluxes are of comparable size. The decrease of the sensible flux over the land surfaces does not reduce the precipitation there, simply because there is little precipitation over land to start with in the BQ run.

The fact that neither the "greenhouse effect" nor the "albedo effect" is obvious in comparing BQ to BK suggests that the difference between these two experiments is not simply a radiative forcing. After all, the interactions between the cumulus convection and the large-scale environment must have changed somehow when we replace the quasi-equilibrium approach with the prognostic CKE.

4.2.1.5 The Prognostic CKE and Cumulus Anvil Incidence: Point-by-Point

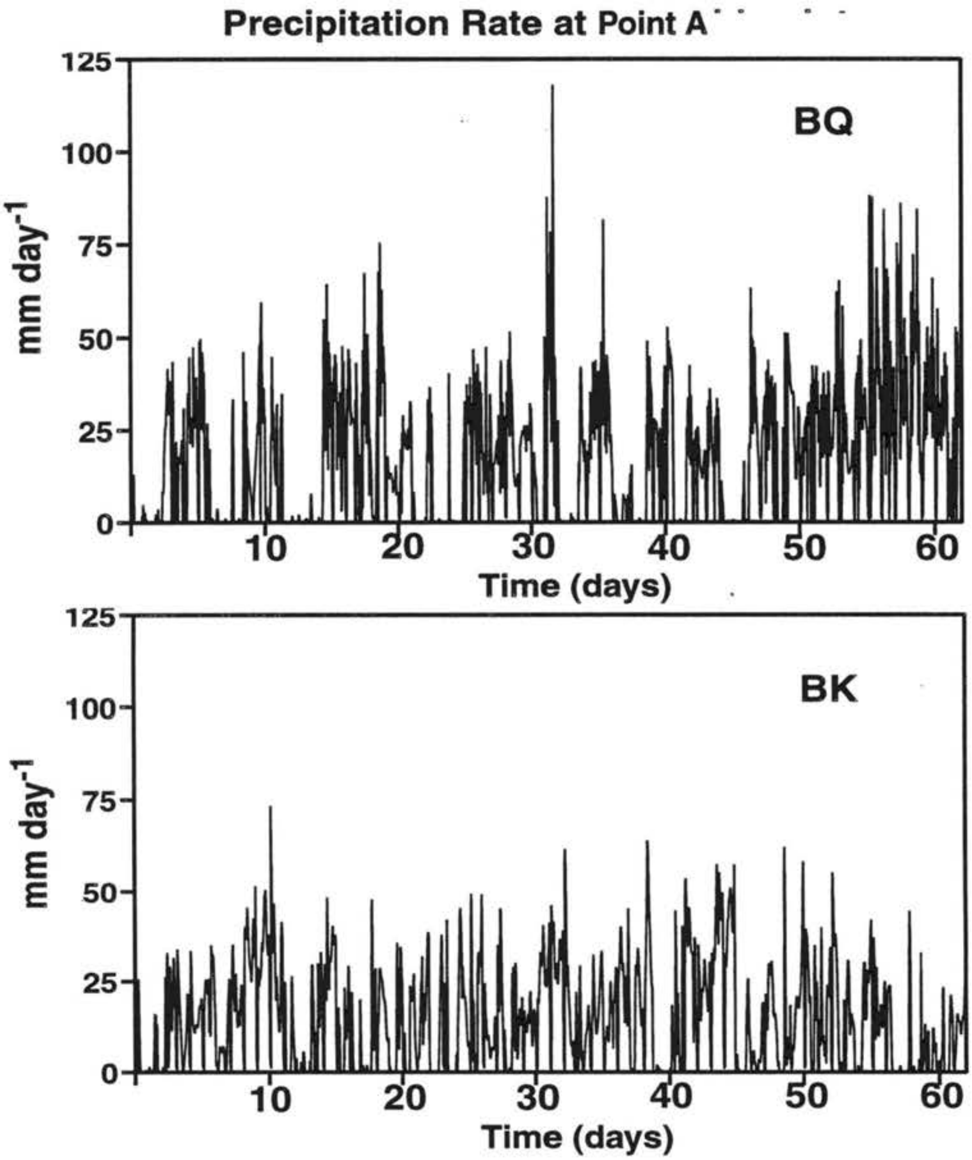

FIGURE 4.12: Time series of the cumulus precipitation rate at a specific grid point north of Australia, from the two different runs: BQ and BK.

Analysis

As mentioned earlier, the anvil incidence increases dramatically when we replaced

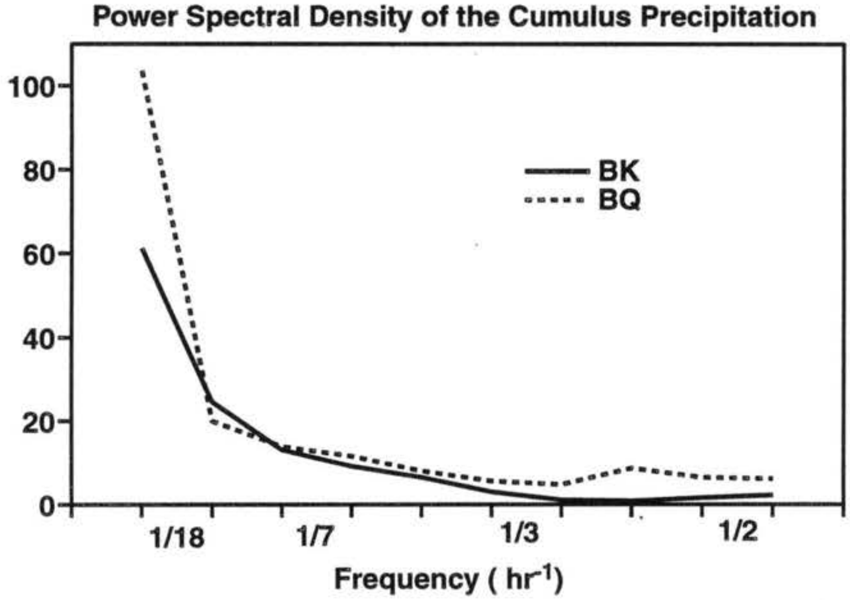

FIGURE 4.13: Power spectrum of the cumulus precipitation as a function of frequency. The original spectrum has been grouped into 10 frequency channels.

the quasi-equilibrium closure with the prognostic CKE approach. Why does the prognostic CKE cause the dramatic change in the anvil incidence? More precisely, how does the difference in the cumulus parameterization lead to the large difference in the anvil incidence? In this subsection, we analyze the data for two specific grid points and try to find the explanation.

We first look at the time evolution of cumulus precipitation over the ocean north of Australia (referred to as "point A"), where heavy precipitation often occurs in the two runs. Fig. 4.12 shows the time series of the cumulus precipitation rate for the two runs. We can see that in the BQ run, cumulus convection quite often produces huge precipitation intermittently. The difference between these two time series can be seen more clearly in Fig. 4.13, which shows the power spectral density of the cumulus precipitation for both the BQ and BK runs. Notice that Fig. 4.13 is a "band" power spectrum, in which we show only the "accumulated" power in frequency intervals. The method of calculating the power spectrum is included in Appendix B.

We can see from Fig. 4.13 that BQ has much more power than BK at the high-frequency end of the spectrum. In BQ, cumulus precipitation changes more violently on time scales of 3 hours or less. This part of the spectrum may account for the tripled anvil incidence from BQ to BK, since the differences between the two runs are not as large (percentage-wise) in the lower- frequency part of the spectrum. The precipitation can come from either deep or shallow clouds, while the anvil incidence counts only the occurrence of deep clouds. The cumulus precipitation does not go to zero although its change is violent. This suggests that shallow convection is more persistent in the BQ run.

As another example, Fig. 4.14 shows 20-day time series of the cumulus precipitation rate at "point B", locating at the middle of the Pacific Ocean (180 longitude, Equator), where the January precipitation rate is similar for both runs while the anvil incidence is about 37% for BQ and 82% for BK. In the 20-day period with BQ, there is no cumulus precipitation 50% of the time; on the other hand with BK, cumulus precipitation occurs in 70% of the time. (Note that this time series used the February results and the time period is only 20 days, therefore, the cloud incidences may not be the same as those shown

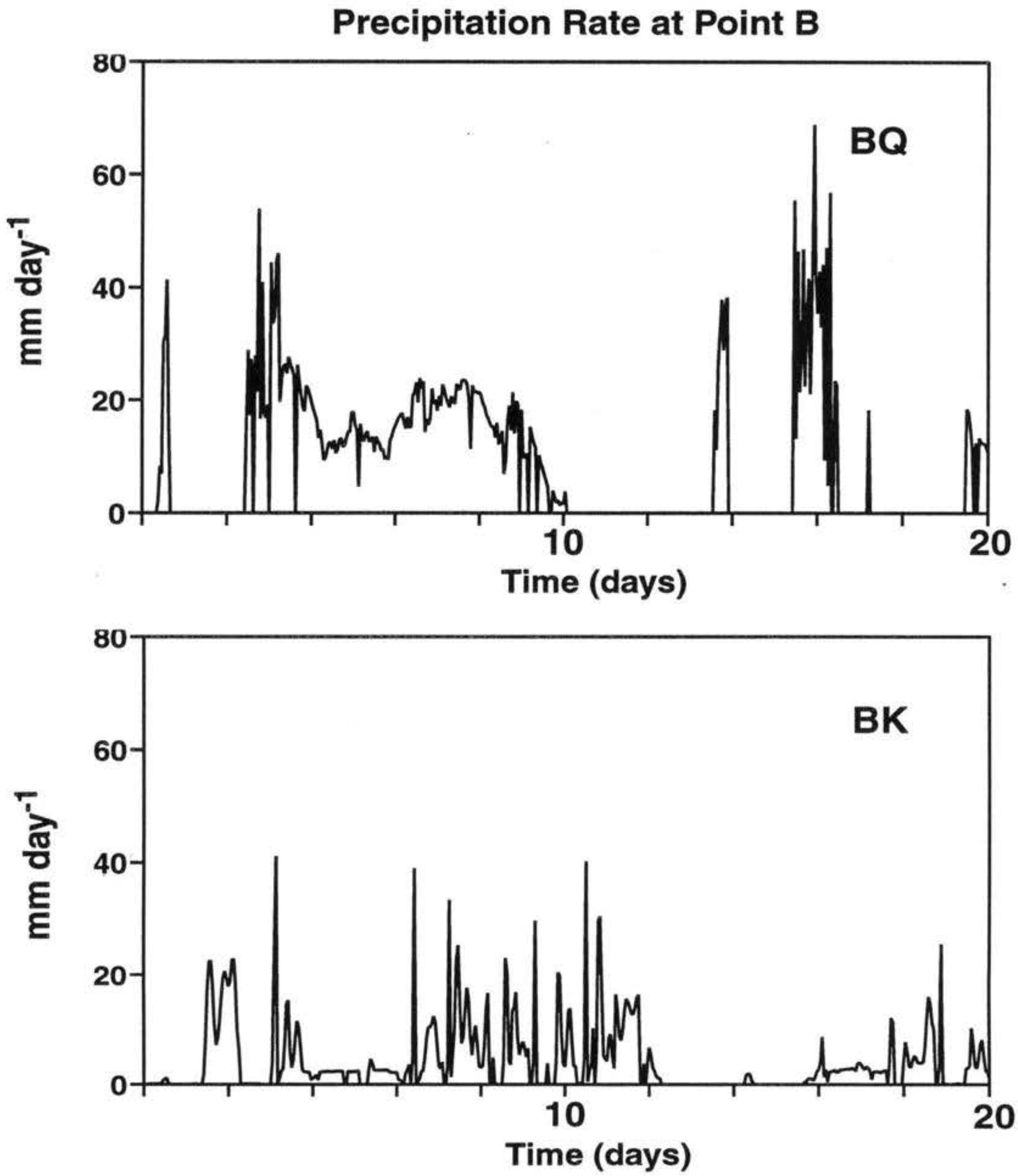

FIGURE 4.14: Same as Fig. 4.12 except for at point B for 20 days only.

earlier in the map.) Comparing with the anvil incidence, it seems that BK run often contains weak (in mass flux and precipitation) but deep clouds. On the other hand, the shallow cumulus in the BQ run precipitates more.

The persistency of the deep cumulus convection (and hence the larger anvil incidence compared to the BQ run) in the BK run suggests that in the BQ run, when the deep cumulus clouds occur, they somehow "over-consume" the cloud work function and drop a lot of precipitation, so that the large-scale forcing cannot accumulate enough positive cloud work function immediately.

The BQ run produces a planetary albedo that is close to that observed, while the cumulus convection in the BK run produces anvils that are optically too thick and hence an excessive planetary albedo. How does the cumulus convection control the planetary albedo? The cumulus clouds can change the albedo by changing the optical thickness of the anvil clouds. With the binary anvil, the major way to change the optical thickness of the anvil clouds is to change the anvil incidence. The anvil clouds determine the radiative cooling in the atmosphere and radiative fluxes at the surface, which in turn are the major factors in determining the cumulus convection (other than the large-scale vertical motion).

How does the interaction between the parameterized cumulus convection and anvil clouds work? The anvil clouds cause warming at 500 mb and below, and cooling above 300 mb. This is equivalent to the effects of cumulus clouds that detrain above 300 mb. The intensity of the cumulus effects depends on the cloud-base mass flux and the environmental sounding, while the efficiency of the anvil's radiative heating/cooling depends on the depth of the anvils and their incidence. The model has to find a mass flux that determines the strength of the cumulus convection and a frequency of convection that determines the radiation field, and the cumulus convection has to balance the radiation in a certain way. Consider an hypothetical atmospheric column. When the anvil incidence (frequency of deep convection) is high, we need less latent heating and hence the total cumulus mass flux should be smaller, if the environmental sounding is the same.

4.2.2 FK vs. BK: Effects of Fractional Anvils

4.2.2.1 The Fractional Anvil

We assume that the anvil clouds usually do not fill the whole grid-box, and the fraction covered by the anvil is

$$f = aM_B \leq 1. \tag{4.4}$$

The shortwave optical depth is

$$\tau_{sw} = f\,\tau_{anv} + (1-f)\,\tau_{cs}, \tag{4.5}$$

where τ_{anv} and τ_{cs} are the optical depths for anvil and clear sky, respectively. The longwave emittance is

$$\varepsilon = f\,\varepsilon_0. \tag{4.6}$$

Here the value $a = 75\ \mathrm{m^2\,s\,kg^{-1}}$ was obtained by trial and error. It was chosen so that the global-mean OLR (outgoing longwave radiation) is close to that observed. ε_0, expressed in (4.1), is the longwave emittance when the layer is completely filled with anvil clouds. The requirement $aM_B \le 1$ means that when M_B exceeds 4.7 mb hr^{-1}, the anvil clouds cover the whole grid box.

As a simple check on the statistical significance of the results of the 2-month experiments, we compared the cumulus precipitation from the one-month January mean with that from a 10-year January mean with the same version of the model. Fig. 4.15 shows the cumulus precipitation from FK of a 2-month run and a 10-year run, compared with that from the BK run. Both the global-mean cumulus precipitation and its distributions are almost identical between the two FK runs, especially when compared to the BK run. In other words, the (global-mean) differences between the two FK runs are much smaller than that between FK and BK. (The latter is 20 times as large.) This means that the comparison between 2-months runs can show high “signal-to-noise” ratio. (In this case, the “signal” is the effects of the fractional anvils.) Many other fields, such as the surface evaporation, cloud-base mass flux, zonal mean cumulus heating, etc. were also compared. High similarity between the two FK runs is seen in all fields, especially in the tropics. Note that we have used $\alpha = 10^7$ m^4 kg^{-1}, instead of $\alpha = 10^8$ m^4 kg^{-1}, in the above comparison because $\alpha = 10^7$ m^4 kg^{-1} had been chosen in the 10-year run in the first place.

4.2.2.2 Radiation Budgets

Since the coefficient in the fractional anvil is chosen to make the OLR realistic, the fractional anvil results in optically thinner anvil clouds. This can be seen in Fig. 4.16, which shows the differences in OLR and the absorbed solar radiation at the top of the at-

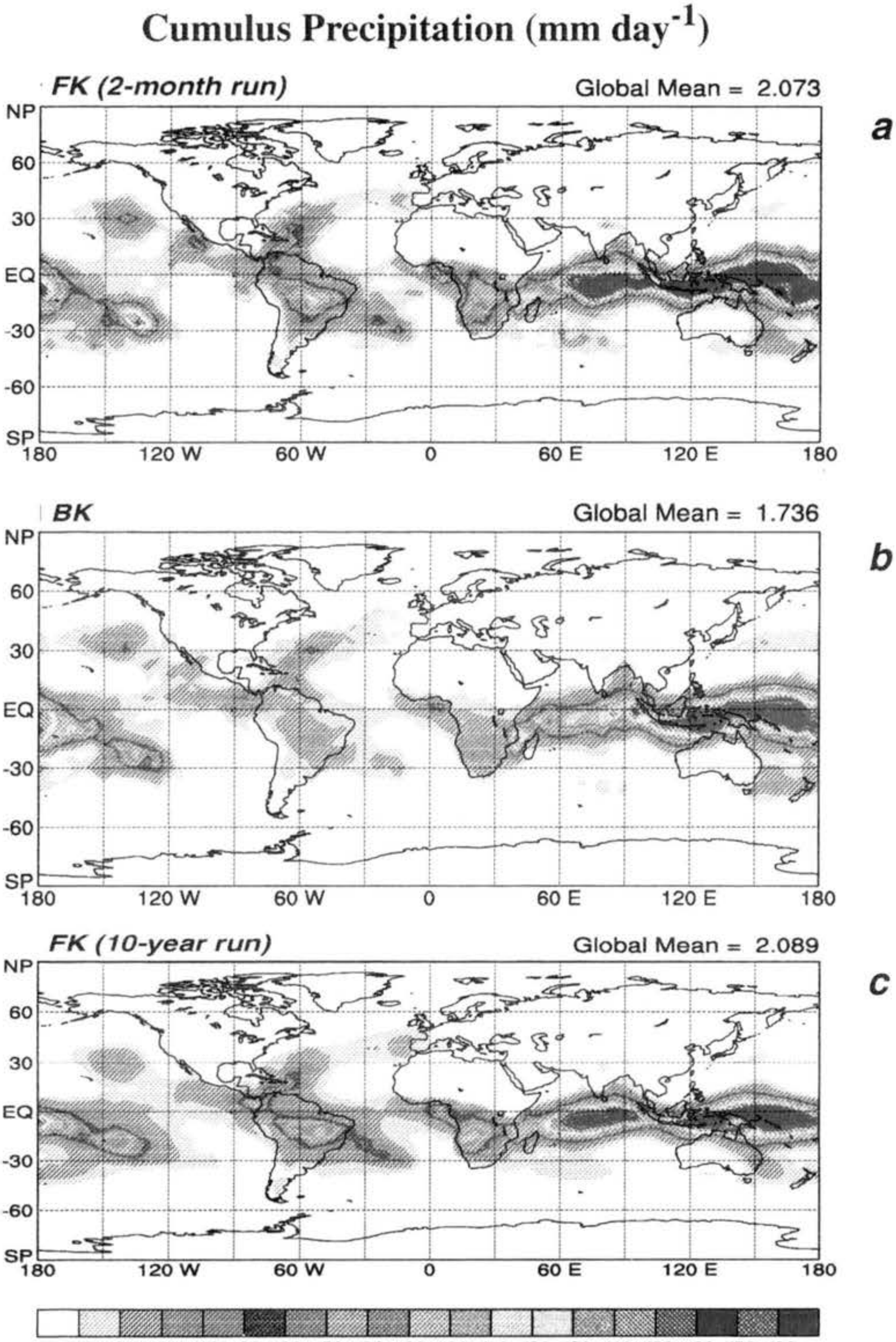

FIGURE 4.15: January monthly-mean cumulus precipitation from the two 2-month runs (*a* and *b*), and the 10-year run result. Global mean is shown at the upper right corner of each plot.

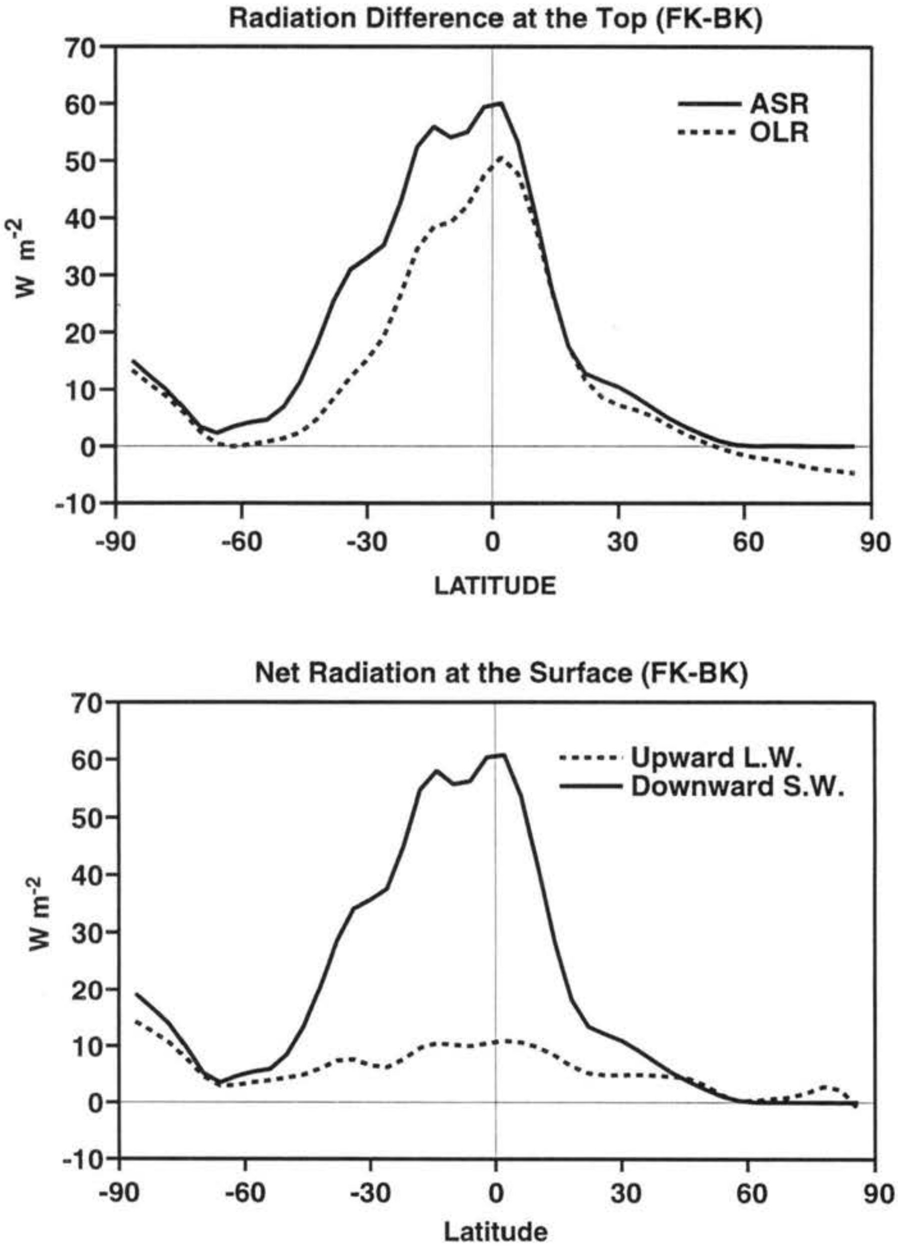

FIGURE 4.16: Zonal mean difference between the FK and BK runs, showing OLR (outgoing longwave radiation, dashed line) and ASR (absorbed shortwave radiation), upper panel. The lower panel shows the difference of the upward longwave and downward shortwave at the surface.

mosphere, caused by the change to the fractional anvils. In most of the tropics, much more solar radiation (up to 60 W m^{-2}) is absorbed by the Earth-atmosphere system. In the meantime, the OLR also increases where the absorbed solar radiation increases, but not as much. As a result, there is a net gain of radiative energy at the top of the atmosphere from 10^oN to 60^oS.

Also shown in Fig. 4.16 is the difference radiative fluxes at the surface. Comparing the two pictures in Fig. 4.16, we can see that most of the increased incoming solar radiation goes into the surface. However, the increase of the upward longwave is small and not enough to compensate the OLR loss at the top. Therefore, the atmosphere as a whole has a net radiative energy loss. In order to satisfy the energy balance of the atmosphere, stronger surface sensible flux or more latent heat release has to be involved.

The larger incoming solar radiation causes more heating (more absorption of solar energy) at the land surfaces, and hence more surface evaporation. (The change of sensible heat flux is relatively small.) This results in maximal increases of precipitation over the summer-tropical land surfaces — Amazon and South Africa. Other than over the land surfaces, maxima of precipitation increases are also seen over the Indian Ocean and South western Pacific Ocean.

Fig. 4.17 shows the latitude-pressure distribution of the difference in total radiative cooling between the FK and BK runs. The difference is mainly between 30^oN and 30^oS. The longwave cooling accounts for most of the radiative difference. The fractional anvils result in radiative warming above 200 mb and radiative cooling (stronger longwave cool-

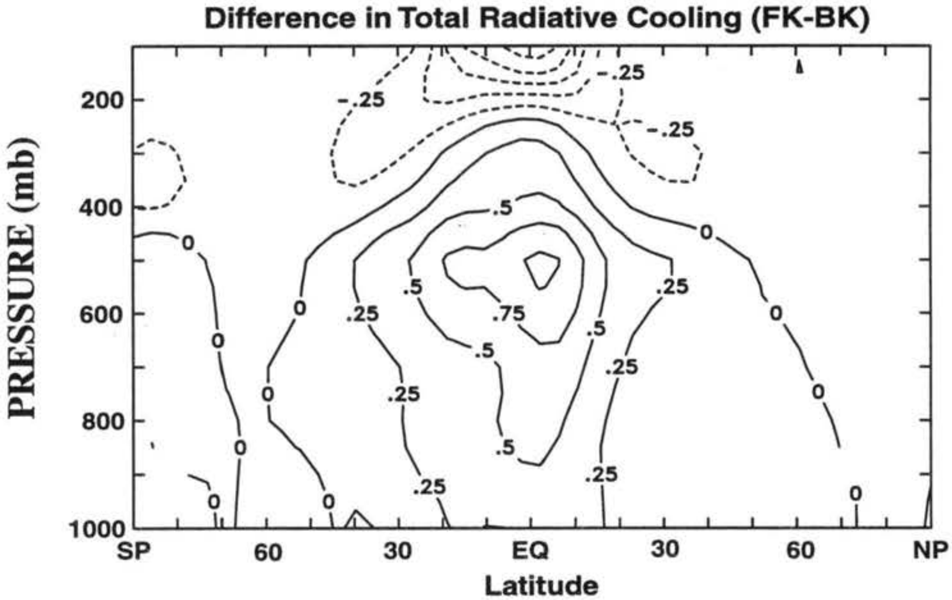

FIGURE 4.17: Zonal-mean difference of the total radiative cooling between the FK and BK runs (FK-BK). The contour interval is 0.25 K day^{-1}.

ing) through the whole layer below, with a maximum at 500 mb. The maximal differences are more than 1 K day^{-1} and lean toward the winter hemisphere.

4.2.2.3 Cumulus and LSP Heating

Fig. 4.18 shows the difference between FK and BK in cumulus and LSP heating and moistening. Cumulus heating is generally stronger for FK, especially between 500 and 200 mb, with a maximum of more than 1 K day^{-1} between 300 mb and 400 mb. Negative values above 200 mb means stronger detrainment cooling, which is consistent with the stronger subsidence heating below. The cumulus heating difference has a comparable

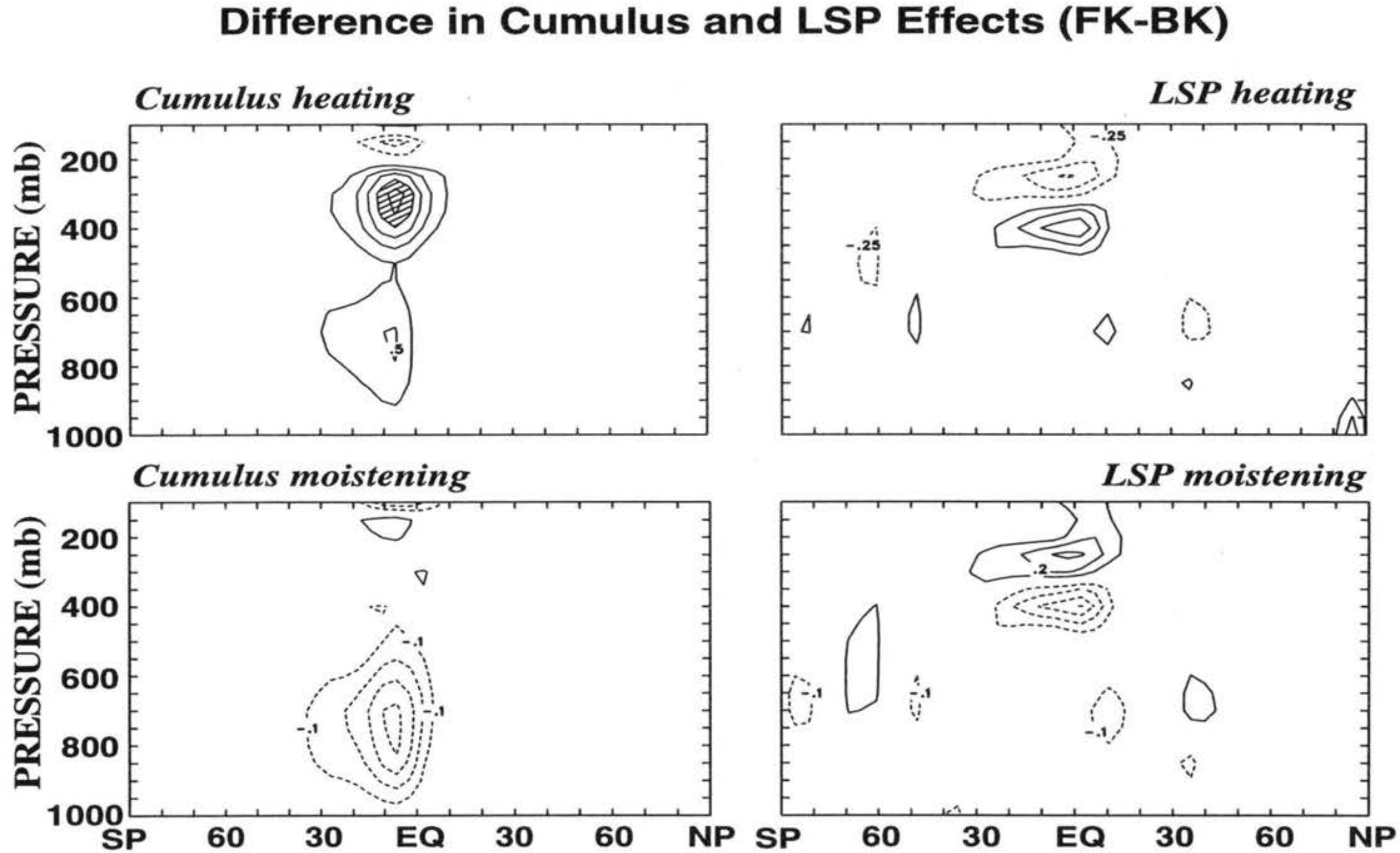

FIGURE 4.18: Difference between FK and BK in cumulus heating/moistening and LSP heating/moistening. The contour intervals are 0.25 K day^{-1} for heating and 0.1 g kg^{-1} for moistening. Dashed lines represent negative values. Zero lines are omitted. Shaded areas are larger than 1 K day^{-1}.

maximum with that of the radiative cooling, except that the radiative cooling maximum is lower (500 mb) and on the other side of the Equator. Although the cumulus detrainment cooling is stronger near the tropical tropopause (above 200 mb), the large-scale condensational heating is weaker there. The LSP shows less heating between 200 and 300 mb and less cooling between 300 and 500 mb. The LSP moistening has the opposite signs to the LSP heating, as expected. The stronger cumulus heating above 500 mb is associated with a larger static stability, while the stronger heating below (where the static stability is actually smaller) must be due to the stronger cumulus mass flux. More drying below 500 mb and more heating above means more latent energy transported vertically in FK than in BK.

Fig. 4.19 shows the differences in zonal-mean temperature and specific humidity. The fractional anvils result in an overall colder atmosphere, except for the tropical tropopause. This is similar to the distribution of the difference in the radiative cooling. The maximal cooling by the fractional anvils occurs at 500 mb and is almost symmetric about the Equator. This makes the atmosphere more statically stable above 500 mb and less stable below and favors shallow convection. This means that shallow convection can happen more easily, or that less buoyancy from latent heat release is needed for shallow convection. The FK run also shows a dryer atmosphere below 500 mb, especially in the tropics.

4.2.2.4 Cumulus and Anvil Incidences

Anvils occur much less often in the FK run than in the BK run, while the cumulus incidence is not changed much. The average depth of the anvil clouds also decreases. Fig.

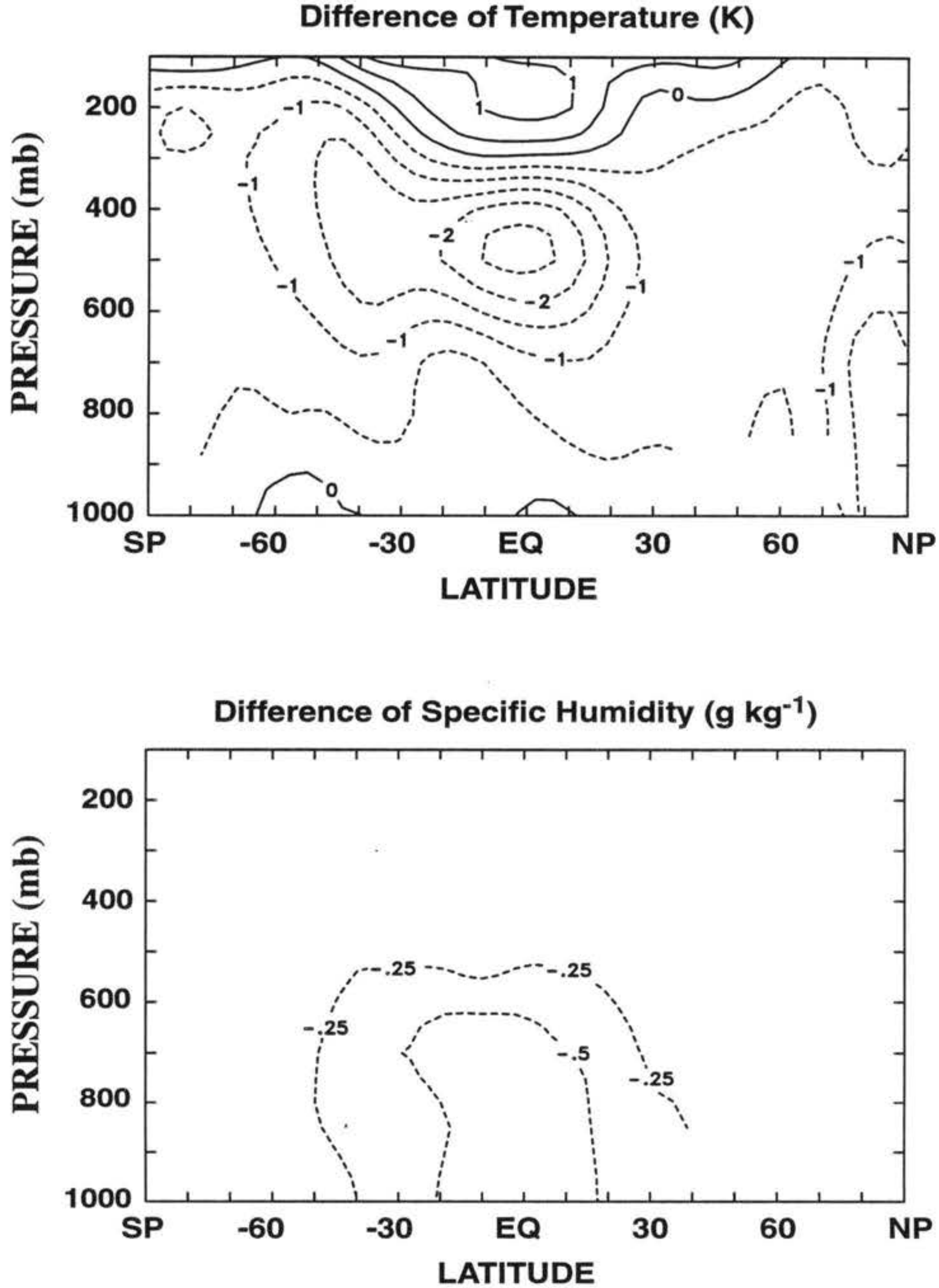

FIGURE 4.19: Difference of temperature (a) and specific humidity between FK and BK. The contour interval is 0.5 K for the temperature plot, and 0.25 g kg^{-1} for the specific humidity plot.

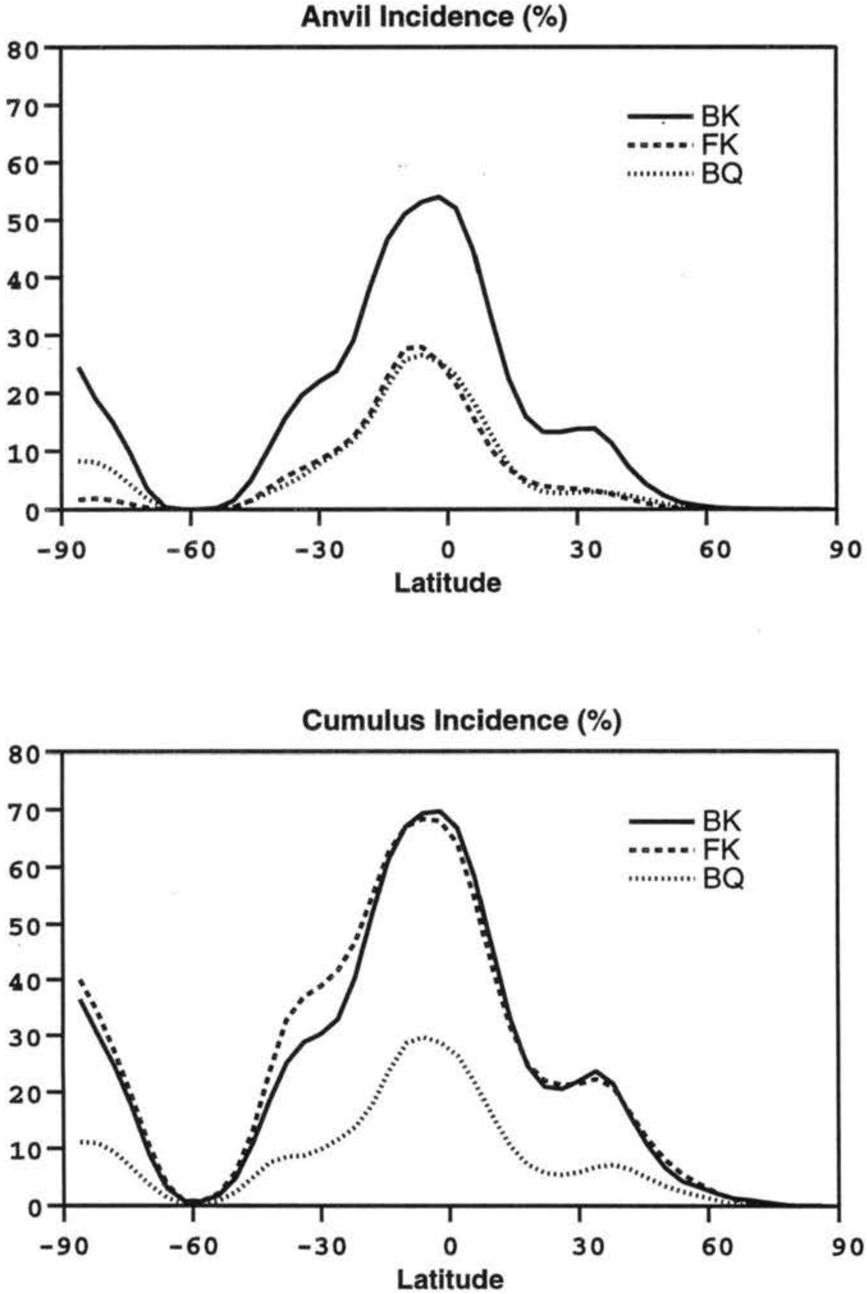

FIGURE 4.20: Anvil (above) and cumulus incidences for experiments BK (solid), FK (dashed), and BQ.

4.20 shows the January zonal-mean cumulus and anvil incidences for all the three runs: BK, FK, and BQ. The anvil incidence from BK and the cumulus incidence from BQ are dramatically different from the others. In the tropical area, BK has both large cumulus and anvil incidences (~ 60%), and BQ has both small cumulus and anvil incidences (~25%). Once convection occurs in BK or BQ, it usually can reach 500-mb or higher levels and so forms anvil clouds. This does not happen in FK. In the regions of 60% or higher cumulus incidence in the tropics, less than 30% of the area contains convection deeper than 500 mb. This suggests that the binary anvils suppress shallow convection, or that the fractional anvils favor shallow convection.

4.2.2.5 Mean Meridional Circulation

The change of the distributions of diabatic heating due to the different cumulus parameterization or the fractional anvil parameterization may change the large-scale dynamics. We now compare the simulated global-mean streamfunction of the MMC (mean meridional circulation) with that from the European Center for Medium-Range Weather Forecasts (ECMWF) observations. The Hadley cells with BK and FK are stronger than observed and stronger than in the control run. The similar strength of the MMC in BK and FK suggest that the intensification of the MMC cannot be directly explained by the use of the fractional anvil or the prognostic CKE.

It should be kept in mind, however, that even the observational estimates of the mean meridional circulation can vary by a factor of two or more. The MMC from 1988-1992 ECMWF analyses in Hack et al. (1994) showed a much stronger maximum of the main

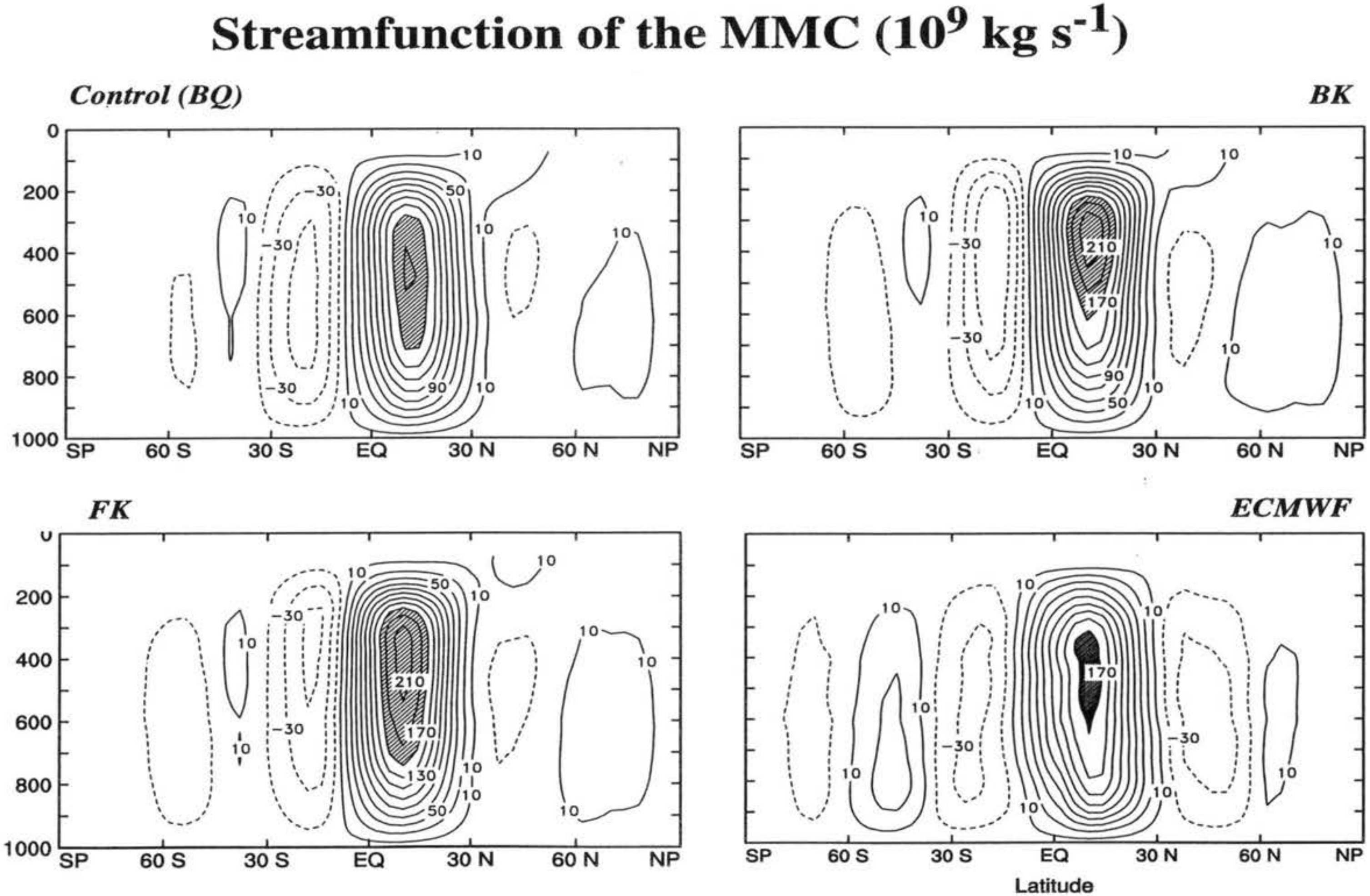

FIGURE 4.21: Streamfunction of the mean meridional circulation. Three plots from the experiments (BQ, BK, and FK) and one from the ECMWF observations are shown. The contour interval is 20×10^9 kg s^{-1}. Regions with values larger than 170×10^9 kg s^{-1} are shaded.

Hadley cell (up to 220×10^9 kg s^{-1} vs. 170×10^9 kg s^{-1} shown in Fig. 4.21). The MMC's obtained with both BK and FK are very close to the 1988-1992 ECMWF analyses.

4.2.3 Inter-comparisons

	BQ	FQ	BK	FK
Cumulus Precipitation (mm / day)	2.08	2.12	1.38	1.76
Total Precipitation (mm / day)	3.6	3.6	3.3	3.7
M_B (mb / hr)	0.63	0.64	0.38	0.51
OLR (W m^{-2})	229	231	207	224
ASR (W m^{-2})	250	254	221	246
ASR-OLR (W m^{-2})	21	23	14	22
Net L.W. at the Surface (W m^{-2})	66	67	54	60
Net S.W. at the Surface (W m^{-2})	190	194	159	185
Surface Latent Heat Flux (W m^{-2})	105	105	96	108
Surface Sensible Flux (W m^{-2})	8.9	9.2	3.9	4.9
Net Downward Heat Flux at the Surface (W m^{-2})	9.9	11.7	4.8	12.4
Precipitable Water (mm)	22.0	21.8	25.4	23.7
Planetary Albedo (%)	31	30	38	32

TABLE 4.2: Comparison of global means among the four experiments.

We have compared the prognostic CKE with the quasi-equilibrium approach when using the binary anvils. However, the binary anvils may not be an appropriate way to represent the radiatve effects of the anvil clouds. As discussed, the anvil clouds can be fractional according to observations and the use of the fractional anvils in the model also proves that the binary anvils suppress shallow convection.

When we replace the cloud work function quasi-equilibrium with the prognostic CKE *and when the anvils are binary*, both the anvil and cumulus incidences dramatically increase. This big difference between BK and BQ, however, is not seen between FK and FQ. The anvil incidence in the binary-anvil method is more directly related to the (monthly-mean) optical depth than in the fractional-anvil method. The monthly-mean optical depth depends only on the physical depth and the incidence of the anvil, in the binary-anvil case. However, with the fractional anvils, the optical depth can also be changed by the "fractional coverage", and anvil incidence is not as tightly related to the radiation anymore. It is, therefore, expected that the anvil incidence can be relatively insensitive to different cumulus parameterization methods, when the fractional anvils are used.

4.2.3.1 (FK-BK) versus (FQ-BQ)

After looking at the effects of the fractional anvils, we can also apply the fractional anvils with the quasi-equilibrium approach, in experiment FQ. The change from the binary anvils to the fractional anvils can be considered as a "forcing." The comparison between (FK-BK) and (FQ-BQ) shows the response of the two different cumulus parameterization approaches to this "forcing." For convenience in later discussions, we call the model using cloud work function quasi-equilibrium in the cumulus parameterization as a WQE system.

Some global-mean properties of all the four experiments are summarized in Table 4.2. In experiment FK, we chose the constant in the fractional anvil formula so that the global-mean OLR is close to the observed value. For the FQ run, however, we did not adjust this constant to give the observed OLR.

The changes in radiation (i.e., in the temperature budgets) from the binary anvils to the fractional anvils are smaller in the quasi-equilibrium approach than in the CKE approach. In both cases, almost all of the increased incoming solar radiation at the top of the atmosphere, goes into the Earth's surface. The difference occurs in the longwave radiation. The OLR increase from BQ to FQ is smaller than the longwave radiative flux from the Earth's surface into the atmosphere. This results in longwave energy convergence and reduces the net radiative energy loss in the atmosphere. The global mean net radiative energy loss is on the order of 100 W m^{-2}. The change from BQ to FQ in net radiation is only 4 W m^{-2}, but the change in surface sensible heat flux is 7.3 W m^{-2}. The sum of these two components results in a 10% decrease in the total precipitation. On the other hand, the stronger OLR-increase (than the change of the upward longwave flux at the surface) from BK to FK results in more net radiative energy loss in the atmosphere. This, with the almost unchanged surface sensible heat flux, is associated with a 10% increase in precipitation. In short, the differences in the two approaches of cumulus parameterization caused by changing the anvil representation from the binary anvil to the fractional anvil are the upward longwave radiation convergence/divergence in the atmosphere and the surface sensible heat flux.

From BK to FK, basically, we apply an "external" forcing to the Earth-atmosphere system — reducing the planetary albedo from 38% to 32%. This forcing leads to a net loss of radiative energy in the atmosphere and increases in cumulus precipitation. On the other hand, from BQ to FQ the change in planetary albedo is from 31% to 30%. Considering the change in albedo as an external forcing, the forcing in the FQ-BQ run is much smaller and does not cause changes as significant in other fields, such as precipitation, precipitable water, and surface evaporation, etc. Both the cumulus and anvil incidences are also essentially unchanged (not shown). Therefore, if we consider the change in planetary albedo as the forcing for the CKE parameterized cumulus and WQE system, the design of the FQ run may not be appropriate for the comparison between (FK-BK) and (FQ-BQ).

The changes from BQ to FQ and from BK to FK, however, are the same in terms of the anvil parameterization method. As a comparison, the anvil incidence decreases from 20% in BK to 8% in FK, while the cumulus incidence is unchanged. This means that the model atmosphere, with CKE parameterized cumulus, is more sensitive to external forcing. Since we do not change the constant in the fractional anvil formula, the sensitivity of the radiation field to cumulus convection is the same for FK and FQ. In other words, same amount of mass flux, from the same type of clouds, produces the same radiative effects. Keep in mind that the radiative effects of the anvils do no depend on the environment. On the other hand, the radiation change by anvils does change the environmental sounding which in turn affects the cumulus convection.

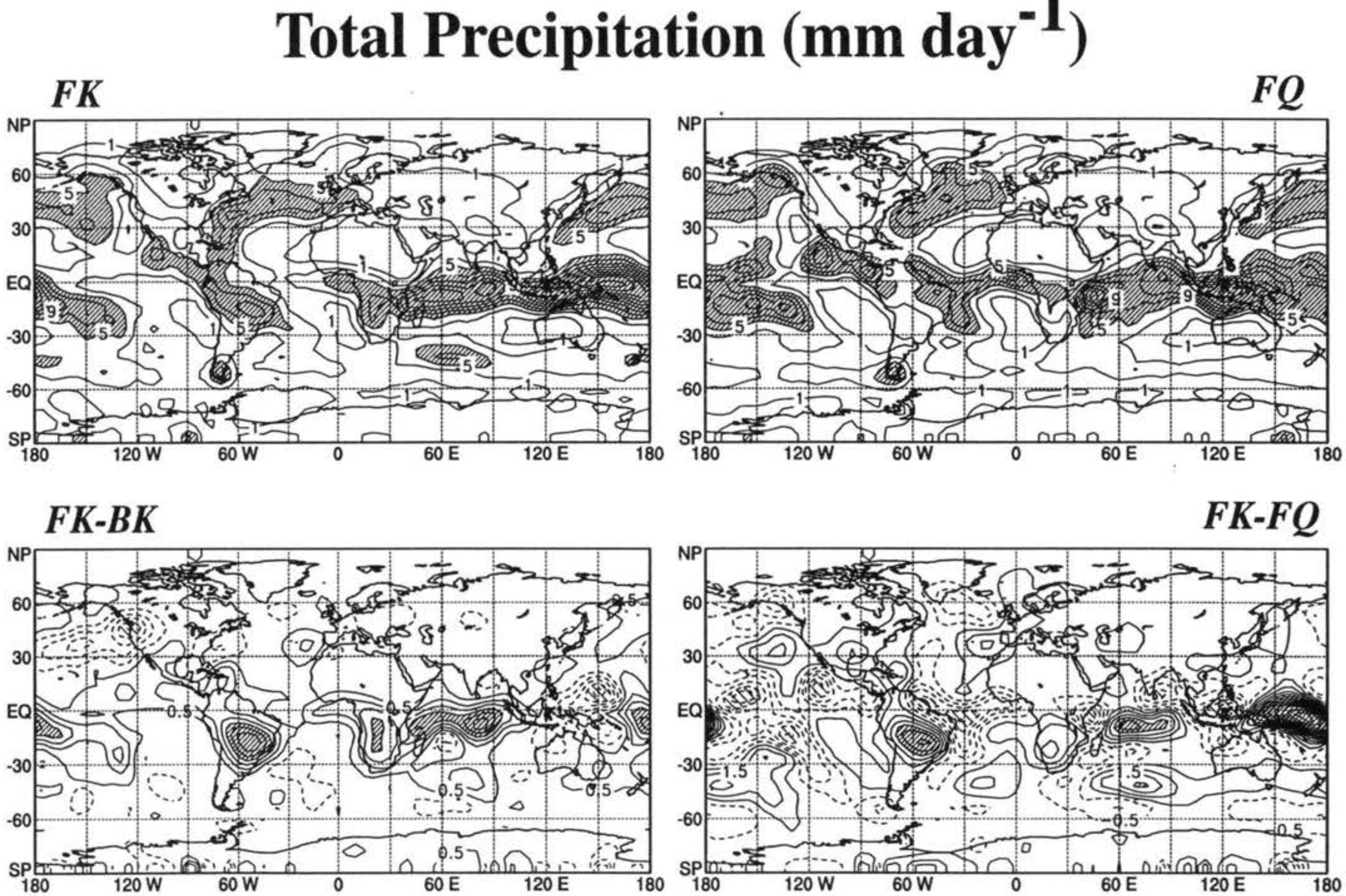

FIGURE 4.22: Total precipitation of FK and differences between FK and BK, and between FK and FQ. Intervals and shadings are the same as in Fig. 4.1.

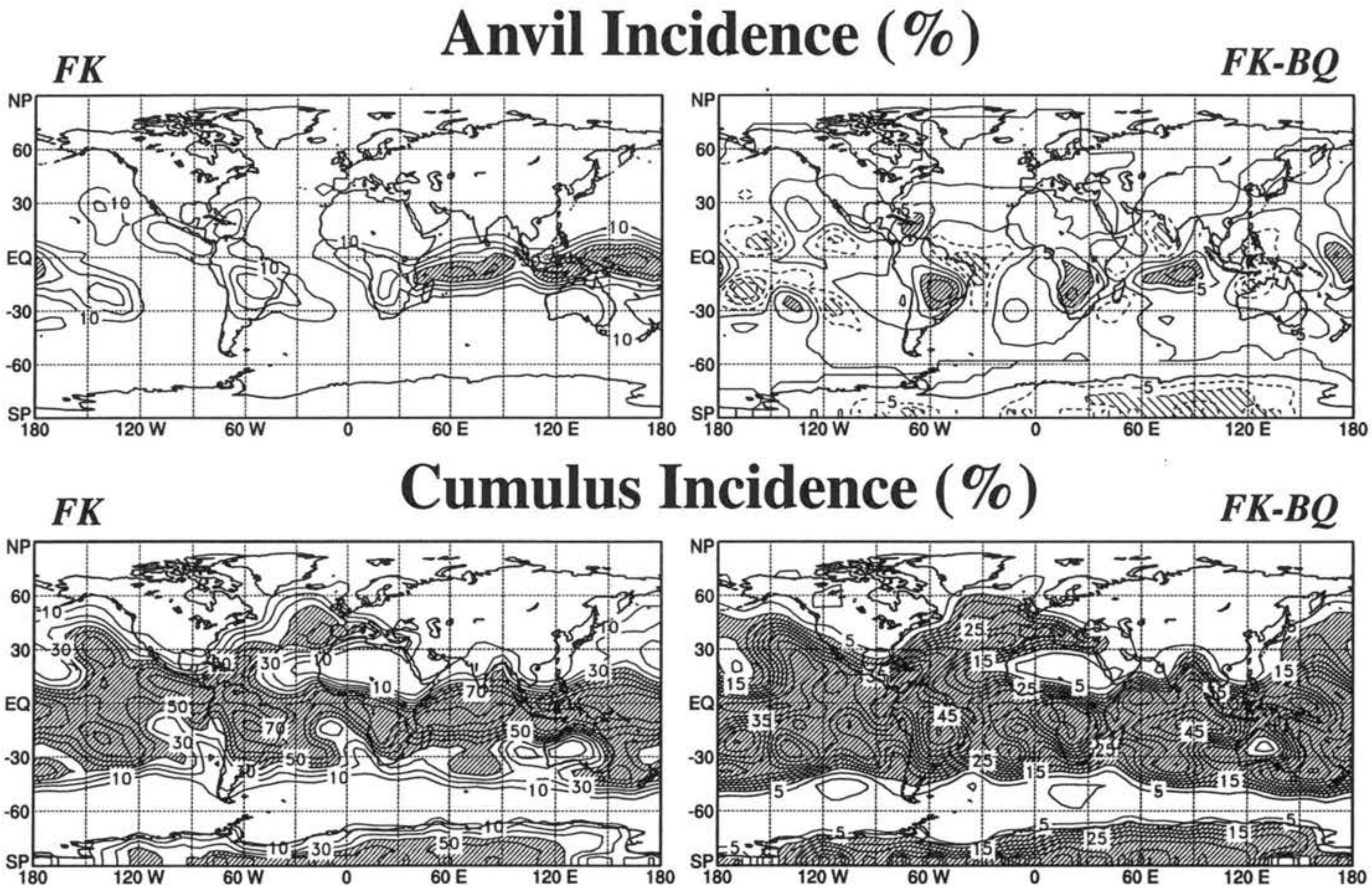

FIGURE 4.23: Anvil and cumulus incidence for FK and difference between FK and BQ (FK-BQ). For FK, interval is10%, shading is above 40%. For the difference plots, interval is 5% and shading is above 10% and below -10%.

4.2.3.2 FK versus BQ

Among the four runs, only the FK run produces maxima over the winter-hemisphere land. Fig. 4.22 compares the precipitation of FK and that of BQ. The precipitation rate from FQ is also shown. Fig. 4.23 shows the cumulus and anvil incidences comparing FK and BQ runs. FK and BQ show very similar global-mean anvil incidences but obvious changes in their distributions. The increases (from BQ to FK) in anvil incidence is apparently associated with the increases in precipitation, primarily over land.

Similar differences between FK and BQ can also be seen in Fig. 4.24 which shows cloud-base mass flux distribution for all the four runs. Only the FK run shows apparent maxima over land surfaces. We can see that the WQE parameterized cumulus clouds send much more global-mean mass flux across the PBL-top than the CKE parameterized. The WQE parameterized cumulus convection is also less organized. Relative maxima are seen in middle latitudes, especially over North Atlantic Ocean which is not seen with the CKE-parameterized cumulus convection. On the other hand, the CKE cumulus convection shows much stronger and spatially coherent maxima of the ITCZ.

Very dramatic increases appear in cumulus incidence, from BQ to FK (or BK), almost everywhere in the tropics. The maximal cloud-base mass flux over North Atlantic Ocean in the BQ run, however, corresponds to very small cumulus/anvil incidence. The cumulus/anvil incidence here with the FK (or BK) run is twice as large but associated with much smaller mass flux. Mean meridional circulation (as shown earlier) is stronger in FK than in BQ, as shown earlier.

Cloud-Base Mass Flux (mb hr^{-1})

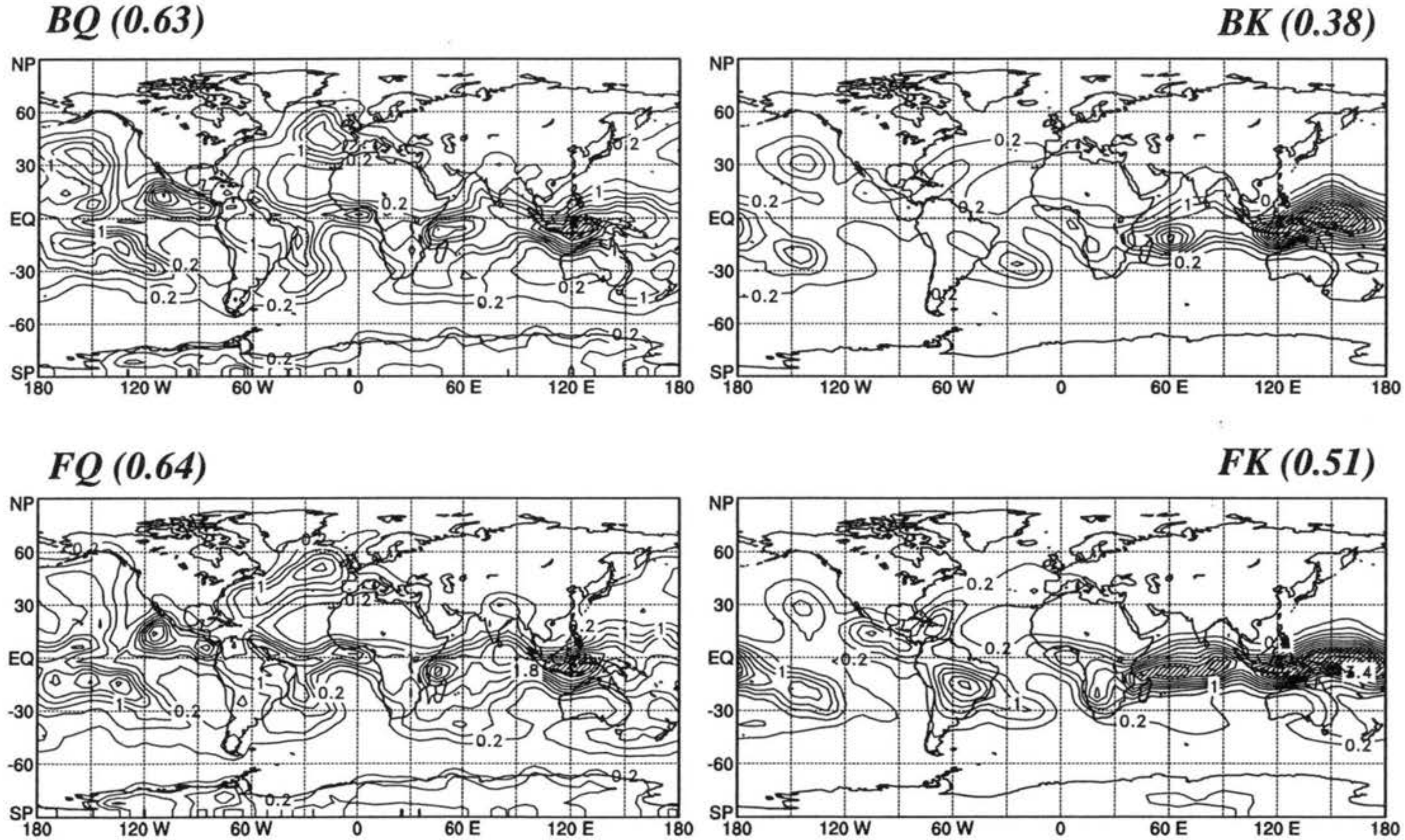

FIGURE 4.24: January-mean cloud-base mass flux for the four runs. Contour intervals are 0.4 mb hr^{-1}. Areas shaded are where mass flux exceeds 3 mb hr^{-1}. Numbers in the parentheses are global means.

The fractional anvils, in a sense, simplify the interaction among cumulus subensembles. In our simple anvil parameterization, the shallow cumulus clouds have a direct effect on the optical depth of the anvil clouds by contributing to the total cloud-base mass flux. In other words, the shallow convection can (indirectly through radiation) change the temperature and moisture field of the higher elevations where they do not reach. Therefore, via the radiative effects of the fractional anvil, shallow cumuli actually have similar effects as deep cumuli, except that the deep cumulus clouds determine the pressure depth of the anvils that the shallow cumulus clouds have no control of. Since both the effects of the anvil clouds and the deep convection are to cool at the top of the anvil clouds and warm the whole column below. Shallow convection has the ability of "suppressing" deep clouds by increasing the optical depth of the anvil clouds. However, the above are still simplified arguments. It can be more complex in the model, e.g., the anvil can cool a deeper layer than the deep cumulus clouds which only cool the layers of the cloud tops.

4.3 Comparison with Observations

In this section, we compare the results of FK and BQ with observations. We have four-year mean ECMWF observations for temperature and relative humidity, from which the specific humidity can be derived. (The effect of ice is not taken into account when calculating the saturation mixing ratio.)

Fig. 4.25 shows the differences between BQ and observations and those between FK and observations, in zonal mean temperature, relative humidity, and water vapor mixing ratio. The humidity fields above 400 mb are ignored because the observations above this

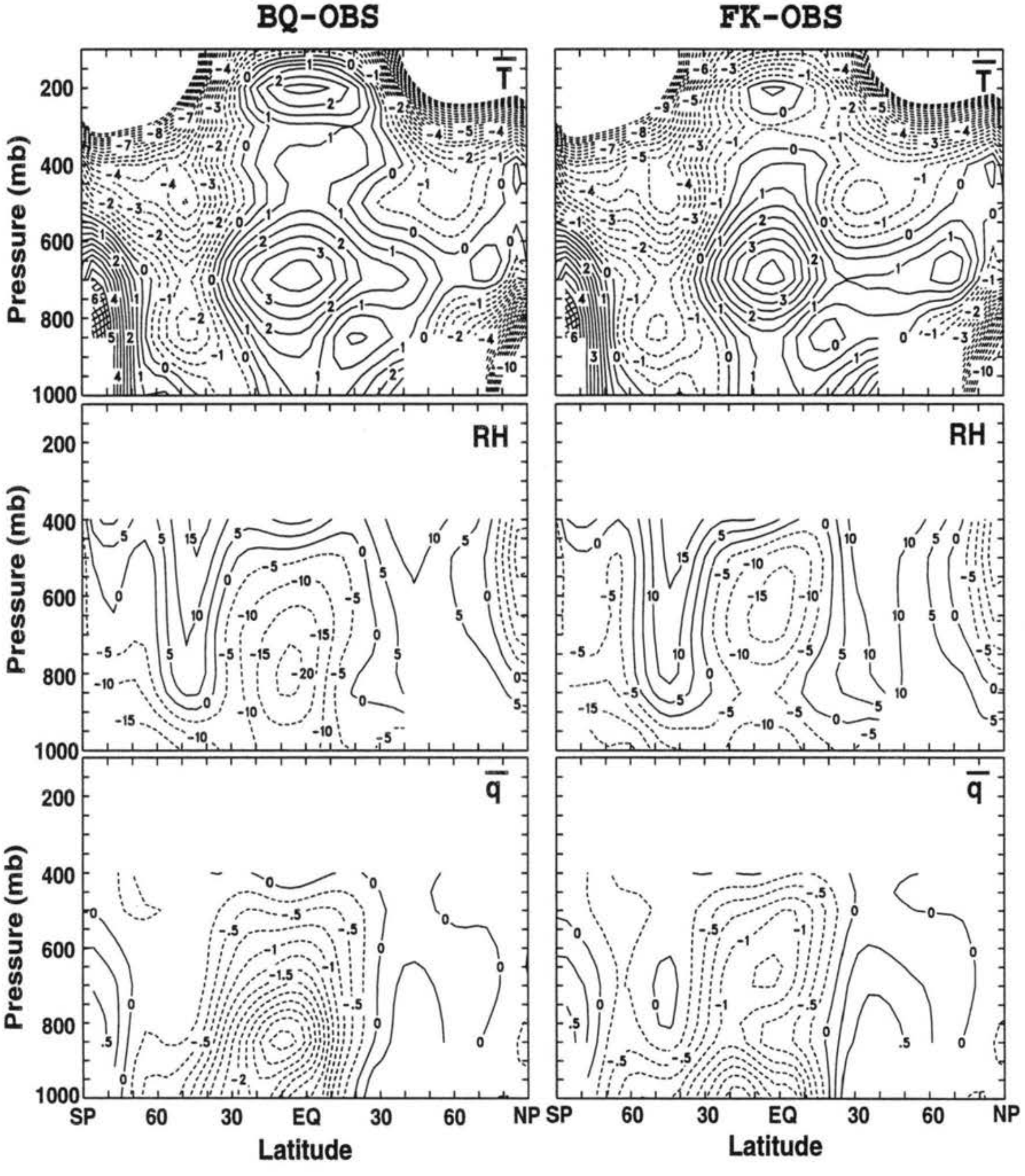

FIGURE 4.25: Difference plots showing (BQ-observation, left) and (FK10-observation) in zonally-averaged monthly-mean temperature (upper), relative humidity (middle), and mixing ratio. The contour interval for temperature (relative humidity, mixing ratio) is 0.5 K (5%, 0.25 g kg^{-1}). Moisture fields above 400 mb are omitted.

level are unreliable. The huge temperature deficits above 300 mb in middle to high latitudes are not meaningful, since the model does not resolve the stratosphere.

Compared to BQ, FK gives an improvement in the distribution of water vapor mixing ratio. The BQ run produces a very dry layer (as much as 3 g kg^{-1} lower than observed) at 850 mb in the tropics. This moisture deficit is reduced to 1 g kg^{-1} in the FK run. Compared to observations, BQ is too warm all through the tropical troposphere. FK produces more realistic temperature between 500 mb and 200 mb, but is slightly warmer in the middle troposphere between 800 and 500 mb. FK has a colder atmosphere above 200 mb. Relative humidity is better between 850 and 700 mb, but not as good at 500 mb and 400 mb.

4.4 Summary and Discussion

In this chapter, we describe tests of the prognostic CKE method in the CSU GCM. Results were compared with those from the cloud work function quasi-equilibrium. Through the comparison, we examine the interactions among cumulus convection, radiation, and large-scale dynamics. These interactions cannot be seen in our preceeding 1-D experiments.

The CSU GCM originally used a very simple "binary anvil" parameterization to represent the cloud-radiation interactions, in which the "anvils" either cover the whole grid box or do not exist at all. With this unrealistic way of representing anvil clouds, anvils (deep cumulus clouds) seldom occur. The simulated January-mean tropical OLR is also lower than the observed. When we replace the cloud work function quasi-equilibrium with the CKE approach in the cumulus parameterization, dramatic changes occur in the anvil incidence and the tropical OLR is further reduced. This suggests the need for a better way of representing the anvil-radiation processes.

To make the “anvil clouds” more realistic, we allow their “fractional coverage.” The optical depth of the fractional anvils is assumed proportional to the total cloud-base mass flux of the cumulus convection. This more directly links the cumulus activity to the radiation field and large-scale dynamics. The January climate is reasonably well reproduced, with the CKE parameterized cumulus clouds and the fractional anvils.

Combination of the CKE method with fractional anvils produces better results than the cloud work function quasi-equilibrium with binary anvils. The January precipitation rate over land improves. Cumulus convection occurs more more often almost anywhere in the tropics.

The decrease of the optical depth of anvil clouds suppresses convection. Since the cloud radiative forcing by the anvil clouds is usually a deep warming through the troposphere, the warming intensifies the upward branch of the Hadley circulation which in turn promotes deep convection (Randall *et al.*, 1989). The effects of the cloud radiative forcing in the “Seaworld” experiments of Randall *et al.*(1989) are the reduction of cumulus incidence and the increase of the global mean precipitation. The fractional anvils result in optically thinner anvil clouds. The smaller monthly-mean anvil optical depth is mainly due to the smaller anvil incidence. The optically thinner anvil from the fractional anvil, however, corresponds to a larger global mean precipitation. A large part of the precipitation increase comes from the land surfaces where the increased solar-radiation absorption promotes convection.

We define the anvil clouds whenever a deep cumulus cloud penetrates above 500 mb. With the binary anvils, deep cumulus convection interacts with the radiation by anvil incidence. For that reason, the more often the deep cumulus convection occurs, the less the latent heating (which also includes the contribution from shallow clouds) is needed to balance the radiative cooling. This also affects the intensity of the mean meridional circulation. On the other hand, with the fractional anvils, deep cumulus convection can occur frequently with each deep cumulus carrying little mass flux, if the global radiation budget is to remain the same. The little mass flux with deep cumulus clouds makes an easier environment for shallower clouds.

The zonal-mean anvil and cumulus incidences suggest that the fractional anvils help the shallow convection. Since we allow the shallow cumulus clouds to contribute to the change of the optical depth of the anvil clouds, they can directly affect the whole depth of the atmosphere through radiation while they do not contribute to heating/moistening in the upper levels through latent heating. The increased optical depth of the anvil clouds suppresses convection (if large-scale vertical motion is not taken into account). Since the cloud radiative forcing by the anvil clouds is usually a deep warming through the troposphere, it especially suppresses the deep convection. Therefore, via the radiative effects of the fractional anvil, shallow clouds actually have the function of suppressing deep clouds.

In the 1-D experiments discussed in the preceding chapter, no interactive radiation was used. We used either a constant 2 K day^{-1} cooling or, for the GATE simulation, the observed total radiative heating rate. The cumulus clouds could not change the radiative heating rate in these experiments. However, as we have discussed, cumulus convection is closely related to the existence of radiatively important stratiform clouds. The distributions of radiative and cumulus heating strongly affect the atmospheric general circulation. The general circulation determines the "large-scale forcing" for the cumulus convection, while the cumulus convection changes the environment and the general circulation.

In the model with binary anvils, deep cumulus clouds can change the radiation field by creating the optically thick anvil clouds while shallow clouds do not have any effect on the radiation field. Therefore, only the deep clouds have direct effects on the large-scale forcing (on all cumulus subensembles). Shallow clouds can only interact with other cumulus subensembles by indirectly modifying the environment, i.e. through the kernels. Deep clouds can affect shallow clouds not only through the kernels but also by changing the large-scale forcing for shallow clouds. Should this part also be included in the kernels? This seems to show that the difference between the large-scale forcing and the kernel is clearly defined.

In a way, LSP suppresses shallow convection. From our 2 K day^{-1} cooling experiment, the cumulus heating profile is mainly determined by the evaporation of LSP in the middle to low levels. When there is no LSP evaporation, the cumulus heating is a uniform 2 K day^{-1} vertically. When there is no LSP evaporation, the only moisture source for the middle layers is the detrainment from shallow clouds. When there is LSP evaporation, detrainment from shallow clouds is not necessary. On the other hand, the evaporative cooling needs to be balanced by cumulus heating of deep convection.

Why is the LSP weaker or the shallow cumulus convection stronger in the control run? The LSP suppresses shallow convection while it owes its existence to deep convection. We can say that the LSP is the medium through which the deep cumulus clouds interact with (suppresses) the shallow cumulus clouds. The interaction among cumulus subensembles is represented in terms of kernels in the quasi-equilibrium of cloud work function. On the other hand, the LSP is really a large-scale process.

In the control run, shallow cumulus clouds seldom occur. However, they detrain much more mass when they occur, compared to the shallow clouds per incidence in the CKE run. As a result, the BK run shows more heating between 850 mb and 600 mb. The LSP heating (cooling) is stronger in the BK run above 500 mb. This agrees with the above discussion that the LSP suppresses shallow convection.

The methods are so different that we do not calculate kernels and the large-scale forcing at all in our method. However, although we do not define the large-scale forcing, the large-scale processes still promote cumulus convection. Although we do not calculate the kernels, the cumulus subensembles still interact with each other by modifying their shared environment. The way the cumulus clouds modify the environment is unchanged in our method. However, we do modify the way the large-scale processes promote the cumulus convection. Clouds are not asked to follow a cloud work function quasi-equilibrium as strictly.

CHAPTER 5

The Cloud Spectral Parameter

When dealing with the cumulus parameterization problem, we treat cumulus clouds as an ensemble. In a cumulus ensemble, clouds of different depths can co-exist. They modify their common environment in different ways. Deep cumulus clouds moisten the high levels and warm the whole column below, while shallow cumulus clouds moisten the middle to low levels. Therefore, we need to divide the ensemble into sub-ensembles. The question is: How should we define the sub-ensembles?

The noise that occurs in our 1-D experiments (Chapter 3) indicates a drawback of Lord *et al.* (1982)'s method to define the cloud type in a numerical model. In this chapter, we shall discuss this problem and try to develop an alternative cloud spectral parameter that can improve the numerical behavior of the simulated cumulus convection. Since the cumulus parameterization should be based on the physics of cumulus convection, studies of individual cumulus clouds should be the starting point of the cumulus parameterization problem. For that reason, we first review studies on individual convective clouds and try to demonstrate the physical merits of our approach over the original method of Lord.

5.1 Review of Studies on Convective Motions

5.1.1 Simple Parcel Theory

Usually, we judge the presence of moist convective instability by looking at the environmental sounding. Given vertical profiles of temperature and water vapor mixing ratio, we lift an air parcel along an adiabat to its LCL (lifting condensation level) where the parcel saturates. If the parcel conserves water vapor on the way up, the mixing ratio of the parcel will increase because of the decrease of the temperature and will eventually saturate. The environment is said to have conditional instability if the air parcel has positive buoyancy above the LCL. The non-entraining saturated air parcel then follows a moist adiabat upward until it reaches its level of neutral buoyancy. However, the buoyancy derived from this simple parcel theory often exceeds that from the observations (Bunker *et al.*, 1949).

In reality, clouds mix with environmental air as a result of the turbulence on their edges. This turbulent mixing, also known as entrainment, dilutes the buoyancy of the clouds and is an important process in convective motions. Many efforts have been made to obtain an entrainment relationship for cloud models, which we briefly discuss as follows.

5.1.2 Entrainment in Thermals and Plumes

Many studies on entrainment in cumulus clouds were published in late 1940's and 1950's. These studies often used plumes or thermals in the laboratory experiments to study the entrainment in convective motions, assuming that the convection in the atmosphere is a similar process. The plumes or thermals were assumed to conserve their total buoyancy, vertical momentum and mass when rising (sinking) through the environment (Ludlam, 1980). Due to entrainment, the plumes or thermals expand as they travel. These experimenters tried to formulate a relation between the rising speed of the buoyant air and the depth of the convection. The rising speed was often assumed to be proportional to the speed of the inflow from the environment into the plume, i.e., the entrainment rate.

Stommel (1947, 1951) deduced the entrainment rate in real clouds by using the observed in-cloud and environmental soundings. He considered the clouds to be steady jets. Batchelor (1954) used simple dimensional analysis to obtain a relation between the radius of the plume cap and the distance the cap traveled (equivalent to the depth of the convection). He also derived the rising speed in terms of the radius and the depth. Scorer (1957) performed a laboratory experiment to obtain the constants in the relations mentioned above. He also concluded that the Froude number (the ratio between inertial forces and buoyancy) in his laboratory experiment is comparable with that of convection in the atmosphere, so the constants he got can be applied to the atmospheric convection problem. Ogura (1962) did a numerical calculation, releasing a thermal in an incompressible fluid. He further confirmed the constants from the laboratory experiments, and the dimensional analysis. Levine (1959) treated the cumulus as a rising bubble, and found the relation that the entrainment rate is inversely proportional to the radius of the bubble. Simpson and Wiggert (1969) applied this relation in their cumulus cloud model.

With the constants given from the laboratory experiments, the rising speed and expansion rate of the thermal starting from the "virtual origin" can be predicted, given the densities of the environment and the thermal. This implies that entrainment rate is an inherent and *independent* property of the thermal, determined at its "virtual origin." This property of the thermal does not change with time or along its path of travel, and hence is a good identifier for a thermal.

5.2 The Cloud Spectral Parameter in Cumulus Parameterization

In cloud dynamics, only individual clouds are considered. We discuss how a single cumulus cloud can grow and dissipate in an environment and how the entrainment affects the clouds. In cumulus parameterization, an ensemble of clouds is considered. We need to understand not only how the environment allows the cumulus clouds to exist, but also the collective effects of the clouds on the environment. The cloud dynamics must be simplified before it can be applied to the cumulus parameterization problem. The effects of entrainment must be considered and represented in a statistical way.

Arakawa and Schubert (1974) used λ to define the cumulus subensemble, or the cloud "type." They assumed that each cumulus subensemble can be characterized by a normalized vertical profile of the mass flux. This normalized mass flux distribution is interpreted to be the time-average over the life time of that cloud subensemble. It is entirely determined by the value of λ, which is assumed to be independent of height. The assumption of λ constant with height is consistent with the laboratory studies of plumes discussed earlier.

Since entrainment reduces clouds' buoyancy, subensembles with larger λ's lose buoyancy faster than those with smaller λ's. Therefore, there is a one-to-one correspondence between the fractional entrainment rate and the cloud-top height of the subensemble. For a given sounding, defining cumulus subensembles by λ is equivalent to defining them by the height at which they detrain. For a given λ, the clouds might stop at any height between the vertical grid levels of a model. This makes the integration to determine the in-cloud sounding and cloud work function more complex. For this reason, Lord (1980) chose the detrainment level itself, $\hat{p}$, instead of λ, as the independent cloud spectral parameter. Lord essentially still used λ as the cloud spectral parameter, but his λ is a function of $\hat{p}$, i.e., $\lambda = \lambda(\hat{p})$ where $\hat{p}$ is an independent variable. However, the relation between λ and $\hat{p}$ depends on the environmental sounding, and λ is a derived quantity.

We discuss and compare using λ or $\hat{p}$ as the independent variable representing the cloud spectral parameter in more detail in the following sub-sections.

5.2.1 Using the Detrainment-Level Pressure $\hat{p}$ — Lord's Approach

Lord and Arakawa (1980) and Lord *et. al.* (1982) forced clouds to lose buoyancy at discrete model levels, and in that way obtain a λ for each cloud subensemble. In other words, they used the pressure level where the clouds detrain, $\hat{p}$, to define the subensembles. Given an initial guess of λ, we can calculate the normalized mass flux for each sub-ensemble, $\eta(\lambda,p)$, using

$$\rho g \frac{\partial}{\partial p}\eta(\lambda, p) = -\lambda\eta(\lambda, p) . \tag{5.1}$$

The in-cloud profile of moist static energy can then be obtained using

$$-\rho g \frac{\partial}{\partial p}([\eta(\lambda, p) h_c(\lambda, p)]) = \lambda\eta(\lambda, p)\bar{h}(p) . \tag{5.2}$$

The buoyancy at a pressure level, $B(\lambda,p)$, is approximately given by

$$C_p B(\lambda, p) = h_c(\lambda, p) - \hat{h}^*(p) , \tag{5.3}$$

where $\hat{h}^*$ is defined as

$$\hat{h}^* \equiv \bar{h}^* - \frac{(1+\gamma) L\varepsilon}{1+\gamma\varepsilon\delta}[\delta(\bar{q}^* - \bar{q}) - \hat{l}] . \tag{5.4}$$

Eq. (5.3) was derived by Arakawa and Schubert (1974), assuming that ice is not present. Here γ is defined as

$$\gamma \equiv \frac{L}{C_p}\left(\frac{\partial \bar{q}^*}{\partial \bar{T}}\right)_{\bar{p}} . \tag{5.5}$$

Other symbols are: $\delta = 0.608$, $\varepsilon \equiv C_p\bar{T}/L$, and $\hat{l}(z)$ is the liquid water mixing ratio at the level of vanishing buoyancy. Given a detrainment pressure level $\hat{p}$, we can find a λ that satisfies

$$B(\lambda, p_D) \approx 0, \tag{5.6}$$

by iterating (5.1), (5.2), and (5.3).

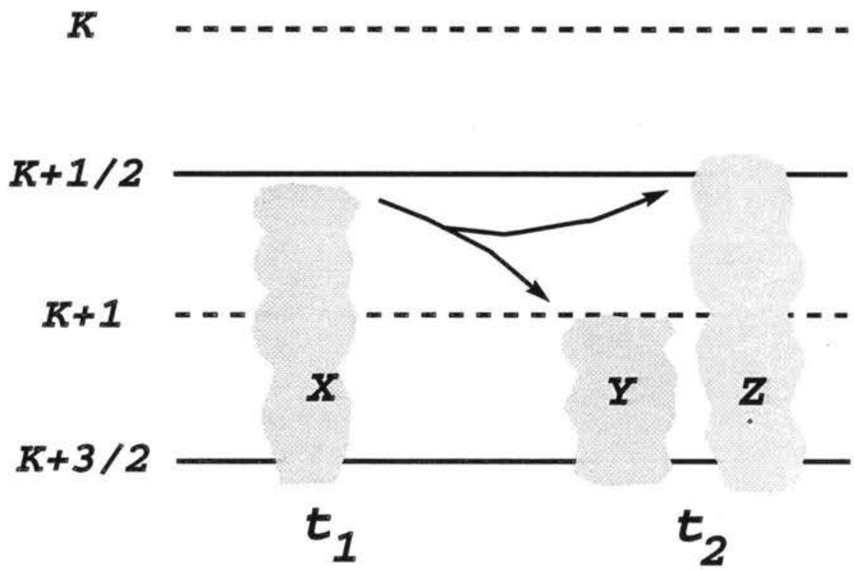

FIGURE 5.1: Schematic plot showing the sudden appearance of cloud type Z, from time t_1 to time t_2. Integer levels (dashed lines) are layer centers, otherwise edges, following Lord's approach.

Lord (1978) defined cloud types by the indices of the GCM layers, as illustrated in Fig. 5.1. If the tallest cloud possible is cloud *Z*, all other shallower clouds detrain in layer centers. For example, the cloud *Y* detrains at level *K+1* and is labeled "type *K+1*." We then determine the fractional entrainment rate for the cloud that loses buoyancy at the level, λ_{K+1}.

All cumulus clouds originate from the PBL and carry the moist static energy and water vapor mixing ratio of the mixed layer. The moist static energy in the clouds can be obtained directly by mixing the upcoming air (parcel) with the environment using the fractional entrainment rate. The mixing ratio of liquid water is calculated using the diluted moist static energy, assuming that the in-cloud air is saturated with respect to water or ice. Ice can be carried by the updraft as well as entrained from the environment, and additional ice formation is calculated according to the cloud temperature.

The ideas discussed above apply to clouds that can exist (but are not necessarily active), given the sounding of the environment. With the sounding, we can determine the highest pressure level the cumulus clouds can reach, with a fractional entrainment rate $\lambda \geq 0$. For each family of cumulus clouds that can lose buoyancy at the various model levels, a fractional entrainment rate is obtained. The cumulus clouds affect the environment only up to the layer where they detrain. The environmental effects of the tallest possible clouds (the non-entraining clouds), however, have to be calculated separately, because they usually lose their buoyancy between the discrete model levels.

Note that the fractional entrainment rate of the tallest cloud type in Lord's approach usually is not exactly zero. The height of the tallest cloud top (just like the tops of the shallower clouds — on model levels) is determined before the cloud liquid water and hence the exact buoyancy is known. We can re-write (5.4) as

$$\hat{h}^* \equiv \hat{h}^{\circ} + \frac{(1+\gamma)\,L\varepsilon}{1+\gamma\varepsilon\delta}\,\hat{l}, \tag{5.7}$$

where $\overset{\circ}{\hat{h}}$ is the part of $\hat{h}^*$ that comes solely from the environment and is used to determine the tallest cloud top. Since $\hat{h}^* \geq \overset{\circ}{\hat{h}}$, Lord's non-entraining clouds lose buoyancy a little earlier than the real non-entraining clouds and have λ slightly larger than zero.

5.2.1.1 The Tallest Cloud Type

Lord (1978) assumed that all clouds (other than the tallest) detrain at integer levels (e.g. level $K+1$, i.e. the center of layer $K+1$ in Fig. 5.1), since the effects of cumulus convection on the environment are only calculated at the layer centers. With this approach, clouds cannot be felt by the environment in layer K until the cloud tops reach level K, even if the $\lambda \sim 0$ clouds penetrate through level $K+1/2$ into layer K. This is the case for the cloud Z in Fig. 5.1. Cloud Z that detrains slightly below the center of layer K (between levels K and $K+1/2$) can "exist" with a positive or zero entrainment rate, but they do not have any effect until they penetrate level K. However, these clouds do not exist (affect the environment) only because the resolution of the model is too coarse. The sudden appearance of these clouds at level K, due to a small change in the sounding, will cause a discontinuous change in the convective heating and drying rates, due to the accumulation of the "energy" that would have been released if the model had finer vertical resolution. This situation is reflected in the results as noise. Lord (1978) dealt with this problem by weighing the cumulus effects on the detrainment layer by the proportion of the penetration into this layer:

$$\frac{h_M - \bar{h}^*_{k+1/2}}{\bar{h}^*_{k-1/2} - \bar{h}^*_{k+1/2}}. \tag{5.8}$$

Since we have associated the cloud type with the "index" of a GCM layer (such as $K+1$) when any clouds that have $\lambda \geq 0$ and detrain *anywhere* in that layer, there will always be a moment when a cloud type in this sense "suddenly" emerges. The numerical problems that occur when clouds cross level $K+1$ have been discussed above. On the other hand, does the sudden appearance of a cloud type also cause numerical problem? If so, this problem is different from the noise problem dealt with by Lord (1978) discussed above.

5.2.1.2 Noise Problem with the Prognostic CKE

When the tallest clouds penetrate into (retreat from) a layer, it corresponds to the sudden appearance (disappearance) of a whole subensemble. This can be illustrated again using the example in Fig. 5.1. At time $t = t_1$, the tallest (non-entraining) cloud type is type X. At the next timestep, $t = t_2$, the non-entraining clouds barely penetrate into layer K and hence define a taller cloud type, Z. Therefore, there are now two types of clouds that reach above level $K + \frac{3}{2}$ and can modify the environment of this layer.

In the CKE approach, the steady-state solution of (3.3) can be written as

$$M_B = \frac{\tau_D}{\alpha} A. \tag{5.9}$$

This equation closely holds for each type of clouds almost all the time, because the time step we use (1 hr) is much longer than τ_D. Suppose that at $t = t_1$, the tallest cloud type, detraining in layer $K+1$, has fractional entrainment rate λ_{K+1}. At the next time step, $t = t_1 + \Delta t = t_2$, a slightly taller cloud penetrates into the next higher layer, K, and has $\lambda_K \sim \lambda_{K+1}$. We expect that $A(\lambda_K) \sim A(\lambda_{K+1})$, and so from (5.9), $M_B(\lambda_K) \sim M_B(\lambda_{K+1})$. When using the CKE approach, however, both types of clouds co-exist at the moment the clouds penetrate into layer K, and both satisfy (5.9). It is as if clouds of a similar entrainment rate (or that detrain at similar heights) suddenly have their mass flux doubled. It takes the model some time to digest this pulse. This results in temporal noise. The degree of this noise can depend on α, according to (5.9). Using a larger α can reduce the noise, but does not really solve the problem.

The situation is different with the approach of cloud work function quasi-equilibrium, in which the existence of a cloud type is immediately (at the same timestep) realized by the other types of clouds. (This is comparable to an implicit numerical scheme.) For this reason, the major effect of the sudden appearance of a cloud type is seen only locally in the new cloud-top layer. Lord's special treatment was thus able to suppress the noise.

The sudden appearance/disappearance of the deepest cumulus subensemble affects the entire atmospheric column (layer K and all the layers below, in the above example). For that reason, the special treatment of the highest cloud-top by Lord (1978) cannot remove the noise. To solve the noise problem, we have to define the cumulus subensembles in a different way. With this new approach to defining cloud type, the effects of the deepest clouds on lower levels should be continuous with time when the cloud tops cross model levels.

5.2.2 Quasi-Equilibrium in Terms of Detrainment Pressure

Other than the numerical problems discussed above, using detrainment-level pressure to define cumulus subensemble may also alter the cloud work function quasi-equilibrium which was originally posed using λ as the spectral parameter. The time derivative of cloud work function as a function of the detrainment-layer pressure, $\hat{p}$, can be divided into two parts:

$$\begin{aligned}\frac{\partial}{\partial t}A(\hat{p}) &= \underline{\left[\frac{\partial}{\partial t}A(\hat{p})\right]_{Cu} + \left[\frac{\partial}{\partial t}A(\hat{p})\right]_{LS}} \\ &= \left\{\left[\frac{\partial}{\partial t}A(\hat{p})\right]_{Cu} + \left[\frac{\partial}{\partial t}A(\hat{p})\right]_{LS}\right\}_{\lambda = constant} \\ &\quad + \frac{\partial}{\partial \lambda}A(\hat{p})\left[\left(\frac{\partial \lambda}{\partial t}\right)_{Cu} + \left(\frac{\partial \lambda}{\partial t}\right)_{LS}\right].\end{aligned} \tag{5.10}$$

Here the subscripts "*LS*" and "*Cu*" denote the contributions from large-scale forcing and cumulus convection, respectively. The term in the braces ({ }) should vanish under the assumption of cloud work function quasi-equilibrium by Arakawa and Schubert (1974). On the other hand, the quasi-equilibrium in Lord's approach requires instead the underscored terms to balance each other, i.e.

$$\left[\frac{\partial}{\partial t}A(\hat{p})\right]_{Cu} + \left[\frac{\partial}{\partial t}A(\hat{p})\right]_{LS} \approx 0. \tag{5.11}$$

These two terms are calculated separately. The second term is the large-scale forcing $F(\hat{p})$ and is determined by

$$F(\hat{p}) = \frac{A'(\hat{p}) - A(\hat{p})}{\Delta t'}, \tag{5.12}$$

where $A'(\hat{p})$ is the cloud work function after the large-scale processes have modified the sounding in the period of time $\Delta t'$. The first term includes the kernels $\mathrm{K}(\hat{p}, \hat{p}')$ obtained by

$$\mathrm{K}(\hat{p}, \hat{p}') = \frac{A''(\hat{p}) - A(\hat{p})}{m_B(\hat{p}')\,\Delta t''}, \tag{5.13}$$

where $A''(\hat{p})$ is the cloud work function after the modification of the environment by the other cloud type ($\hat{p}'$), in a very short time $\Delta t''$. $m_B(\hat{p}')$ is a small trial mass flux chosen arbitrarily. It was shown by So (1982) using mid-latitude data that the kernel obtained from (5.13) does depend on the value chosen for $m_B(\hat{p}')$. Both (5.12) and (5.13) ignore the change in the fractional entrainment rate from $A(\hat{p})$ to $A'(\hat{p})$ or $A''(\hat{p})$, i.e. the two terms after the braces in (5.10). These two terms represent the difference between the original cloud work function quasi-equilibrium and Lord's approach.

Kao and Ogura (1987) used GATE data to estimate these terms. They found that for the middle clouds, the change of λ (which is no longer an independent variable) usually reduces the large-scale forcing and sometimes even makes the large-scale forcing negative. This is because the strong middle-layer vertical rising motion is not allowed to deep-en the cumulus clouds (through the large-scale forcing), when $\hat{p}$ is used to define the cumulus subensemble.

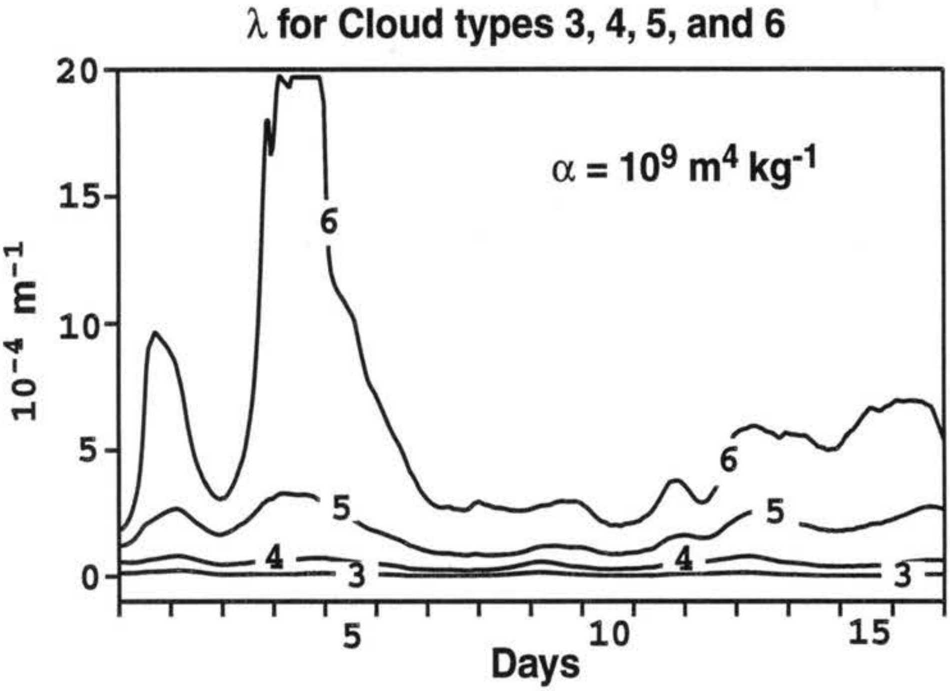

FIGURE 5.2: Fractional entrainment rates for cloud type 3, 4, 5, and 6 in the GATE simulation using Lord's approach. $\alpha = 10^9\ m^4\ kg^{-1}$ has been used.

The difference between Lord's approach and the original cloud work function equilibrium, as seen in (5.10), involves the time rate of change of λ. Fig. 5.2 shows the calculated fractional entrainment rates for cloud type 3, 4, 5, and 6 as a function of time, from the GATE simulation discussed in Chapter 3. The variation of λ with time is significant, especially for the shallower (middle) clouds, types 5 and 6. (The shallowest and deepest clouds are not shown in the figure because they do not exist continuously in time.) The variation of the entrainment rates is generally in phase with that of the precipitation rate (or the large-scale forcing). From Fig. 5.2, we can also see that $\Delta\lambda = 10^{-5}\ \mathrm{m}^{-1}$ is small enough to resolve all the cumulus clouds in this case and with this particular vertical resolution. Tests show that λ is much smaller when $\alpha = 10^{8}\ \mathrm{m}^{4}\ \mathrm{kg}^{-1}$ is used (not shown), and its variation with time is much stronger.

5.2.3 Using λ as the Independent Cloud Spectral Parameter

The iteration using Eqs (5.1) to (5.6) is done for each subensemble at every time-step in Lord's method, so the entrainment rate for a cloud "type" varies with time, as shown above. According to our discussion in the preceding section, however, the entrainment rate is itself a good identifier of cloud type. Furthermore, since the original A-S parameterization uses λ to define cumulus subensembles, an obvious approach is to do the same in numerical models. Unlike Lord (1982) who calculated λ, we make λ an independent variable. As with all other independent variables, we need to find the meaningful range of λ, and to discretize λ with a resolution that can represent the physics.

The reason we can treat λ as an independent variable is that we can choose a range of λ that spans the whole "spectrum" of clouds that can exist under any large-scale situation. We assume that the cumulus parameterization itself can choose to activate or de-activate a cloud type. By choosing a sufficient range of λ and a sufficiently fine resolution in λ-space, we make "enough" cloud types available. By making clouds available to detrain in any layer of the model, we make sure that the model has enough degrees of freedom to perform at least as well as with Lord's method.

When we use the fractional entrainment rate, λ, as the cloud spectral parameter, and treat λ as an independent variable that does not vary with time, clouds with the same λ can detrain in different layers at different times. In other words, a group of clouds with a certain fixed λ can "grow" or "decay" in depth. This makes this approach seem more dynamical than the fixed-$\hat{p}$ approach. For convenience of discussion, and to avoid confusion, we call the cloud type defined by Lord (according to model layers) an "L-type" and the type defined by constant λ a "λ-type".

5.2.4 Method

We define cumulus subensembles with assigned values of $\lambda = \lambda_n$, $n = 1, 2, ...,N$. Let the deepest cumulus clouds have a fractional entrainment rate $\lambda_1 = 0$, and the shallower cumulus subensembles have $\lambda_n = \lambda_{n-1} + \Delta\lambda$, $n > 1$. We shall find values of N and $\Delta\lambda$ that can be used for a wide variety of situations. Once we have a λ for each subensemble, we can calculate the in-cloud soundings using (5.1) and (5.2), and hence the buoyancy at each model level. The buoyancy is positive below cloud top and negative above. The cloud top is defined as the height of zero buoyancy and hence can be obtained by interpolation; no iteration is needed. Computationally, interpolation is much simpler and cheaper than iteration, because we only use (5.1), (5.2), and (5.3) once for each cloud type on each timestep.

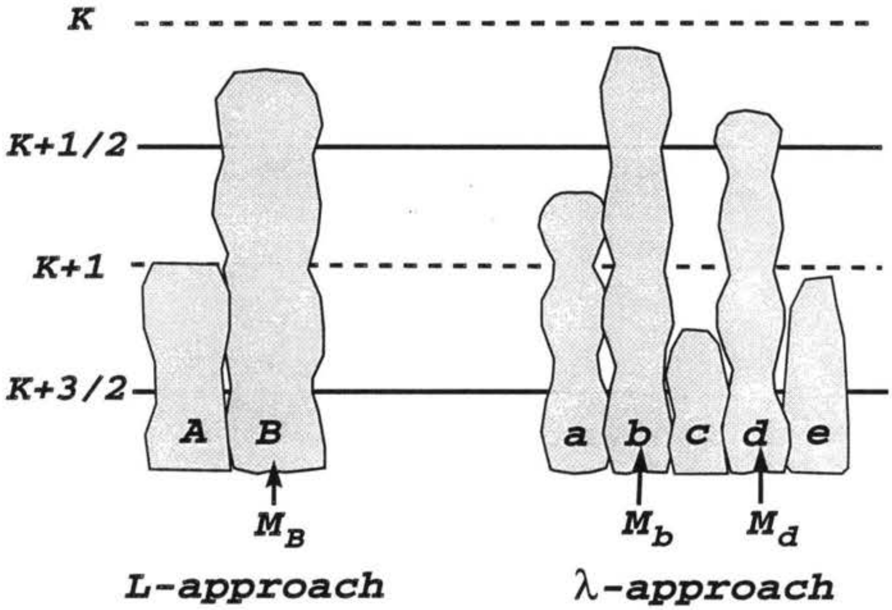

FIGURE 5.3: Schematic plot comparing the steady state of the L-approach with that of the λ-approach. Two L-types (A and B) and five λ-types of clouds (a, b, c, d, and e) exist in the example. The levels below K+3/2 are omitted. The cloud-base mass fluxes of clouds B, b, and d are M_B, M_b, and M_d, respectively.

For consistency of the numerical method, our solution should converge (to the true solution) when $\Delta\lambda \to 0$. Even if this is true, we cannot use an infinitesimally small $\Delta\lambda$ in the actual calculation. Therefore, we need to find a "sufficiently small" $\Delta\lambda$. This "sufficiently small" $\Delta\lambda$ should satisfy the condition that at least one cloud detraining in each layer of the model. In other words, $\Delta\lambda$ should be related to Δz. We shall try to derive this relation in the next section.

When $\Delta\lambda$ is too large relative to Δz, there can be some layers in which no clouds detrain. In those layers, convection can only cause warming and drying. If there is no other mechanism, e.g. LSP, to moisten, this layer will become drier and drier. Even if LSP can provide the needed moistening in those layers, it re-distributes static and latent energy in a different manner than the cumulus clouds. There is no obvious reason that the combined effects of the cumulus and LSP will converge when $\Delta\lambda \to 0$. It is therefore reasonable to require cumulus detrainment in every layer. On the other hand, when $\Delta\lambda$ is small enough, there can be many clouds that detrain in one layer.

For $\Delta\lambda$ to be small enough so that each layer has at least one detraining cloud, we must allow the possibility that multiple types of clouds detrain in one layer. This situation is illustrated in Fig. 5.3 which shows an example of the two different approaches. The sketch for the L-approach shows two different L-clouds (A and B) detraining in two different model layers (K and $K+1$), respectively. On the other hand, there are five λ-clouds detraining in the two layers: clouds b and d in layer K, and clouds a, c, and e in layer $K+1$. Then in passing from the L-approach to the λ-approach, we essentially divide one L-cloud into several sub-groups, when there are several λ-clouds detraining in the same model layer. In the above example, the L-cloud B is recognized as two λ-clouds: b and d, and the L-cloud A is seen as 3 λ-clouds: a, c, and e.

Apparently in the above example (Fig. 5.3), the number of λ-clouds detraining in one layer depends not only on $\Delta\lambda$ but also on Δz. Although we allow more than one type of clouds to detrain in one model layer, when cumulus subensembles interact with one another (by modifying their common environment), the clouds that detrain in the same layer are considered as the same type by the coarsely-resolved environment, which is resolved by the vertical grid of the model. In other words, these clouds, although given different entrainment rates, are recognized as belonging to one subensemble by the environment. The cloud work function is defined with respect to cloud subensembles. However, different cloud types defined by λ are recognized as one by the environment due to the limited vertical resolution. This will be further discussed later.

5.2.4.1 α as a function of $\Delta\lambda$

Assume that M_B is the true solution and the total cloud-base mass flux of N λ-clouds that detrain in a certain layer, and each of these N λ-clouds has a cloud-base mass flux M_j. (Note that we are only considering an L-cloud subensemble.) When $z\Delta\lambda \ll 1$, we expect the cloud work function of each λ-cloud (A_j) to be close to that of the L-cloud (A), i.e.

$$A_j \approx A, \quad j = 1, 2, \ldots, N. \tag{5.14}$$

Meanwhile each λ-cloud and the L-cloud satisfy (5.9), i.e.

$$M_j = \frac{\tau_D}{\alpha_\lambda} A_j, \tag{5.15}$$

and

$$M_B = \frac{\tau_D}{\alpha_L} A, \tag{5.16}$$

where we use α_λ and α_L to represent the α's used in the λ-approach and the L-approach, respectively. Note that we still assume that one value of α_λ applies to all λ-clouds. Summing over the N λ-clouds, using (5.16), (5.15) and (5.14), we get

$$\sum_{j=1}^{N} M_j \approx \frac{\tau_D}{\alpha_\lambda} \sum_{j=1}^{N} A_j \sim \frac{\tau_D}{\alpha_\lambda} NA. \quad \textbf{(5.17)}$$

The total mass flux M_B should not change much when N increases due to the use of a smaller $\Delta\lambda$

$$\sum_{j=1}^{N} M_j \approx M_B. \quad \textbf{(5.18)}$$

To satisfy (5.18), (5.17), and (5.16), we must have

$$\alpha_\lambda = N\alpha_L. \quad \textbf{(5.19)}$$

Here we have assumed that α/τ_D is not a function of cloud type. After all, we expect the clouds detraining in the same layer to be very similar to each other, especially when Δz is very small.

Remember that N is the number of clouds detraining in a certain layer, and that it increases when $\Delta\lambda$ decreases. We conclude, therefore, that α/τ_D should depend on $\Delta\lambda$. On the other hand, N can also vary with layer and time, given a $\Delta\lambda$. However, α should not be a function of height, since it is defined with respect to the cumulus subensemble $[K(\lambda) = \alpha M_B^2(\lambda)]$. For this reason, the "$N$" from now on should also be considered as a vertical integral. In other words, N is the ratio of the total number of λ-clouds to the number of model layers. We assume that these λ-clouds are evenly allocated to each layer so that each model layer contains N detraining clouds.

To give an interpretation of (5.19), we can rewrite (2.14) by using the approximation $1-\sigma \sim 1$,

$$\alpha_\lambda = \frac{1}{2\varepsilon}\int_{z_S}^{z_T} \frac{\eta^2(\lambda, z)}{\rho\sigma(\lambda, z)} dz. \tag{5.20}$$

Again we are considering λ-clouds that detrain in one model layer, therefore, we can assume that the normalized mass flux of each λ-cloud is similar to that of the L-cloud

$$\eta(\lambda, z) \approx \eta_L(z). \tag{5.21}$$

Since we do not expect the dynamics of the interaction between the cumulus clouds and the environment to change just because we "re-group" cumulus subensembles, we expect σ but not ε to change. It is also obvious that α_λ can be easily changed by a factor of 2 or more by changing σ.

Provided that every L-cloud is divided into N sub-groups (λ-clouds) that detrain in the same model layer (due to the use of a small $\Delta\lambda$), we have

$$\sigma(z) = \sum_{j=1}^{N} \sigma_j(z). \tag{5.22}$$

If we can write

$$\sigma_j(z) \approx \frac{\sigma_L(z)}{N}, \tag{5.23}$$

this can account for the change of α that is needed to satisfy (5.9). In this case, ε should be a quasi-constant. As an example, we can refer back to Fig. 5.3, in which the "plump" L-cloud B is divided into two "thinner" λ-clouds b and d. We conclude that σ is the main factor that makes α different when a different $\Delta\lambda$ is used. Note that σ should be reduced *throughout the convective layer* when a smaller $\Delta\lambda$ is used.

The above discussion shows that α should depend on $\Delta\lambda$, which is a given constant and does not change with time. However, we have mentioned that N can vary with time, depending on the large-scale environment. Can we still use an α that is constant with time?

When one λ-cloud penetrates into a certain layer and causes an increase of σ there, it should not cause much change in α, which is an integral through the entire cloud depth. After all, σ below the cloud-top layer is not supposed to change much due to a small change of a cloud-top height. Therefore, it is still reasonable to use an α that is constant in time.

We have shown that α should increase with N, and we know that N increases with Δz and decreases with $\Delta\lambda$. We can therefore tentatively formulate α as

$$\alpha \sim \beta\frac{\Delta z}{\Delta\lambda}, \tag{5.24}$$

where β is a universal parameter that does not depend on either Δz or $\Delta\lambda$. According to (5.20), β should be a function of ε and the cloud depth, $z_T - z_B$.

5.2.4.2 Determining $\Delta\lambda$ and λ_{max}

The λ-approach is practically useful only if the results do not strongly depend on $\Delta\lambda$ as long as $\Delta\lambda \leq (\Delta\lambda)_{max}$ is satisfied, and they converge when $\Delta\lambda \to 0$, and can be applied in any large-scale environment. We will test different values of $\Delta\lambda$ in the 1-D model later in the chapter. The rest of this approach is to determine $(\Delta\lambda)_{max}$.

For the similar reason we require the $\Delta\lambda$ to be small enough, we also expect the largest fractional entrainment rate, λ_{max}, to be large enough that the shortest clouds detrain in the lowest layer in the free atmosphere (i.e., the layer just above the PBL where all cumulus clouds originate). Both $\Delta\lambda$ and λ_{max} should depend on the environment and the vertical resolution, Δz.

When $\Delta z \to 0$, the shallowest cumulus clouds lose their buoyancy immediately above the PBL. On the other hand, keep in mind that cumulus convection only occurs in the statically stable environment. (If this condition is not satisfied, the dry convective adjustment is triggered instantaneously and eliminate the dry convective instability.) The cumulus-induced subsidence can cause warming only when the environment is statically stable.

Often the saturation moist static energy increases with height. Usually, air parcels are negatively buoyant just above the PBL, if the PBL is not saturated. If there is little entrainment, the latent heat release from condensation soon gives the parcels positive buoyancy, and keeps them going up.

For the cumulus clouds to detrain in a layer, two conditions must be satisfied: the air parcel must lose its buoyancy at certain height, and the vertically integrated buoyancy (cloud work function) from the PBL top to this height must be positive.

Experience shows that when $\Delta\lambda$ is sufficiently small, the model itself will choose the maximal λ. Clouds with entrainment that is too strong will not be able to exist. Therefore, we do not need to set any limit for λ. Lord (1978) had to set a limit of λ as 2×10^{-3} m^{-1} for a 9-layer model, which was not explained. Also this maximal value of λ may vary with the vertical resolution of the model. Why did Lord need an upper limit for λ?

5.3 Numerical Experiments with the λ-approach

To test the λ-approach, we repeat the one dimensional GATE simulation done in Chapter 3. We allow up to 200 λ-clouds to exist in this 9-layer model. We used $\tau_D = 600$ sec all through our tests. We tested the model with different values of $\Delta\lambda$ to see if the results converge when $\Delta\lambda \to 0$.

5.3.1 Consistency Tests With $\Delta\lambda$

We started with a large $\Delta\lambda$ of 10^{-3} m^{-1}, using $\alpha = 3 \times 10^{8}$ m^4 kg^{-1}. Results show that in the beginning, the non-entraining cloud loses buoyancy in the third layer of the model, and the cloud of $\lambda = 10^{-3}$ m^{-1} detrains in the sixth layer. We have imposed the

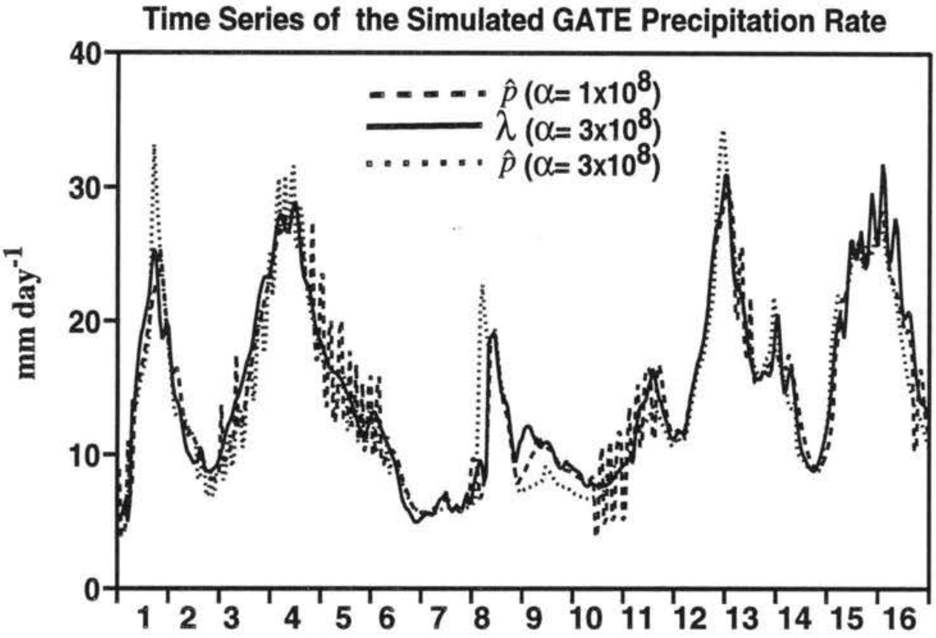

FIGURE 5.4: Simulated GATE precipitation rate using λ (solid line, with $\alpha = 3 \times 10^8$ m^4 kg^{-1}), and or $\hat{p}$ (dashed line, with $\alpha = 10^8$ m^4 kg^{-1}) as the independent cloud spectral parameter. Lord's approach with $\alpha = 3 \times 10^8$ m^4 kg^{-1} is also shown in the dotted line. In the λ-approach, $\Delta\lambda = 10^{-5}$ m^{-1} has been used.

condition that the clouds with unsaturated cloud-tops do not exist. Apparently, the number $\Delta\lambda = 10^{-3}$ m^{-1} is too big to allow any cloud to detrain in layers 4 and 5. On the other hand, the mass flux of the non-entraining cloud cannot take over the effects (functions) of the clouds that "should have" detrained in layers 4 and 5. This leads to an insufficient cumulus heating in layer 6 and below. As a result, these levels keep cooling and soon saturate. The near-neutral sounding allows very strongly-entraining clouds to be buoyant, and a huge mass flux is delivered by shallow clouds. Therefore, the big $\Delta\lambda$ causes a numerical problem.

We then tried $\Delta\lambda = 10^{-4}$ m^{-1} and with all other parameters remaining the same. We get much better results. However, sometimes some layers still do not have clouds detraining.

When we reduced $\Delta\lambda$ to 2×10^{-5} m^{-1}, we had to impose the constraint that the in-cloud temperature must be higher than the environment in the same level. There are clouds detraining in layers 3, 4, 5, and 6 most of the time, and sometimes clouds can penetrate into layer 2.

Fig. 5.4 shows the simulated precipitation rate using the λ-approach (with $\Delta\lambda = 10^{-5}$ m^{-1}), and a comparison with that obtained using Lord's approach. We used $\alpha = 3 \times 10^8$ m^4 kg^{-1} in the λ-approach and $\alpha = 10^8$ m^4 kg^{-1} in Lord's approach. The results from the two approaches are very similar, except that most of the noise is removed when the λ-approach is used. Also shown in Fig. 5.4 is the precipitation rate from Lord's approach using $\alpha = 3 \times 10^8$ m^4 kg^{-1}, which is obviously different from the other two simulations. We need to use a larger α for the λ-approach because more clouds detrain in each layer. Generally speaking, there are all together about 3 to 5 times as many cloud types active with the λ-approach, compared to the L-approach (8 types allowed and 5 types active). The slight noise on the 15th and the 16th days is due to the similar reason as mentioned above, and goes away when a smaller $\Delta\lambda = 2.5 \times 10^{-6}$ m^{-1} is used. The time evolution of the total precipitation rate is almost identical when we further reduce $\Delta\lambda$ and meanwhile increase α proportionally, according to (5.23).

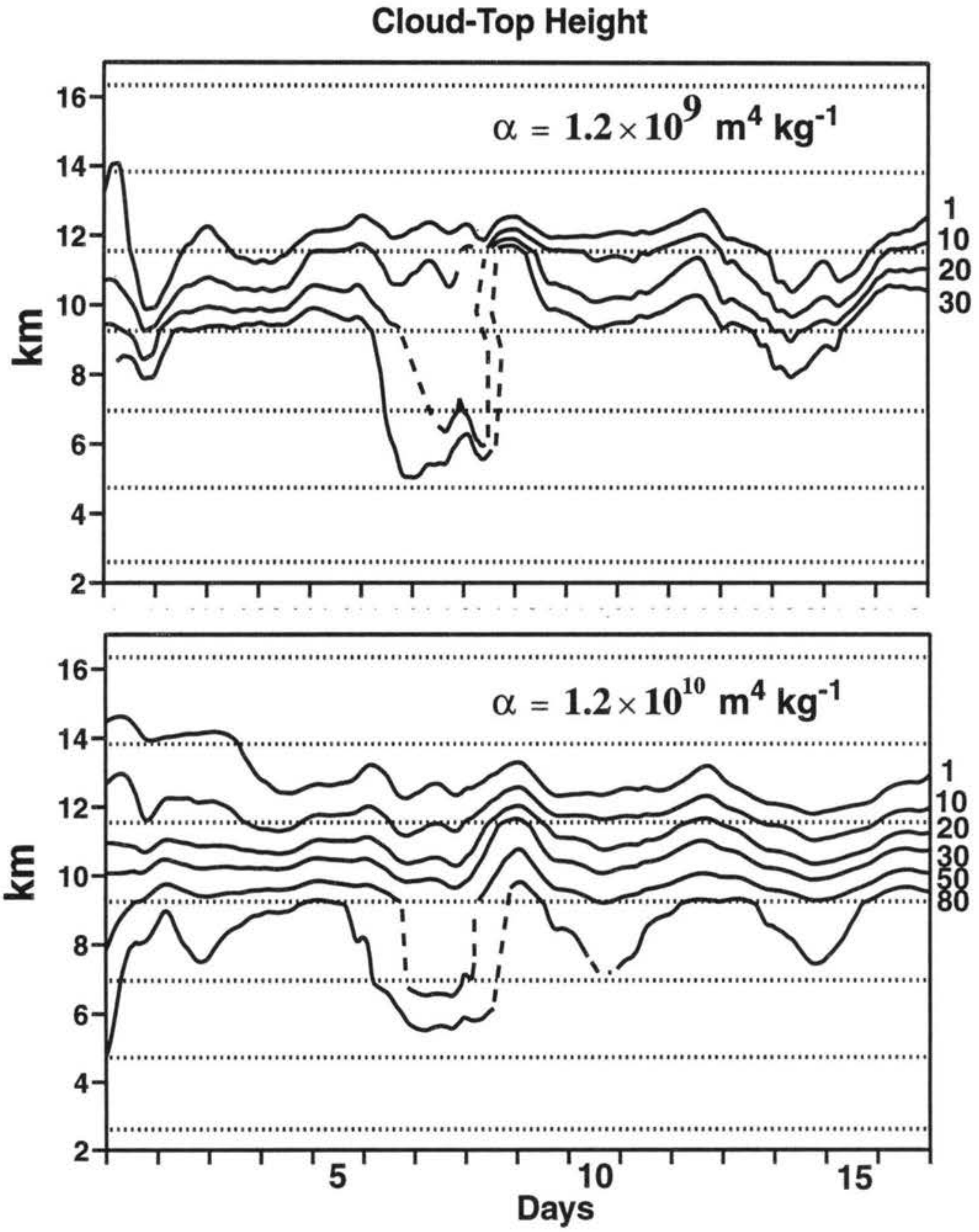

FIGURE 5.5: Cloud-top height for a variety cloud types. Numbers on the right are the cloud types representing clouds of λ equaling n times of 2.5×10^{-6}, n=10, 20, 30, 50, and 80; n=1 represents the non-entraining clouds. Dotted lines separate model layers. Dashed lines mean clouds are not existent due to unsaturated cloud-top.

From our consistency tests, we conclude that our results from the GATE simulation converge when $\Delta\lambda \rightarrow 0$. (There is no cloud detraining in layers 7 and 8 at any time though, even when $\Delta\lambda = 2.5 \times 10^{-6}$.)

5.3.2 Cloud-Top Height

As mentioned earlier, the cloud-top height of a λ-cloud can vary with time. This can be seen in the results of our experiments. Fig. 5.5 shows the time variation of the cloud-top heights of non-entraining cloud and clouds 10, 20, 30, 50, and 80, with $\Delta\lambda = 2.5 \times 10^{-6}$. In the case of $\alpha = 1.2 \times 10^{9}$ m^4 kg^{-1}, the non-entraining cloud has its top-height vary between 10 km and 14 km. The number of clouds detraining in layer 4 (~9 to 11.5 km) of the model also vary with time.

We shall further compare the results from the λ-approach and the L-approach in the next section. In all the results from the λ-approach to be discussed later in this chapter, we use $\Delta\lambda = 2.5 \times 10^{-6}$ m^{-1} and $\alpha = 1.2 \times 10^{9}$ m^4 kg^{-1}.

5.3.3 Cloud-Base Mass Flux

Fig. 5.6 shows the total cloud-base mass flux from the two different approaches. The agreement between the two approaches in this field is far from as good as in total precipitation. Generally speaking, the total cloud-base mass flux is much smaller during the peak convective events from the L-approach than from the λ-approach.

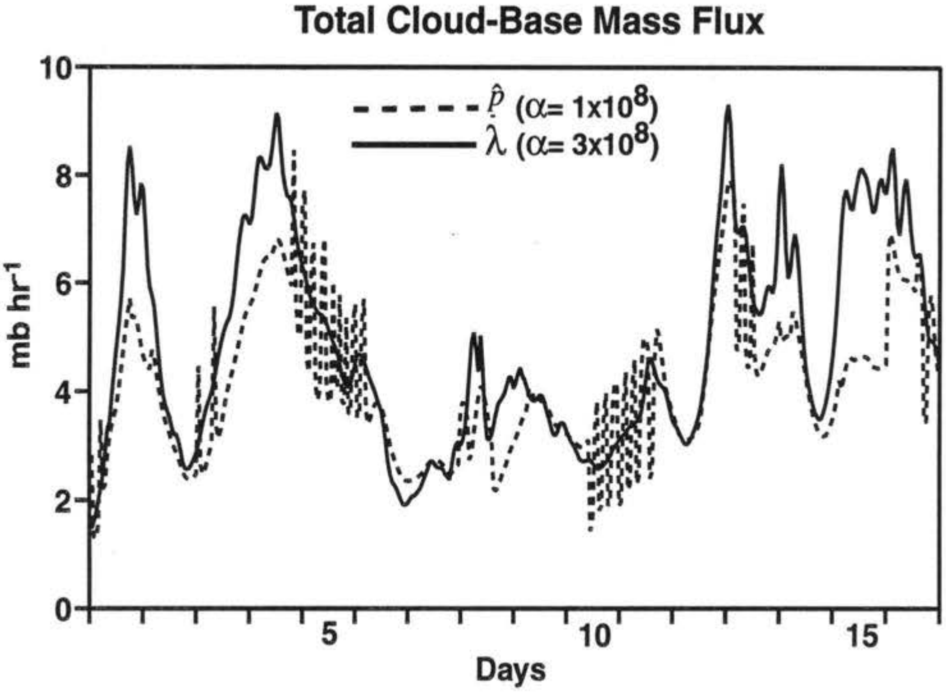

FIGURE 5.6: Total cloud-base mass flux in mb hr^{-1}. $\Delta\lambda = 2.5 \times 10^{-6}$ m^{-1} and $\alpha = 1.2 \times 10^{9}$ m^4 kg^{-1} have been used in the λ-approach.

A difference between these two approaches is the vertical distribution of the detrainment mass flux. The λ-approach allows shallower clouds to draw larger mass flux from the PBL than deeper clouds. In the L-approach with prognostic CKE, deeper clouds always have larger cloud work function which is a vertical integration from the cloud base to the cloud top. Larger work function results in larger cloud-base mass flux according to (5.9). Therefore, the detrainment mass flux (if existent) in the L-approach always increases with height. With the λ-approach, (5.9) still holds for each type of clouds. However, more than one type of clouds can detrain in a layer. This makes it possible that more mass actually detrains in a lower layer. This can be seen in Fig. 5.7.

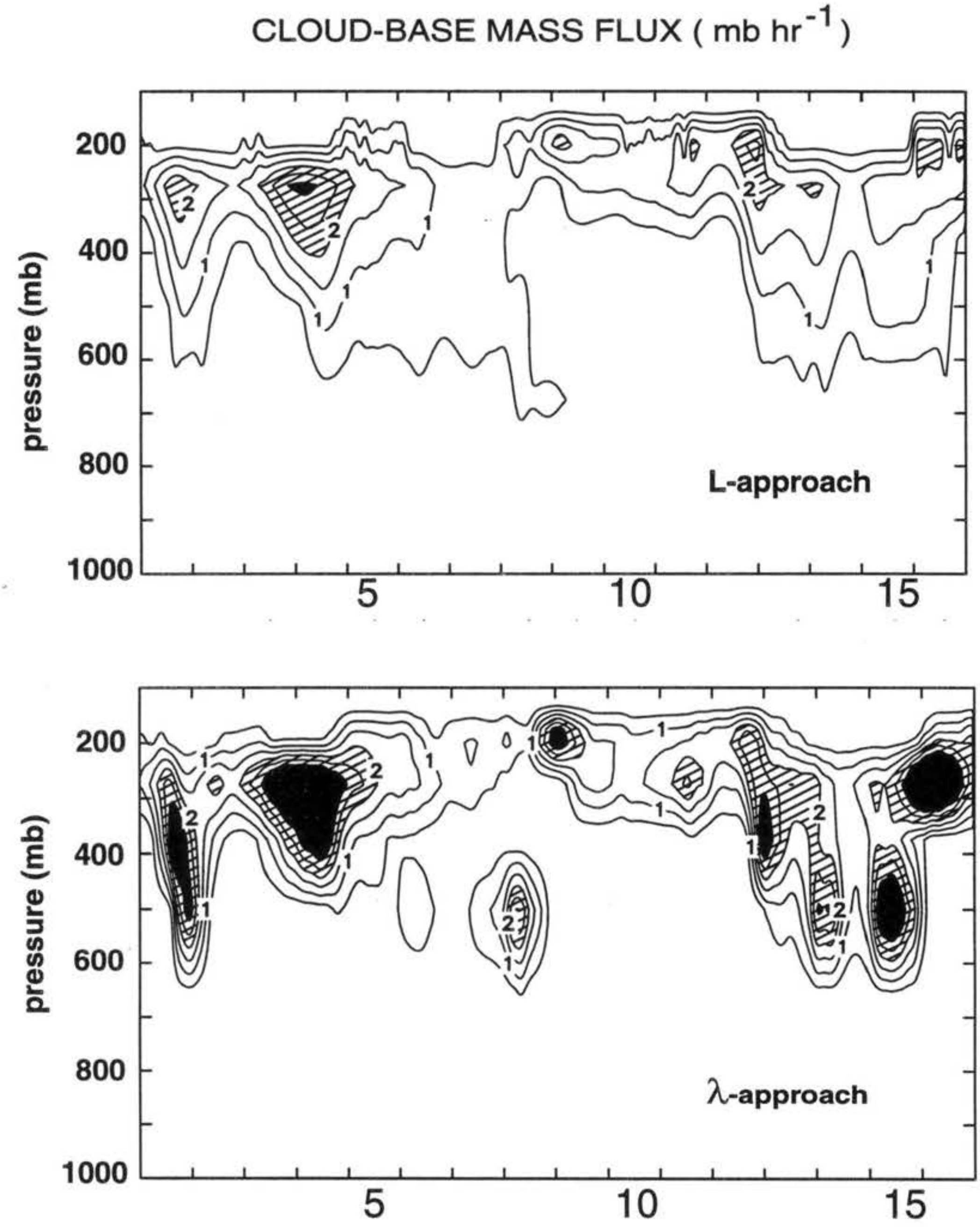

FIGURE 5.7: Cloud-base mass flux as a function of detrainment height and time. Figure shows the results from Lord's approach (above) and that from λ-approach. The contour interval is 0.5 mb hr^{-1}. Values larger than 2 mb hr^{-1} and 3 mb hr^{-1} are lightly and darkly shaded, respectively. Smoothing has been applied to make the figure easier to read. $\alpha = 3 \times 10^8\ m^4\ kg^{-1}$ has been adopted in the λ-approach.

Fig. 5.7 shows the time-pressure cross-section of the cloud-base mass flux for all clouds in terms of detrainment-level pressure. Results from both the λ-approach and the L-approach are shown. Comparing the λ-approach with the L-approach, maximal cloud-base mass flux can be carried by middle clouds and much more mass flux detrains between 400 mb and 600 mb. The high-level maxima generally intensify with the λ-approach. More mass detrained in lower layers simply means the larger frequency of occurrence for shallower clouds.

Fig. 5.8 shows the difference in temperature and water vapor mixing ratio between the results of the λ-approach and that of the L-approach. It is always warming below 600 mb from the L-approach to the λ-approach. This is because there is no cumulus cloud detraining in these layers and more mass flux detraining above, with the λ-approach, enhances the cumulus heating effect. The larger detrainment mass also leads to the cooling above 350 mb.

To examine the difference between the λ-approach and Lord's approach, again we look at the average Q_1 and Q_2 during four "severe" convective events. To be consistent with Chapter 3, we used the same criterion (13.5 mm day^{-1} in total precipitation) to define the "severe" convective events. We picked the periods when the cumulus precipitation is larger than this amount and calculate the time average of Q_1 and Q_2. The results are shown in Fig. 5.10 and Fig. 5.11, respectively. Observations are also shown for comparison.

The negative Q_1 above 300 mb is not as large with the λ-approach as with the L-approach. The apparent heating is generally smaller above 500 mb with the λ-approach

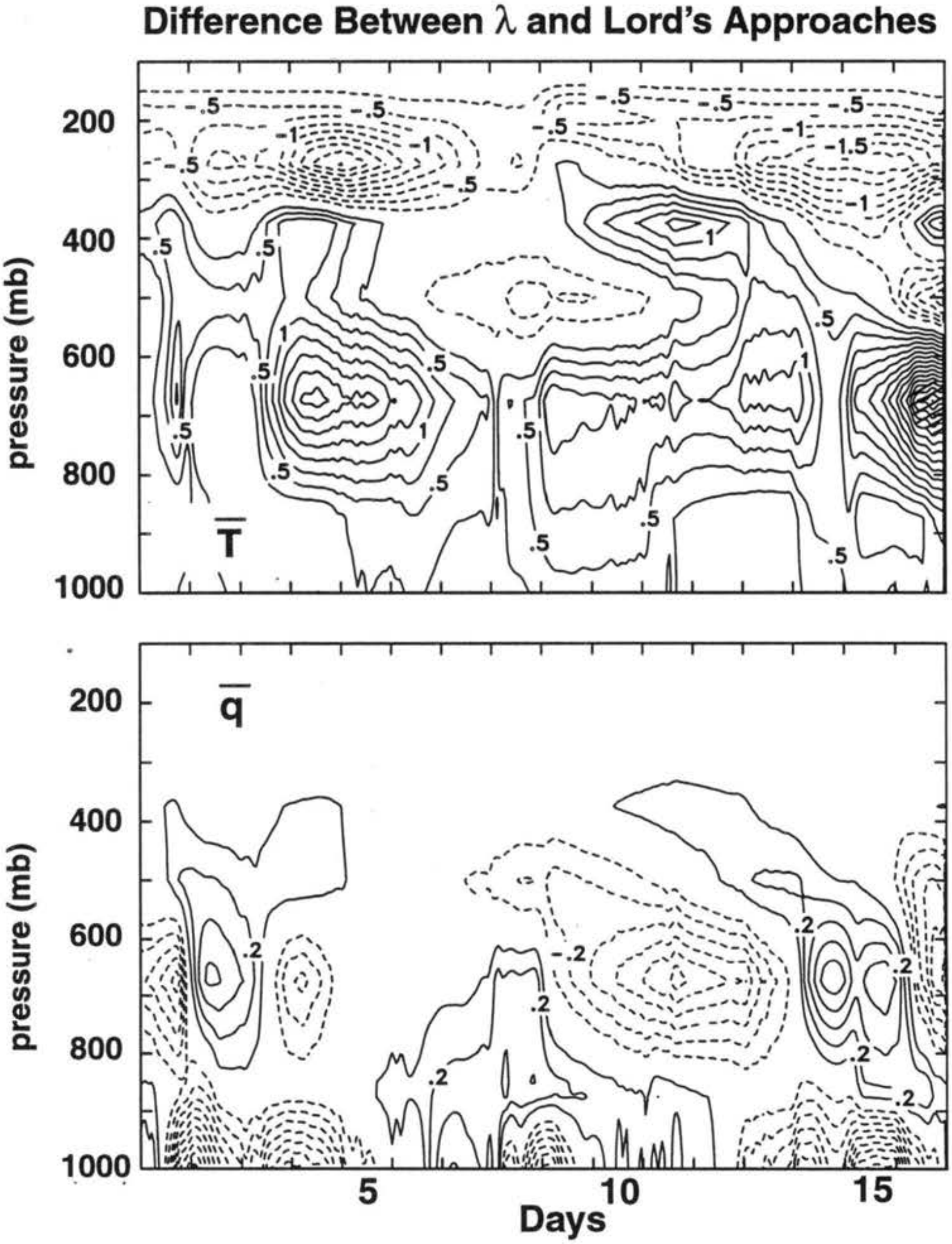

FIGURE 5.8: Difference in simulated temperature (upper panel) and water vapor mixing ratio using the λ-approach and Lord's approach. The contour intervals are 0.25 K and 0.1 g kg^{-1}, respectively. Temperature above 3 K is shaded.

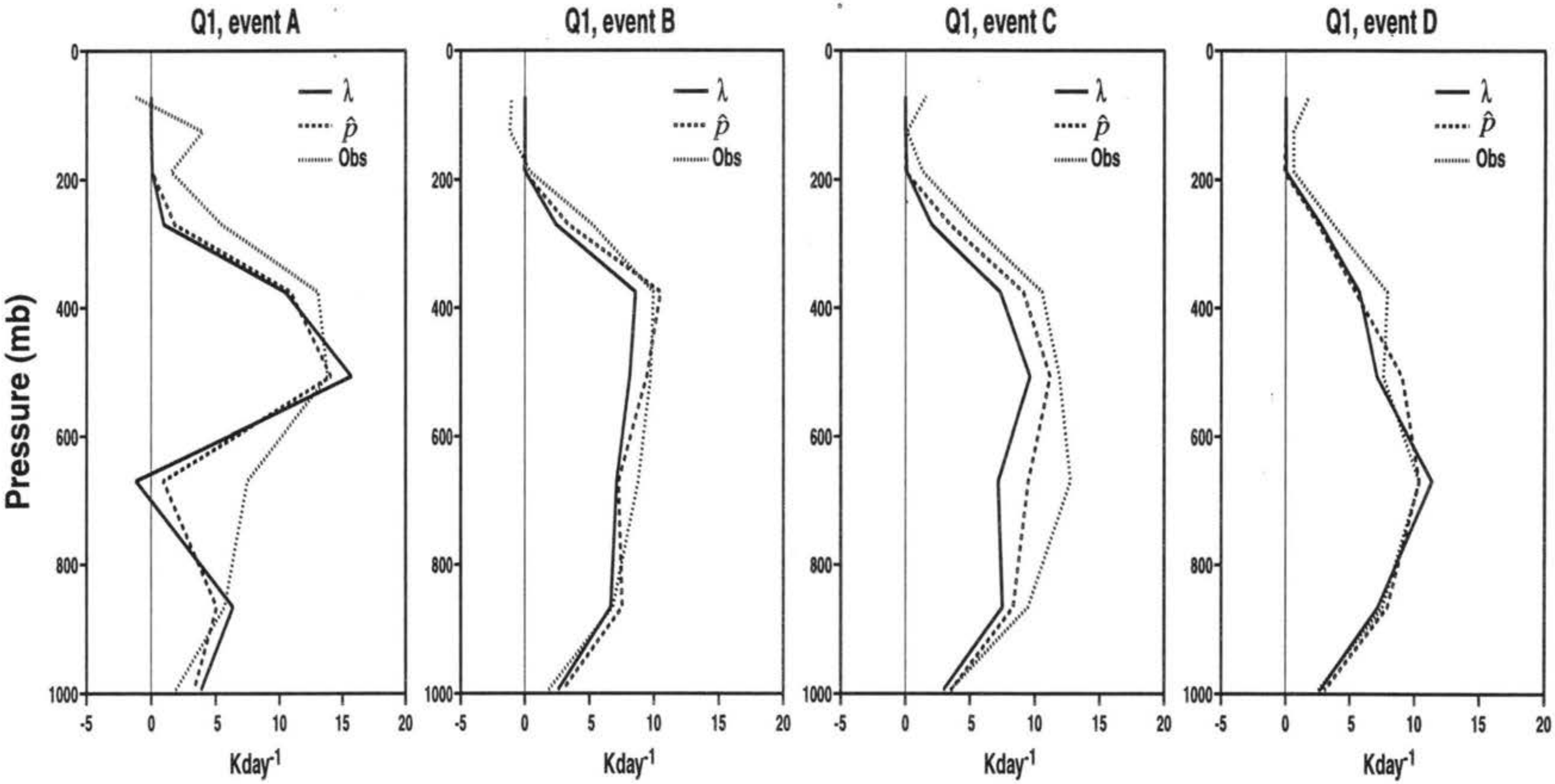

FIGURE 5.9: Time-averaged Q_1/c_p of the four “severe” events.

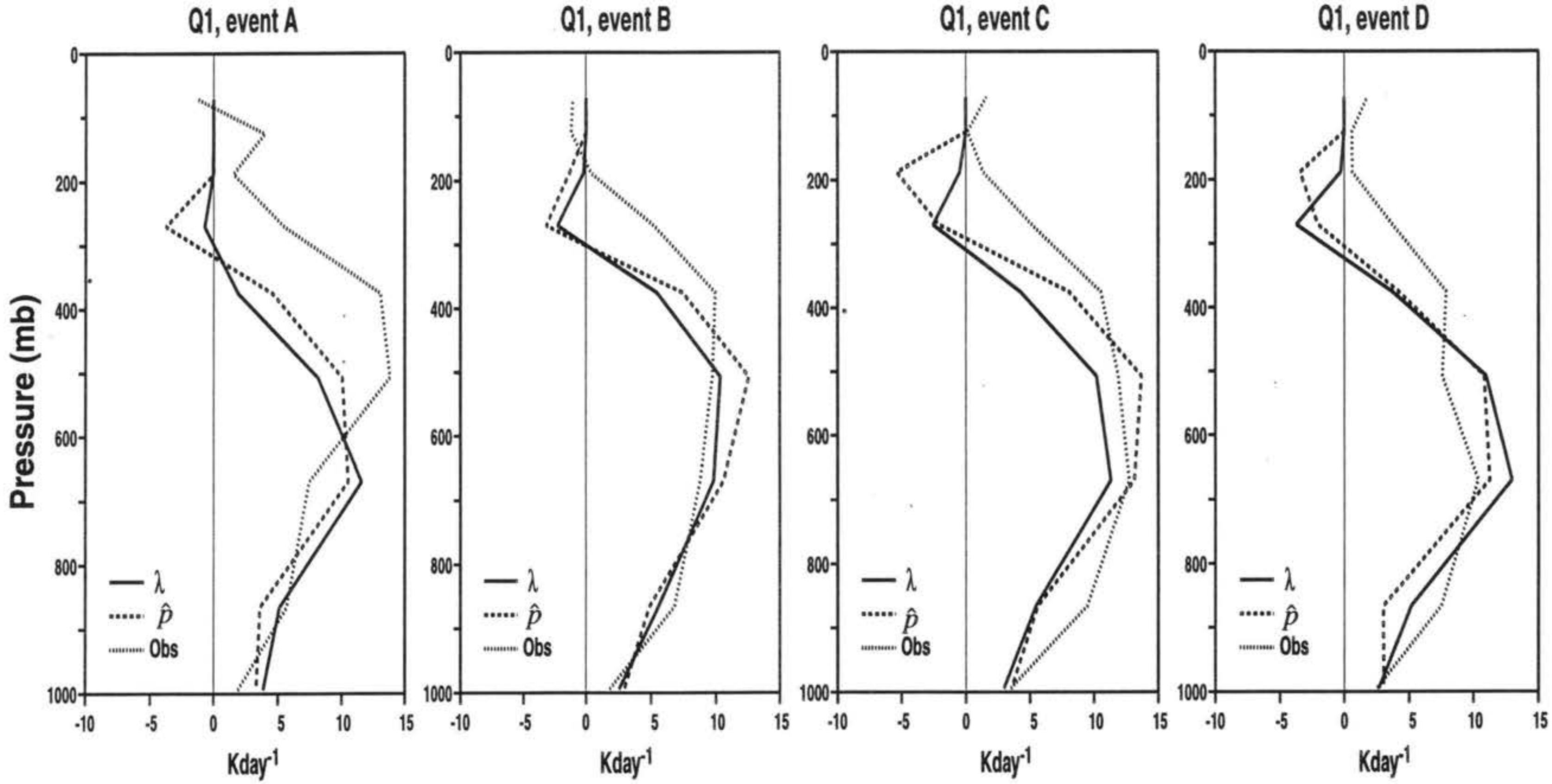

FIGURE 5.10: Same as Fig. 5.10, except that LSP heating is excluded.

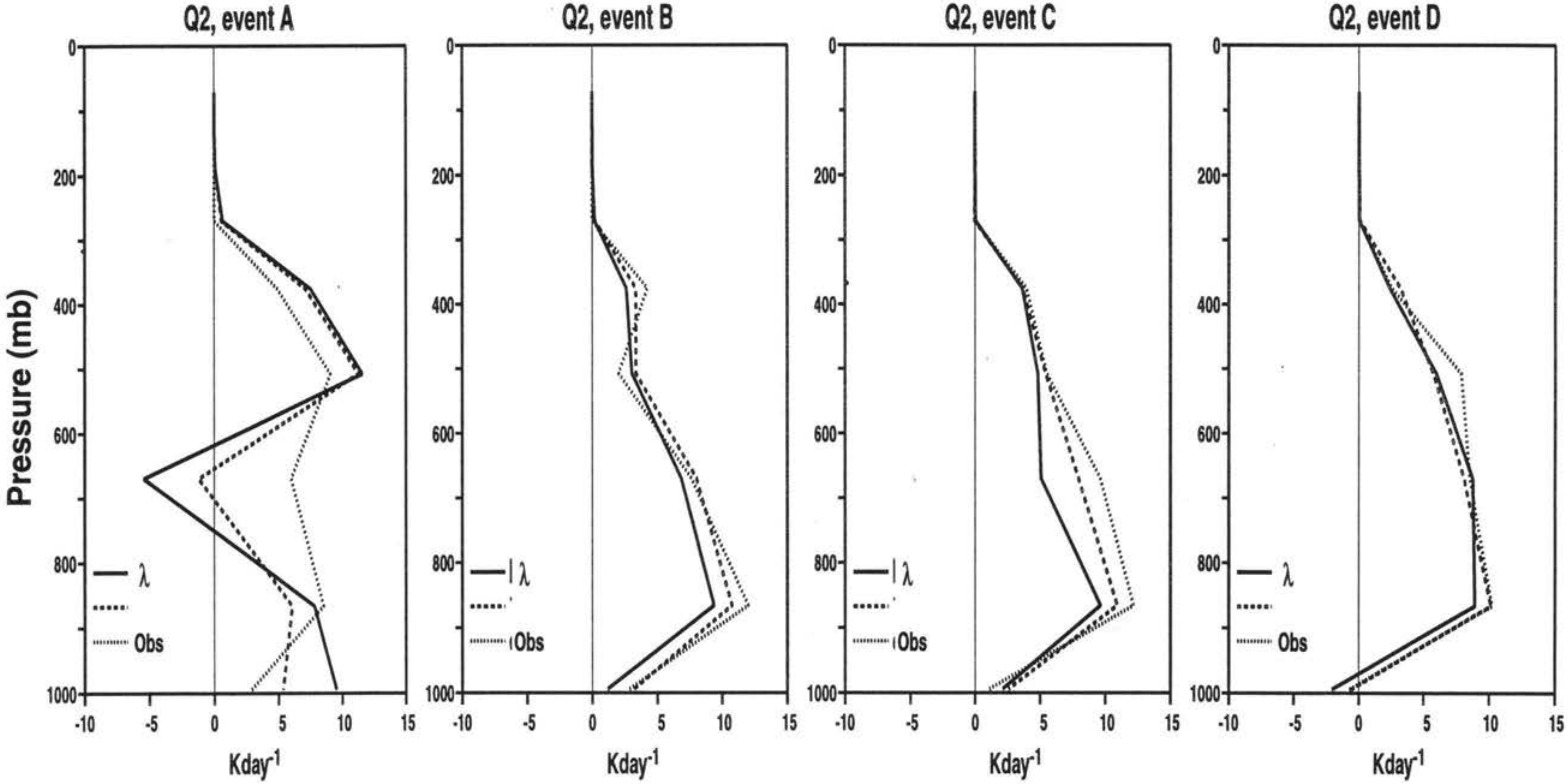

FIGURE 5.11: Time-averaged Q2 for the four events.

than with the L-approach. The maxima of the simulated apparent heating with either approach generally are still lower than that observed.

5.3.4 Value of α

We have concluded that the value of α should be inversely proportional to $\Delta\lambda$. However, that does not tell us what the absolute value of α is. We have tested with different values of α in the GATE simulation in Chapter 3, and found that a larger α leads to larger LSP while the total precipitation is almost unchanged.

An advantage of the λ-approach is that it is possible to isolate the effects of certain clouds by their identity, λ. For example, we can look at the role of non-entraining clouds or highly-entraining clouds separately. With Lord's approach, we can only look at the cumulus effects by model layers.

5.4 Summary

We reviewed early research on the entrainment in convective motions. The entrainment rate of a thermal is determined at the "virtual origin" and does not change with time or space. It seems reasonable to consider the entrainment rate as an inherent property of convective cells, and use it to define the cumulus subensemble in the cumulus parameterization problem. Arakawa and Schubert (1974) used the fractional entrainment rate as an independent variable, called cloud spectral parameter, in the cloud model.

Lord (1978), however, used the detrainment-level pressure to define cloud types. The detrainment pressure was favored over the fractional entrainment rate because the model can only resolve the cumulus effects in certain "layers". It seems convenient to identify the cumulus clouds with given model levels where their tops are found. In Lord's method, the fractional entrainment rate has to be obtained by iteration and it depends on the environment, and hence varies with time. Lord (1978) eventually had to deal with the tallest cumulus clouds separately. These clouds usually detrain in the middle of a layer. This approach is computationally costly, and is not compatible with the CKE method. The resolution of the cumulus convection is locked to the vertical resolution of the model.

We use λ as the cloud spectral parameter to replace Lord's approach. λ is treated as an independent variable and does not vary with time. For that reason, the cloud-top height of each cloud subensemble can rise or descend with time. No subensemble can suddenly appear or disappear instantaneously. Our approach appears to have improved the numerical results in a GATE simulation. The results are in good agreement with the two different approaches, except that the numerical noise is eliminated using our approach.

As with other independent variables, a $\Delta\lambda$ has to be determined in advance. It is also found that α should be related to $\Delta\lambda$. This can be explained using the relation (5.20) in which α is related to $\sigma(z)$, the areal coverage of the cumulus clouds.

The λ-approach appears to be practically useful. Interpolation replaces the iteration that is used in the L-approach and makes λ-approach computationally much cheaper. Experiments prove that the results using λ-approach does not strongly depend on either the

$\Delta\lambda$ chosen (if it is small enough) or the vertical resolution of the model. The method is proven to be consistent numerically.

One advantage of the λ-approach over the L-approach is that we can isolate and examine separately the effects of cumulus clouds of different λ's, and their roles in the large-scale environment. For instance, we can turn off the strongly-entraining clouds and compare the results with those of the whole cloud spectrum.

CHAPTER 6

Concluding Discussion

6.1 Summary

We have reviewed the cumulus parameterization problem. Many methods have been proposed, and the Arakawa-Schubert parameterization is the most successful by far. The key assumption of the A-S parameterization is the quasi-equilibrium of the cloud work function, which states that the cumulus ensemble is always in a statistical equilibrium with the large-scale environment. The cumulus convection immediately consumes the convective instability that the large-scale processes build up. Consequently, Arakawa and Schubert defined all the processes that are not directly related to the cumulus mass flux as the "large-scale forcing" for the cumulus convection. The definition of the large-scale forcing is not clear, however, especially with respect to the production of stratiform clouds and their interactions with radiation.

The concept of cloud work function quasi-equilibrium can also be linked to the quasi-equilibrium of cumulus kinetic energy (Lord and Arakawa, 1980). It is therefore convenient to directly use the cumulus kinetic energy equation, since the quasi-equilibrium of cumulus kinetic energy will be closely approximated automatically as long as the dissipation time-scale of the cumulus kinetic energy is short enough. This approach bypasses the ambiguity of the definition of the large-scale forcing. It also greatly simplifies the computation process and therefore allows future improvements in the physics such as the inclusion of downdrafts and multiple cloud bases, etc.

The prognostic CKE approach is closed through the introduction of a parameter, α, that relates the cumulus cloud-base mass flux to the CKE. A formula (Eq. 2.14) was derived for α which shows that α depends on the cloud depth. Accordingly, we need an α for each cumulus subensemble.

Before attempting to formulate an α for each subensemble, one dimensional experiments were conducted to test the prognostic CKE approach with a single constant α for all cloud types. For a given α in the experiment with imposed constant radiative cooling, the parameterized cumulus convection has reasonable interactions with the environment. However, the steady-state solution significantly depends on the value of α.

The "one-α" CKE approach was further tested in a GATE simulation, in which we imposed the observed large-scale advection and radiation hourly. Results showed that the time evolutions of precipitation and Q_1 and Q_2 are well reproduced with our cumulus parameterization. The over-estimation of precipitation during the "break" periods is due to the over-simplification of the PBL processes. The generally lower-than-observed Q_1 maxima and the cooling peak at high levels are related to the LSP. The simulated environment, however, is usually saturated above 400 mb. This indicates the inappropriate coupling between the parameterized cumulus convection and the LSP in the model.

Four GCM experiments were performed, with which we investigated the interactions among the parameterized cumulus convection, radiation, and large-scale dynamics. The results from the CKE approach were compared against those from the quasi-equilibrium approach. Deep convection occurs much more frequently with the CKE approach. This is due to the way in which the anvil-radiation effects are parameterized in the model.

With the unrealistic "binary-anvil" parameterization, the cloud work function quasi-equilibrium generates a January OLR that is only slightly larger than observed. The inadequacy, however, can be seen in the anvil incidence which is much smaller than that observed. The inadequacy of the binary anvils is somehow amplified by using the prognostic CKE cumulus parameterization. The significant over-estimation of the tropical OLR suggests the modification of the anvil-radiation interaction.

A simple fractional anvil parameterization was introduced, in which we allow "fractional coverage" of the anvil clouds. The introduction of the fractional anvils with the CKE parameterized cumulus convection (and an observed global-mean OLR) gives better January precipitation over land. Also cumulus convection occurs much more often.

Lord (1978) chose the detrainment pressure as the cloud spectral parameter. This approach, when combined with our prognostic CKE, leads to a numerical problem. To solve the problem, we replace Lord's approach with the λ-approach, which identifies cumulus subensembles by given fractional entrainment rates. The fractional entrainment rate in this case is thus treated as an independent variable in the model. Using λ as the "independent" cloud spectral parameter is a part of the development of the prognostic CKE parameterization.

With the λ-approach, the value of α should depend on $\Delta\lambda$ and the vertical resolution of the model. Even though we can identify clouds as many more subensembles, the total number of "cloud types" is always the number of model layers *when considering the cumulus interactions and their feedback on the environment.*

Since the λ-approach identifies cumulus subensembles with fractional entrainment rate instead of the layer "index" of the model, it appears to be a useful tool for analyzing the roles of cumulus clouds (in terms of characteristic of cumulus clouds themselves) in the general circulation. For instance, it is possible in a numerical experiment to turn off the highly-entraining clouds while meaningless to set the total cumulus effects in a certain model layer to zero.

6.2 Conclusions

We conclude from this study that:

• The prognostic-CKE cumulus parameterization simplifies the calculation and hence allows more sophisticated physics to be included in the large-scale numerical models.

• Experiments with the 1-D model showed that the steady-state solution depends on the value of α. LSP is a part of the "forcing" for the cumulus convection, and hence how we parameterize the LSP has direct effects on the results. However, the LSP is also a response to convective detrainment. This means that we cannot really clearly separate forcing and response, as Arakawa and Schubert (1974) did.

• In the 1-D GATE simulation, we can generally recover the time evolution of the precipitation rate and the vertical distribution of the apparent heat source and moisture sink. The atmosphere is too often saturated in the simulation, however. This is due to the over-simplified LSP which re-evaporates the precipitation falling from upper levels. LSP is not triggered until the whole grid box is saturated.

• In the GCM tests, it was found that the model produces much higher anvil incidence which dramatically reduces the incoming solar radiation in the tropics. The "fractional anvil" parameterization with the CKE approach produces improvements in the January global precipitation distribution over land. The higher anvil incidence is more realistic.

• Lord's approach was proven incompatible with the CKE approach. With this approach, λ is an independent variable and the value of α should depend on $\Delta\lambda$ and the vertical resolution of the model. The independent λ appears to be a physically more reasonable identifier for cloud types.

6.3 Future Work

With the simplification due to the introduction of the CKE approach, the downdraft effects of cumulus convection (Chen and Randall, 1995) and multiple-cloud-base cumulus (Ding, 1995) can be included in the CSU GCM. To improve the LSP, a new stratiform cloud parameterization (e.g. Fowler *et al.*, 1995) should be implemented. All these works are ongoing.

Although the "one-α" CKE approach appears to work reasonably well in our 1-D GATE and the GCM simulations, α should be "parameterized" so that the CKE approach includes more detailed cloud dynamics. A CEM can be a useful tool to help us understand and implement the cloud dynamics in the cumulus parameterization.

We can also easily include the shear production term in the CKE equation. The momentum flux in the shear production term can be easily parameterized according to Wu and Yanai (1994).

The important point is that the new ideas that we have developed in this report, while useful in themselves, also open the door to many additional improvements to the parameterization that might otherwise have been impossible.

REFERENCES

Albrecht, B. A., V. Ramanathan and B. A. Boville, 1986: The effects of cumulus moisture transports on the simulation of climate with a general circulation model. *J. Atmos. Sci.*, 43, 2443-2462.

Anthes, R. A., 1977: A cumulus parameterization scheme utilizing a one-dimensional cloud model. *Mon. Wea. Rev.*, **105**, 270-286.

Arakawa, A and J.-M. Chen, 1987: Closure assumptions in the cumulus parameterization problem. *WMO/IUGG Symposium on Short- and Medium- range Numerical Weather Prediction*, Tokyo, 107-130.

Arakawa, A., and V. R. Lamb, 1977: Computational design of the basic dynamical processes of the UCLA general circulation model. *Methods in Computational Physics*, 17, Academic Press, New York, pp. 173-265.

Arakawa, A., and V. R. Lamb, 1981: A potential enstrophy and energy conserving scheme for the shallow water equations. *Mon Wea Rev*, **109**, 18-36.

Arakawa, A and W. H. Schubert, 1974: Interaction of a cumulus cloud ensemble with the large-scale environment, Part I. *J. Atmos. Sci.*, **31**, 674-701.

Arakawa, A and K.-M. Xu, 1990: The macroscopic behavior of simulated cumulus convection and semiprognostic tests of the Arakawa-Schubert cumulus parameterization. *Proc. of the Indo-U.S. seminar on parameterization of sub-grid scale processes in dynamical models of medium-range prediction and global climate.* Pune, India.

Asai, T, 1964: Cumulus convection in the atmosphere with vertical wind shear: numerical experiment. *J. Meteor. Soc. Japan*, **42**, 245-259.

Batchelor, G. K., 1954: Heat convection and buoyancy effects in fluids. *Quart. J. Roy. Met. Soc.*, **80**, 339-358.

Betts, A. K., 1986: A new convective adjustment scheme. Part I: Observational and theoretical basis. *Quart. J. R. Met. Soc.*, **112**, 677-691.

Betts, A. K. and M. J. Miller, 1986: A new convective adjustment scheme. Part II: Single column tests using GATE wave, BOMEX, ATEX and arctic air-mass data sets. *Quart. J. R. Met. Soc.*, **112**, 693-709.

Bunker, A., B. Haurwitz, J. S. Malkus, and H. Stommel, 1949: The vertical distribution of temperature and humidity over the Caribbean Sea. *Pap. Phys. Ocean. Meteor., Mass. Inst. Tech. and Woods Hole Ocean. Instn.*, **11**, No. 1.

Charney, J. G. and A. Eliassen, 1964: On the growth of hurricane depression. *J. Atmos. Sci.*, **21**, 68-75.

Chen, C.-H. and D. A. Randall, 1995: Modeling the effects of convective downdrafts on the global circulation of the atmosphere. In preparation for *J. Geophy. Res.*

Cheng, M. D., 1989: Effects of downdrafts and mesoscale convective organization on the heat and moisture budgets of tropical cloud clusters. Part II: Effects of convective-scale downdrafts. *J. Atmos. Sci.*, **46**, 1540-1564.

Cheng, C. -P., and R. A. Houze, Jr., 1979: The distribution of convective and mesoscale precipitation in GATE radar echo patterns. *Mon. Wea. Rev.*, **107**, 1370-1381.

Deardorff, J. W., 1972: Parameterization of the planetary boundary layer for use in general circulation models. *Mon. Wea. Rev.*, **100**, 93-106.

Ding, P., 1995: A parameterization of cumulus convection with multiple cloud base levels. Ph.D dissertation, Colorado State University, Fort Collins, 210 pp.

Donner, L. J., H.-L. Kuo and E. J. Pitcher, 1982: The significance of thermodynamic forcing by cumulus convection in a general circulation model. *J. Atmos. Sci.*, **39**, 2159-2181.

Fowler L. D., D. A. Randall, and S. A. Rutledge, 1995: Liquid and ice cloud microphysics in the CSU general circulation model. Part I: Model description and results of a baseline simulation. Submitted to *J. Climate.*

Frank, W. M., 1976: The structure and energetics of tropical cyclones. Atmospheric science paper No. 258, Colorado State University, 180 pp.

Frank, W. M., 1978: The life cycles of GATE convective system. *J. Atmos. Sci.*, **35**, 1256-1264.

Hack, J. J., B. A. Boville, J. T. Kiehl, P. J. Rasch and D. L. Williamson, 1994: Climate statistics from the national center for atmospheric research community climate model CCM2. *J. Geophy. Res.*, **99**, No D10, 20785-20813.

Harshvardhan, R. Davies, D. A. Randall, and T. G. Gorsetti, 1987: A fast radiation parameterization for general circulation models. *J. Geophys. Res.*, **92**, 1009-1016.

Harshvardhan, D. A. Randall, T. G. Corsetti and D. A. Dazlich, 1989: Earth radiation budget and cloudiness simulations with a general circulation model. *J. Atmos. Sci.*, **46**, 1922-1942.

Hartmann, D. L., H. H. Hendon, and R. A. Houze, Jr., 1984: Some implications of the mesoscale circulations in tropical cloud clusters for large-scale dynamics and climate. *J. Atmos. Sci.*, **41**, 113-121.

Johnson, R. H., 1976: The role of convective-scale precipitation downdrafts in cumulus and synoptic-scale interactions. *J. Atmos. Sci.*, **33**, 1890-1910.

Johnson, R. H., 1980: Diagnosis of convective and mesoscale motions during phase III of GATE. *J. Atmos. Sci.*, **37**, 733-753.

Kao, C.-Y. J. and Y. Ogura, 1987: Response of cumulus clouds to large-scale forcing using the Arakawa-Schubert cumulus parameterization. *J. Atmos. Sci.*, **44**, 2437-2458.

Kuo, H. L., 1965: On formation and intensification of tropical cyclones throughout latent heat release by cumulus convection. *J. A. S.*, **22**, 40-63.

Levine, J., 1959: Spherical vortex theory of bubble-like motion in cumulus clouds. *J. Meteor.*, **16**, 653-662.

Lilly, D. K. and B. F. Jewett, 1990: Momentum and kinetic energy budgets of simulated supercell thunderstorms. *J. Atmos. Sci.*, **47**, 707-726.

Lin, C.-C., 1994: Development of an improved cloud model for use in cumulus parameterization. Ph. D. dissertation. University of California, Los Angeles, 252 pp.

Lord, S. J. and A. Arakawa, 1980: Interaction of a cumulus cloud ensemble with the large-scale environment, Part II. *J. Atmos. Sci.*, **37**, 2677-2692.

Lord, S. J. and W. C. Chao and A. Arakawa, 1982: Interaction of a cumulus cloud ensemble with the large-scale environment, Part IV: The discrete model. *J. Atmos. Sci.*, **39**, 104-113.

Lord, S. J., 1982: Interaction of a cumulus cloud ensemble with the large-scale environment, Part III: Semi-prognostic test of the Arakawa-Schubert cumulus parameterization. *J. Atmos. Sci.*, **39**, 88-103.

Lord, S. J., 1978: Development and observational verification of a cumulus cloud parameterization. Ph.D. dissertation, University of California, Los Angeles, 359 pp.

Ludlam, F. H., 1980: Clouds and storms: the behavior and effect of water in the atmosphere. *Penn. State Univ. Press.*, 405 pp.

Manabe, S., J. Smagorinsky and R. F. Strickler, 1965: Simulated climatology of a general circulation model with a hydrologic cycle. *Mon. Wea. Rev.*, **93**, 769-797.

Manabe, S. and R. F. Strickler, 1964: Thermal equilibrium of the atmosphere with a convective adjustment. *J. Atmos. Sci.*, **21**, 361-385.

Ogura, Y., 1962: Convection of isolated masses of a buoyant fluid: A numerical calculation. *J. Atmos. Sci.*, **19**, 492-502.

Randall, D. A., 1989: Cloud Parameterization for Climate Models: Status and Prospects. *Atmospheric Research*, **23**, 345-362.

Randall, D. A. and D.-M. Pan, 1993: Implementation of the Arakawa-Schubert cumulus parameterization with a prognostic closure. *Monograph on Cumulus parameterization*, 137-144.

Randall, D. A., Harshvardhan, D. A. Dazlich and T. G. Corsetti, 1989: Interactions among radiation, convection, and large scale dynamics in a general circulation model. *J. Atmos.*

Sci., **46**, 1943-1970.

Raymond, D. J and K. A. Emanuel, 1993: The Kuo cumulus parameterization. *Monograph on Cumulus parameterization*, 145-147.

Rutledge, S. A. and R. A. Houze, Jr., 1987: A diagnostic modeling study of the trailing stratiform region of a midlatitude squall line. *J. Atmos. Sci.*, **44**, 2640-2656.

Scorer, R. S., 1957: Experiments on convection of isolated masses of buoyant fluid. *J. Fluid Mech.*, **2**, 583-594.

Seitter, K. L. and H.-L. Kuo, 1983: The dynamical structure of squall-line type thunderstorms. *J. Atmos. Sci.*, **40**, 2831-2854.

Simpson, J., R. H. Simpson, D. A. Andrews and M. A. Eaton, 1965: Experimental cumulus dynamics. *Rev. Geophys.* **3**, 387-413.

Simpson, J. and V. Wiggert, 1969: Models of precipitating cumulus towers. *Mon. Wea. Rev.*, **97**, 471-489.

Sloss, P. W., 1967: An empirical examination of cumulus entrainment. *J. Appl. Meteor.*, **6**, 878-881.

So, S. S., 1982: An observational study of the role of convection in the Baiu situation with special attention to the Arakawa-Schubert cumulus parameterization. Ph.D. dissertation, Geophysical Institute, University of Tokyo, 133 pp.

Stommel, H., 1947: Entrainment of air into a cumulus cloud. *J. Meteor.*, **4**, 91-94.

Stommel, H., 1951: Entrainment of air into a cumulus cloud II. *J. Meteor.*, **8**, 127-129.

Stull, R. B., 1988: An introduction to boundary layer meteorology. *Kluwer academic publishers*, 666 pp.

Tiedke, M., 1985: Effect of physical parameterization on the large-scale flow in the ECMWF model. *Seminar on physical parameterization for numerical models of the atmo-*

sphere, Reading, U.K., European Centre for Medium Range Weather Forecasts, 277-314.

Wu, X. and M. Yanai, 1994: Effects of vertical wind shear on the cumulus transport of momentum: Observations and parameterization. *J. Atmos. Sci.*, **51**, 1640-1660.

Xu, K.-M., 1991: The coupling of cumulus convection with large-scale processes. Ph.D. dissertation, University of California, Los Angeles, 250 pp.

Xu, K.-M. and A. Arakawa, 1992: Semiprognostic tests of the Arakawa-Schubert cumulus parameterization using simulated data. *J. Atmos. Sci.*, **49**, 2421-2436.

Xu, K.-M. and K. A. Emanuel, 1989: Is the tropical atmosphere conditionally unstable? *Mon. Wea. Rev.*, **117**, 1471-1479.

Yanai, M., S. Esbensen and J.-H. Chu, 1973: Determination of bulk properties of tropical cloud clusters from large-scale heat and moisture budgets. *J. Atmos. Sci.*, **30**, 611-627.

Yanai, M., J.-H. Chu, T. E. Stark and T. Nitta, 1976: Response of deep and shallow tropical-maritime cumuli to large-scale processes. *J. Atmos. Sci.*, **33**, 976-991.

Appendix A

The Cloud Model Using λ as the spectral parameter

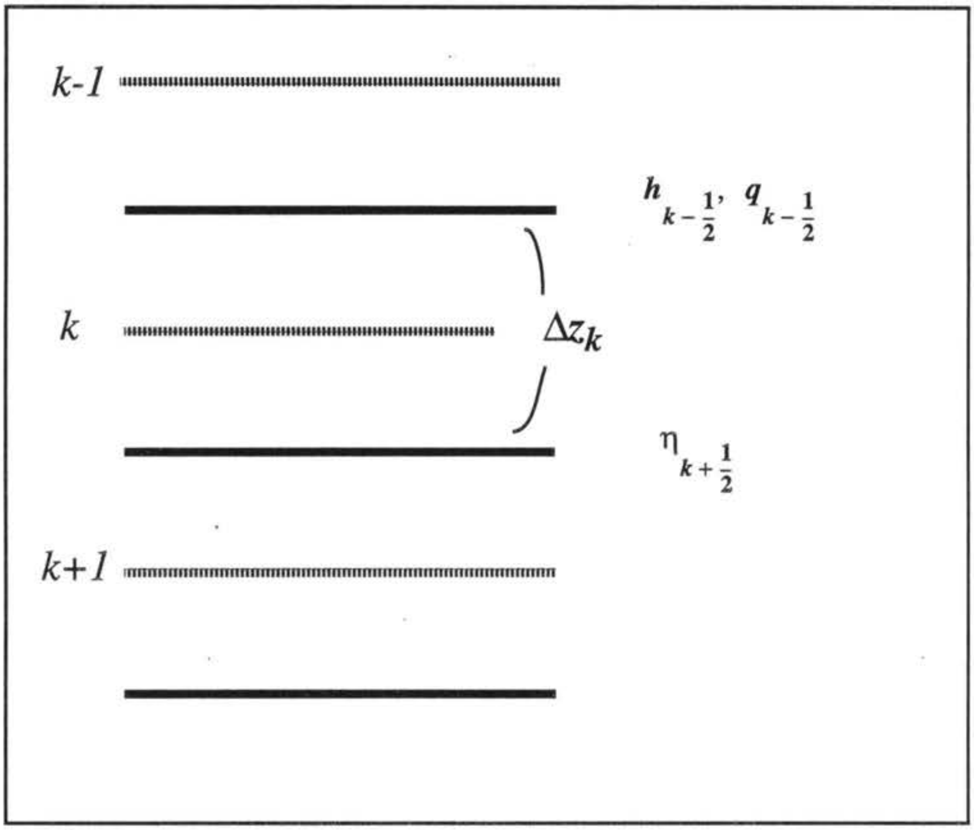

FIGURE 6: Vertical grid-structure.

The cloud model we used mostly follows Lord (1978). The difference is mainly the determination of the cloud tops. We fix the values of λ's, and let clouds grow or dissipate with time. This method is applied to solve the problem that sudden occurrence (disappearance) of certain types of clouds (and hence clouds' feedback to those levels) results only due to a penetration (retreat) of clouds into (from) a certain level. A special treatment of the cumulus feedback in the cloud-top layer is also introduced.

A.7 Arrangement of variables

Fig. 6 shows the arrangement of the variables on the vertical grid. All cloud variables are calculated on "even" levels (i.e., k-1/2, k+1/2, etc.) except for the net condensation, precipitation, and some temporary variables such as the cloud water before precipitation and before ice production.

A.8 Properties of Cumulus Subensembles

The normalized mass flux of cloud-type i (with fractional entrainment rate λ) at the top and the bottom of layer k are related by

$$\eta_{i,\,k-\frac{1}{2}} = (1+\lambda\Delta z_k)\,\eta_{i,\,k+\frac{1}{2}}\ , \tag{A.6}$$

where $\Delta z_k = z_{k-\frac{1}{2}} - z_{k+\frac{1}{2}}$. The moist static energy of cloud-type i is obtained by

$$h_{i,\,k-\frac{1}{2}} = \frac{h_{i,\,k+\frac{1}{2}} + \lambda\Delta z_k \bar{h}_k}{1+\lambda\Delta z_k}. \tag{A.7}$$

We then calculate the mixing ratios of the total cloud water before precipitation q^t

$$q^t_{i,\,k} = \frac{q^t_{i,\,k+\frac{1}{2}} + \lambda\Delta z_k \overline{q}^t_k}{1+\lambda\Delta z_k}, \tag{A.8}$$

and cloud ice q^I before ice formation

$$q^I_{i,\,k} = \frac{q^I_{i,\,k+\frac{1}{2}} + \lambda\Delta z_k \overline{q}^I_k}{1+\lambda\Delta z_k}. \tag{A.9}$$

The cloud vapor q and cloud temperature are then obtained by

$$q_{i,k-\frac{1}{2}} = \overline{q_k^*} + \frac{\gamma}{(1+\gamma)L}\left[h_{i,k-\frac{1}{2}} - \overline{h_k^*} + L_f q_{i,k}^I\right], \tag{A.10}$$

and

$$T_{i,k-\frac{1}{2}} = \bar{T}_k + \frac{1}{c_p(1+\gamma)}\left[h_{i,k-\frac{1}{2}} - \overline{h_k^*} + L_f q_{i,k}^I\right]. \tag{A.11}$$

The term $L_f q_{i,k}^I$ in (A.10) and (A.11) is omitted in the first place. The total liquid water before ice formation and precipitation is thus $q^t - q^I - q$. The cloud temperature is used to calculate the ice production, I, which is then added to q^I. (A.10) and (A.11) are recomputed with the presence of q^I. The liquid water after ice formation, $\ell = q^t - q^I - q - I$, is divided into two parts: the suspended liquid water $\ell_{i,k-1/2}$, and precipitation (per unit cloud-base mass flux from cloud-type i falling from layer k):

$$r_{i,k} = \eta_{i,k}\frac{c_0\Delta z}{1+c_0\Delta z}\ell_{i,k} = \eta_{i,k}C_{i,k}, \tag{A.12}$$

where $c_0 = 2\times 10^{-4}$ m^{-1} and C is the net condensation. The surface precipitation is

$$P_0 = \sum_k M_i r_{i,k}, \tag{A.13}$$

where M_i is the cloud-base mass flux of cloud-type i.

A.9 Determining the Cloud Top

In our approach, with the assigned values of λ, we can obtain the buoyancy of the clouds at all model levels, and interpolate to get the pressure level, $\hat{z}(\lambda)$, where the cumulus clouds lose buoyancy

$$B_k = h_k - \overline{h_k^*} + L_f q_k^l + \left[Lf(\overline{q_k^*} - \bar{q}_k - \frac{1}{\delta}(1 + q^l - \bar{q}^l)) \right] = 0, \tag{A.14}$$

where all variables are defined on even levels. We search for level k from the top down, such that $B_k < 0$ and $B_{k+1} > 0$ and the cloud top is determined using direct interpolation

$$\hat{z} = z_{k+1} + \kappa \Delta z_{k+1}, \tag{A.15}$$

where

$$\kappa = \frac{B_{k+1}}{B_{k+1} - B_k}. \tag{A.16}$$

$\hat{z}(\lambda)$ is then used in integrating the cloud work function (from Eq. B 92 of Lord, 1978)

$$A(\lambda) = \int_{z_B}^{\hat{z}(\lambda)} \frac{g}{c_p T} \eta(\lambda, z) \frac{\varepsilon\delta}{f} B(\lambda, z)\, dz, \tag{A.17}$$

where $z_{k+1} < \hat{z}(\lambda) < z_k$. There might be several level k's that satisfy t $B_k < 0$ and $B_{k+1} > 0$. In that case, we let the tallest k be the cloud top. These clouds are similar to the "E-type" clouds of Lord (1978).

The effects of the cumulus clouds, per unit cloud-base mass flux and per time step on the environment, in moist static energy and water vapor mixing ratio, are given by

$$\delta_i \bar{h}_k = -g\frac{\partial}{\partial p}\eta_{i,k}(h_{i,k} - \bar{h}_k) =$$

$$-\frac{g}{\Delta p_k}[\eta_{i,k-1}(h_{i,k} - \bar{h}_{k-1}) - \eta_{i,k}(h_{i,k+1} - \bar{h}_k)], \tag{A.18}$$

and

$$\delta_i \bar{q}_k = -g\frac{\partial}{\partial p}\eta_{i,k}(q_{i,k} - \bar{q}_k) =$$

$$-\frac{g}{\Delta p_k}[\eta_{i,k-1}(q_{i,k} - \bar{q}_{k-1}) - \eta_{i,k}(q_{i,k+1} - \bar{q}_k) + \eta_{i,k}C_k]. \tag{A.19}$$

Here we have assumed that all the detrained liquid water evaporates and ice sublimates immediately. We do not need to consider the detrainment layer separately, where it is usually evaporative cooling and moistening instead of subsidence warming and drying. (A.18) and (A.19) are applied in layers k=1, 2, ..., *KT+1*, where *KT* is the cloud-top layer. At the top of the cloud-top layer, $\eta_{i,KT-1} = 0$ and the two equations above reduce to

$$\delta_i \bar{h}_{KT} = \frac{g}{\Delta p_{KT}}\eta_{i,KT}(h_{i,KT+1} - \bar{h}_{KT}), \tag{A.20}$$

and

$$\delta_i \bar{q}_{KT} = \frac{g}{\Delta p_{KT}}\eta_{i,KT}(q_{i,KT+1} - \bar{q}_{KT} - C_{KT}). \tag{A.21}$$

The cumulus effects must be small when the cumulus clouds barely penetrate into layer *KT*, we therefore choose

$$\eta_{i,KT} = \kappa(1 + \lambda\Delta z_{KT+1})\eta_{KT+1}. \tag{A.22}$$

This relation conserves the moist static energy between the two layers *KT* and *KT+1* and water substance. This is equivalent to spreading the cumulus detrainment into the layer below *KT* when the cumulus clouds are barely into layer *KT* and, therefore, the cumulus effects in layer *KT* are weak.

Since we allow more than one λ-cloud to detrain in one layer, The total effects of cumulus clouds on the environment are

$$\delta\bar{h}_k = \sum_i^N \frac{1}{C} M_i (\delta_i \bar{h}_k) , \tag{A.23}$$

and

$$\delta\bar{q}_k = \sum_i^N \frac{1}{C} M_i (\delta_i \bar{q}_k) , \tag{A.24}$$

the constant C is related to $\Delta\lambda$ and the vertical resolution of the model. No matter how many λ-clouds exist in the same time (or how small $\Delta\lambda$ is), the cumulus effects can only be seen within the model vertical resolution. On the other hand, when we calculate the cloud work function, every λ-cloud is calculated independently with the same environmental sounding and a different number for λ.

Appendix B

Calculation of the Spectral Density Function

Given a time series *v(t)*, we first calculate its autocovariance function

$$R(\tau) = \frac{1}{T}\int_T v(t-\tau)\,v(t)\,dt, \tag{A.25}$$

where T is the record length. We then Fourier transform the autocovariance function and get

$$(S(f))^{1/2} = \int R(\tau)\,e^{-i2\pi f\tau}d\tau, \tag{A.26}$$

where $S(f)$ is called the *power spectral density.*

In discrete form for time series *v(n)*, we rewrite the autocovariance function as

$$R(m) = \frac{1}{N-m}\sum_{n=1}^{N-m} v_n v_{n+m}, \tag{A.27}$$

where N is the record length. Before we make the discrete Fourier transformation, we make *R(m)* an even function by using *R(-m) = R(m).*

$$(S(j))^{1/2} = \sum R(m)\,e^{-i2\pi j\Delta f}. \tag{A.28}$$